Universidad Nacional Autónoma de México

Programa de Posgrado en Astrofísica

Instituto de Astronomía

UN ESTUDIO EN MULTILONGITUDES DE ONDA DE UNA MUESTRA DE AGNs SELECCIONADAS MEDIANTE RAYOS X DUROS

T E S I S

Que para obtener el grado académico de

DOCTOR EN ASTROFÍSICA

Presenta

ANGEL CASTRO CASTRO

Director de Tesis

Dr. TAKAMITSU MIYAJI

Ensenada, B. C., Junio 2017

RESUMEN

UN ESTUDIO EN MULTI-LONGITUDES DE ONDA DE UNA MUESTRA DE AGNs SELECCIONADA MEDIANTE RAYOS X DUROS

ANGEL CASTRO CASTRO

Dirigida por el Dr. Takamitsu Miyaji

Junio 2017

En el presente trabajo se presenta un estudio sistemático en las bandas del cercano y mediano infrarrojo de las las propiedades de formación estelar en la zona circumnuclear de una muestra de AGNs cercanas seleccionadas mediante un criterio de rayos X duros.

En una primera etapa de este trabajo estudiamos los espectros de baja resolución en la banda 2.2–5 μm obtenidos mediante la cámara infrarroja (IRC; InfraRed Camera) a bordo del observatorio espacial infrarrojo Akari. Se consideró una muestra de 54 AGNs brillantes seleccionadas bajo un criterio de selección a partir de rayos X duros, que incluyó tanto objetos Seyfert 1s como Seyfert 2s. A esta muestra le denominamos la 'muestra temprana'. Dicha muestra fue seleccionada a partir del catálogo Swift/Burst Alert Telescope (BAT) 9–month survey (Tueller et al., 2008) en la banda 14–195 keV. Todos ellos poseen mediciones espectrales en rayos X (E $\geq$ 10 keV) disponibles en la literatura (e.g. Winter et al., 2009, y referencias ahí incluidas). Estos espectros en rayos X proporcionan mediciones de la densidad columnar de hidrógeno neutro (N_H) en dirección a las AGNs. Usamos la luminosidad de la línea de emisión en 3.3 μm ($L_{3.3\ \mu m}$) de PAH como indicador de la tasa de formación estelar (SFR) y la luminosidad de rayos X duros en la mencionada banda

($L_{14-195\ keV}$) como un indicador de la actividad del AGN. Buscamos posibles diferencias en la actividad de formación estelar entre las AGNs tipo 1 (no absorbida) y tipo 2 (absorbida).

Nuestro análisis de la muestra temprana con Akari/IRC incluye tanto detecciones como no-detecciones de la línea de emisión de PAH. Para este último caso se determinaron límites superiores, por lo que fue necesario emplear métodos de superviviencia para el análisis de datos que incluyen datos censurados (e.g. límites superiores). Usando los datos de la muestra temprana, se encontró fuerte correlación SFR y $L_{14-195keV}$, así como entre sSFR y (λ_{Edd}) para las AGNs tipo 1. No se encontró diferencia estadística en la SFR media, trazada por la línea de 3.3 μm, entre las AGNs tipo 1 y tipo 2 dentro de nuestra muestra. Se determinó también la tasa de formación estelar específica (sSFR) y la $L_{14-195keV}$ normalizada por la masa del agujero negro, siendo esta relación proporcional a la razón de Eddington (λ_{Edd}).

Los resultados de la regresión lineal para la relación $\log(L_{14-195keV})$–$\log(L_{3.3\ \mu m})$ muestran una correlación positiva, siendo la pendiente para las tipo 1 (AGNs no-absorbidos) más pronunciada que para las tipo 2 (AGNs-absorbidos) en un nivel 3σ. Nuestro análisis también muestra que la formación de estrellas circumnuclear está más estimulada en las tipo 2 que en las tipo 1 por la baja luminosidad de rayos X para AGNs con baja razón de Eddington, mientras que no hay ninguna dependencia significativa entre la actividad de formación estelar circumnuclear y el tipo de la AGN para las fuentes con altas luminosidades en rayos X/razones de Eddignton.

Nuestros resultados sugieren que la diferencia entre las AGN tipo 1 y 2 de baja luminosidad podría reflejar una secuencia evolutiva, donde más material está disponible alrededor de las AGNs tipo 2 siendo suministrando hacia la maquinaria central. En el escenario de altas luminosidades, la diferencia entre tipos 1 y 2 podría deberse principalmente al efecto de orientación.

En una segunda etapa del trabajo, como extensión de nuestra investigación fueron incluidas fuentes en el mid-IR completando una muestra final de 130 fuentes observadas mediante el espectrómetro infrarrojo (IRS; InfraRed Spectrometer) a bordo del observatorio espacial Spitzer con un criterio de selección z $<$

0.1 en el rango de luminosidades $42 \leq \mathrm{L}_{14-195\mathrm{keV}} \leq 45$. A esta muestra le denominamos la 'muestra extendida'. Debido a la diferencia temporal entre la primera y la segunda etapa, ahora se incluyen todos los objetos Seyfert del catálogo Swift/BAT 70-month survey (Baumgartner et al., 2013) que además cuentan con datos públicos de Spitzer/IRS en la base de datos infrarrojos de la NASA. Aproximadamente el 53% de los objetos con datos Spitzer/IRS cuentan también con espectros observados por Akari/IRC, lo cual permitirá realizar estudios comparativos entre las líneas de emisión de PAHs en el mediano y cercano infrarrojo. Para el presente trabajo se midieron también las líneas de emisión de PAHs en 6.2 y 11.3 μm y se estudiaron empleando los mismos procedimientos y técnicas para la determinación de las propiedades de SFR circumnuclear basados en la líneas de 11.3 μm en particular.

En este trabajo se exploran las dependencias entre la emisión de rayos X duros y las propiedades de SFR circumnuclear basados en las líneas de emisión de PAH en 3.3 y 11.3 μm. Se presenta también un análisis comparativo entre estas propiedades de acuerdo al tipo espectral (i.e. Seyfert 1 o Seyfert 2).

AGRADECIMIENTOS

El presente trabajo fue supervisado por el Dr. Takamitsu Miyaji, quien me apoyó desde el incio del posgrado, primero como maestro y luego como supervisor. Takamitsu es un amigo y colaborar sin el cual este trabajo no hubiese sido posible. Agradezco su compromiso y paciencia a lo largo de todo este tiempo. Para la realización de este trabajo se contó con el apoyo financiero de las becas CONACyT 179662 y 252531, DGAPA - Universidad Nacional Autónoma de México (UNAM), las becas PAPIIT IN104216 y IN104113, así como del apoyo parcial de las becas Grants-in-Aid for Scientific Research 23540273 y 26400228 del Ministerio de Educación, Cultura, Deporte, Ciencia y Tecnolgía (MEXT) de Japón.

Este trabajo fue presentado, en diferentes estapas de completitud, en diversos congresos y simposios, con el apoyo económico del Comité de Posgrado del IA-UNAM y los poyectos PAPIIT IN104113 y IN104216. Entre ellos: XIII Latin American Regional IAU Meeting, IAU S304: Multiwavelength AGN Surveys and Studies, The Universe in the light of AKARI and Synergy with future Large Space Telescopes Symposium, XXV Reunión Nacional de Astronomía, y el LVII Congreso Nacional de la Sociedad Mexicana de Física, y otros. Un versión reciente de este trabajo fue presentada la XXIX IAU General Assembly con el apoyo económico del Dr. L. Gutiérrez a través de la beca CONACyT No. 167236.

Quiero extender este agradecimiento a muchas otras personas que han contribuido con su esfuerzo, amistad o apoyo. En lo familiar, agradezco a mis padres Saida y Herniloberto, así como a mi hermana Claudia Castro por su completo e incondicional apoyo. A Liliana Altamirano, mi amiga, mi persona, mi amor y mi compañera de vida y ahora madre de Leonardo, nuestra fuerza. Agradezco a las familias Esparza-Núñez y Pánfilo Osuna por su apoyo a través de muchos años de amistad. A los maestros que con su trabajo y ejemplo contribuyeron a mi desarrollo personal y profesional. Agradezco particularmente al Dr. Raul

Michel, quien me permitió inicialmente acercarme al mundo de la Astronomía, por el entrenamiento en el manejo de telescopios y diversas técnicas observacionales. Mi gratitud al personal administrativo y técnico del Observatorio Astronómico Nacional.

Agradezco a los Drs. Luis Salas, David Hiriart, Elena Jiménez-Bailón, Omar López-Cruz, Héctor Aceves y Leonel Gutiérrez, quien formaron parte de mi comité tutoral y me dieron su consejo durante el desarrollo de esta investigación. Agradezco también a los Drs. Irene Cruz-González, Anna Lia Longinotti, Omaira González-Martín y Jacopo Fritz por su trabajo como miembros de comité sinodal, cuyas correcciones, comentarios y sugerencias contribuyeron al mejoramiento del presente trabajo, y finalmente, a la Biol. Bertha Vázquez por su enorme apoyo administrativo recibido a lo largo de todo el posgrado.

La presente investigación está basada en observaciones realizadas con el observatorio infrarrojo espacial Akari, un proyecto de la Agencia Espacial Japonesa (JAXA) con la participación de la Agencial Espacial Europea (ESA), y de telescopio espacial Spitzer, el cual es operado por el Jet Propulsion Laboratory en el California Institute of Technology. Los sitios web de los catalogos del Swift/BAT 70-month y 9-month son operados por NASA Goddard Space Flight Center.

Contents

List of Tables

List of Figures

CHAPTER 1

INTRODUCTION

1.1 Overview

Supermassive black holes (SMBHs) in the nuclei of galaxies are widely accepted to grow over the cosmic time mainly by accreting matter. However, the fueling mechanism, where gas is accreted from a kilo-parsec scale to a sub-parsec scale towards the black hole (BH; e.g. Alexander & Hickox, 2012) as well as the triggering mechanisms remain as fundamental questions. A galaxy that exhibits bright emission in the nuclear region due to the release of gravitational energy from the inner infalling gas of the host galaxy onto the SMBH is named an Active Galactic Necleus (AGN).

Recent studies report an excess of young to intermediate age stars in the inner few handred parsecs when compared with non-active galaxies (e.g. Cid Fernandes et al., 2001; Davies et al., 2007; Esquej et al., 2014) supporting the idea of a AGN-Starburst connection (Perry & Dyson, 1985; Norman & Scoville, 1988). As summarized in Alexander & Hickox (2012), it is actually concensed that gas inflow from kpc scales down to the central 100 pc region occurs in gas-rich galaxies, from a variety of external (major and minor mergers, fly-bys) or internal (secular, circumnuclear stellar winds) events, which inject a large amount of angular momentum to the infalling gas. But because accretion produces radiation, and radiation makes pressure, it is also suggested that once AGNs are ignited, feedback from AGNs may clear surroundings from cold gas and quench star formation and further accretion (e.g Bundy et al., 2008; Lagos et al., 2008).

According to the unified scheme of AGNs (e.g. Antonucci , 1993; Urry & Padovani, 1995), the different

observational properties of AGNs (e.g. optical emission-line widths and X-ray spectral slopes) are due solely to the viewing-angle-dependent obscuration of the nucleus: those sources viewed face-on are unobscured (allowing a direct line-of-sight to their nuclei) and entitled as "type 1" AGNs, while those viewed edge-on are "type 2" AGNs with most of their central engine and broad line regions being buried by the obscuring dust (Li, 2006).

However, many studies found in the literature show that the fraction of absorbed (type 2) AGNs decrease with luminosity (Lawrence & Elvis, 1982; Ueda et al., 2003; La Franca et al., 2005; Shinozaki et al., 2006; Hasinger, 2008; Ueda et al., 2014), nevertheless it might be due a selection effect based on X-rays or optical emission lines (Lawrence & Elvis, 2010). The same trend has been observed in optical/IR (e.g. Maiolino & Risaliti, 2007) and in the X-ray/IR (e.g. Ichikawa et al., 2012b). Simpson (2005) also found that the fraction of type 1 AGNs increases with luminosity and shows that the faint-end slope of the AGN luminosity function steepens considerabily when a correction for the 'missing' type 2 is made.

Also, clustering studies indicate some systematic difference of large-scale environments between type-1 and type-2 AGNs (Cappelluti et al., 2010; Allevato et al., 2011) (but see also Hickox et al. (2010) for results for absorbed and un-absorbed QSOs). These observations suggest that type 1 (unabsorbed) and type 2 (absorbed) AGNs have some systematic differences in their intrinsic properties, beyond the viewing angle effect, such as opening angle/distribution of the absorbing material (e.g. Ramos-Almeida et al., 2011; Elitzur et al., 2012), and these two classes may be in different stages of AGN evolution, with a significant overlap. If a circum-nuclear starburst plays a major role in feeding the central SMBH at the early stage of the AGN activity, where the absorbing torus may have a thicker geometry with a larger covering factor, it is more likely to be observed as a type 2 AGN.

Measuring the amount of the X-ray extinction provides information on the total column density of the interstellar matter along the line-of-sight (Güver & Özel, 2009). The amount of the X-ray extinction is frequently expressed in terms of the equivalent hydrogen column density ($\mathrm{N_H}$). Recent observational evidence based on the shape of the X-ray backgound (XRB) suggest that although the fraction of obscured AGN is found to decrease with luminosity a non-negligible population of highly obscured Compton-thick (CTK; defined as those heavily obscured AGNs with $\mathrm{N_H} > 10^{24}\ \mathrm{cm^{-2}}$) AGNs is still required (Gilli et

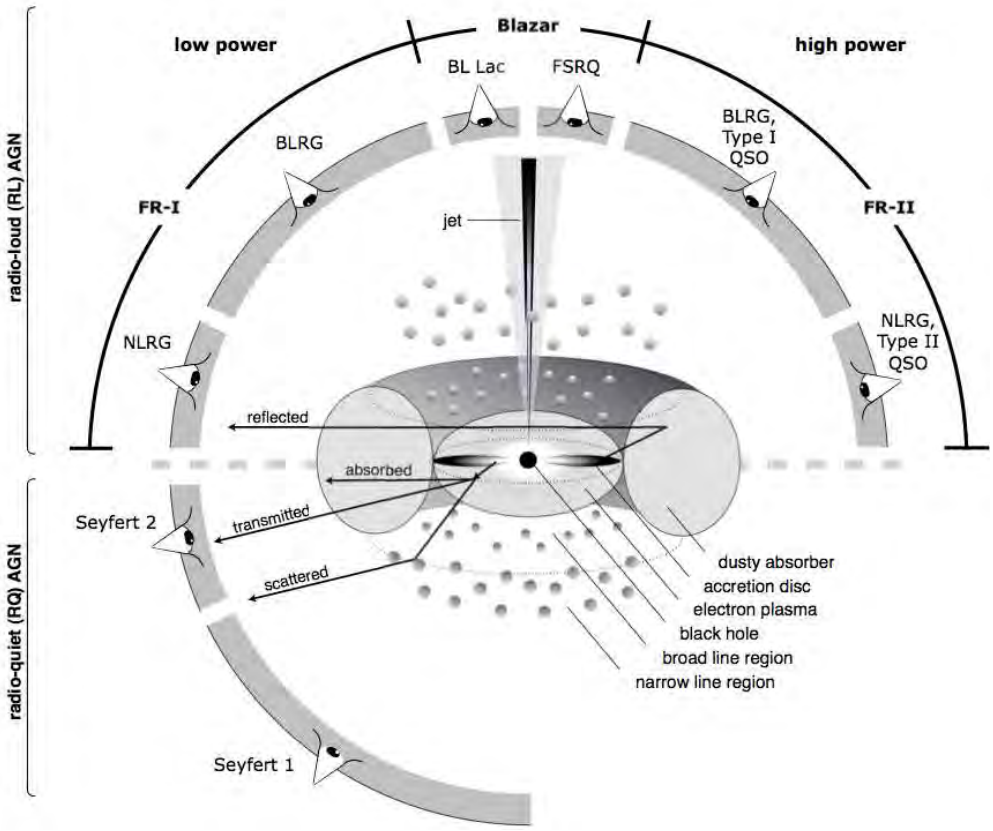

Figure 1.1: Schematic representation of the AGN phenomena in the context of the unified model scheme. Taken from Beckmann & Shrader (2013).

al., 2007), contrasting with the results of Esposito et al. (2016). Esposito et al. (2016) argues that a lager population of CTK AGNs is not required, since the reflection component of mildly oscured AGNs could reproduce the XRB without a large population of CTK AGNs.

Ueda et al. (2014) found that the fraction of CTK AGNs to absorbed Compton-thin AGNs should be 0.5–1.6 in order to reproduce the hard XRB intensity in the 20–50 keV band within current uncertainties. This is also well consistent with the results of hard X-ray surveys above 10 keV currently available. The correct determination of the ratio of unobscured to obscured AGNs as a function of luminosity and redshift will provide a constrain to the growth history of SMBHs.

Soft X-ray (2–10 keV) and mid-IR observations provide powerful, complementary methods for identifying and studying AGNs over a wide range of intrinsic obscuration (Eckart et al., 2010). However, very

hard X-ray $E > 10$ keV) surveys such as available with Swift Burst Alert Telescope (BAT; Tueller et al., 2008, 2010; Ajello et al., 2012; Baumgartner et al., 2013) or INTEGRAL (Krivonos al., 2010) allows us to select AGNs with a wider range of absorbing column densities, since photoelectric absorption is negligibly small. This property makes them easily identifiable in the various surveys and easy to study both visually and spectroscopically. However, hard X-ray surveys (e.g. Swift/BAT) of AGNs provide observations along a wide range of intrinsic absorption and are less biased and more complete than optical (e.g. Richards et al., 2006) and soft X-ray ($E \leq 2.4$ keV; Hasinger et al., 1998) surveys.

There are many previous studies in the literature showing the presence of star formation activity in AGNs (Cid Fernandes et al., 2001; Davies et al., 2007; Oi et al., 2010; Alonso-Herrero et al., 2014; Castro et al., 2014; Esquej et al., 2014). Classical indicators of on-going or recent star formation (e.g. Hα, Paα, UV emission, [NeII] 12.8 μm) are difficult to use in the nuclear regions of AGNs, as they can be easily contaminated by bright AGN emission (Alonso-Herrero et al., 2014). The polycyclic aromatic hydrocarbon (PAH) features have been used to disentangle between AGN and starbursts (SB) in Ultra-Luminous InfraRed Galaxies (ULRIGs;e.g. Sanders et al., 1988; Lutz, 1998), since observationally these features have been found to be weak or absent in classical AGNs but generally strong in starbursts (Moorwood, 1986; Genzel et al., 1998; Imanishi & Dudley, 2000). The PAH emission act as an indicator for the presence of pumping far-ultraviolet (FUV) photons and reveals the presence of massive stars (Genzel et al., 1998; Tielens, 2008). The source of the UV radiation is generally considered to be from the massive stars in the star-formation region rather than AGNs, because in AGNs, X-ray photons destroy the PAH molecules (Voit, 1992). From a study of the IR properties of sample of Galactic massive star-forming regions, normal starburst galaxies, and well as AGNs and ULIRG, Peeters, Spoon & Tielens (2004) concluded that PAH the emission may be better suited as a tracer of B stars instead of massive stars (O-type). This phenomenon could imply that the emission of PAHs is associated with star formation through a time-scale of tens of millions of years instead of instantaneous star formation.

The mid- and near-infrared spectrum of star-forming galaxies is dominated by strong emission features generally atributed to PAHs. In galaxies with intense star formation, up to 20% of the total infrared luminosity is emitted in the PAH band alone (Smith et al., 2007). The PAH emission features observed

in the infrared spectra (e.g. 3.3, 6.2, 7.7, 8.6, and 11.3 μm), may be used as indicators of star-formation activity with little contamination from AGNs, providing a tool for investigating star formation activities in AGNs. However, Diamond-Stanic & Reike (2010) argued that in local Seyfert galaxies the 6.2, 7.7, and 8.6 μm features are supressed on kpc scales with respect to the 11.3 μm PAH features (see also Smith et al., 2007).

Ground-based IR astronomy is noticeable affected by the atmosphere. Telluric absorption in the rotational and ro-vibration bands of atmospheric gases blind the transmission in the $30 \leq \lambda[\mu\mathrm{m}] \leq 300$ band, and allowing observations only particular windows such as the M (4.5–5.2 μm), the N (8–13 μm), and Q (18–23 μm) bands (Tielens, 2008). Also, the quality of observations may be affected by the thermal emission of the sky, and the telescope itself. In order to avoid this ground-based observational limitations satellital observations can be carried out. The IRC instrument (Onaka et al., 2007) onboard the Akari satellite (see Figure 3.1) provides spectroscopical coverage in the near-infrared band between 2.5 and 5 μm. On the other hand, the Spitzer Space Telescope (see Figure 3.8) allows high sensitivity observations in the 3.6–160 μm band. The primary imaging camera on Spitzer is the Infrared Array Camera (IRAC; Fazio et al., 2004), gathering simultaneous imaging at 3.6, 4.5, 5.8 and 8 μm, while the Infrared Spectrograph (IRS; Houck et al. (2004)) provides spectroscopical data in the 5–38 μm band. Several methods have been developed to select AGNs based on Spitzer/IRAC colors based of the typical spectral energy distribution (SED) of AGNs compared to that of normal galaxies (Stern et al., 2005; Alonso-Herrero et al., 2006). The Akari/IRC and Spitzer/IRS instruments let us to reach the main PAH emission lines in the IR band.

There have been a number of studies that have investigated the PAH emission in a sample of known AGNs and investigated the differences in PAH emission properties among various types of AGNs. Clavel et al. (2000) and Freudling et al. (2003) showed that weak PAH and hot dust are more associated with type 1 AGNs while cooler dust and strong PAHs with type 2 AGNs. Haas et al. (2005) argued that nuclear starburst should be weaker in low-luminosity AGNs. Studying the stellar population of the central $\sim$200 pc of a sample of 79 nearby galaxies, most of them Seyfert 2s, Cid Fernandes et al. (2004) found no correlation between the star formation in the nucleus, neither for the host morphology nor for the presence of companions. The star formation history deduced from their study varied significantly among Seyfert 2s.

Based on a study of a sample of 32 Seyfert galaxies (including both type 1 and type 2) Imanishi & Maloney (2003) and Imanishi & Wada (2004) found correlation between SB and nuclear activity. However, no significant differences have been found between type 1 sources and type 2 sources. Other subsequent studies have reached the same conclusion (e.g. Watabe et al., 2008; Oi et al., 2010; Weaver et al., 2010; Diamond-Stanic & Reike, 2012) in regarding the absence of dichotomy of the SFR properties between type 1 and type 2 sources. In particular, Weaver et al. (2010) conducted a study of the mid-infrared emission-line properties from high-resolution Spitzer spectra of the Swift/BAT AGNs of a sample of nearby galaxies ($z < 0.05$). They found that the distribution for the [OIV] 25.89 μm, [NeII] 12.81 μm, [NeIII] 15.56 μm, [NeV] 14.32/24.32 μm emission lines, and hard X-ray continuum show no differences between type 1 and type 2 AGN populations. They also found that the BAT AGNs fall into a clearly distinctive region based on the [NeIII]/[NeII] and [OIV]/[NeIII] ratios. In a similar analysis, Diamond-Stanic & Reike (2012) measured the AGN luminosity of a sample of Seyfert galaxies using the [OIV] 25.89 μm emission line and the star-forming luminosity based on the 11.3 μm PAH feature. They found strong correlation in the relationship between nuclear SFR (measured on r $\sim$ 1 kpc scales) and the BH accretion rate but only weakly correlated with extended (r $>$ 1 kpc) star formation in the host galaxy. They have not found statistically significant differences between type 1 and type 2 Seyfert objects.

1.2 AGN obscuration and the Unified Model

Seyfert galaxies are lower-luminosity AGNs, with blue absolute magnitude brightness defined by $\mathrm{M_B} > -21.51 + 5\ \log(h_0)$ for the AGN generally accepted criterion. Khachikian & Weedman (1974) were the first to realize that they can be separated into two classifications according to the presence or absence of broad optical/UV emission lines, where sources with optical emission lines, such as H_α and H_β, with more than $1000\ \mathrm{km\ s^{-1}}$ FWHM are considered to be type-1 Seyferts. These broad optical lines are not observed in Seyfert 2 galaxies. Besides these emission lines, most AGNs show a feature-less continuum spectrum in the optical band, produced by an unresolved source within the nucleus. In Seyferts type-1 this component is usually strong while typically weak in type-2s. The notation Seyfert 1.5, 1.8 and 1.9 was introduced by

Osterbrock (1977) based on the appearece of the optical spectrum, where numerical values correspond to weaker broad-line to narrow-line ratios.

However, after broad lines were discovered by Antonucci & Miller (1985) in the polarized sprectrum of NGC 1068, subsequent studies revealed that broad-line region (BLR) clouds can exist in both Seyfert 1 and Seyfert 2 AGNs. Based on this phenomenon, the unified AGN model (e.g. Antonucci , 1993; Urry & Padovani, 1995) proposes that difference between type 1 and type 2 AGNs are solely the viewing angle effect, making Seyfert 1 and Seyfert 2 galaxies identical (Awaki et al., 2000; Oi et al., 2010). In this scenario molecular gas and dust with a torus-like shape surrounds the central SMBH (as shown in Figure 1.1). Due to its composition this torus can obscure the AGN for a Seyfert 2 galaxy, and absorb the energy coming from the central object and re-radiate it in the infrared spectrum of both Seyfert 1 and Seyfert 2 AGNs.

The existence of a toroidal axisymmetric inner structure was infered by the presence of polarized emission lines in Seyfert 2 AGNs. If the absorber was a simple cloud along the line of sight, then reflection should come from all directions, and therefore the sum of all the measurements from every angle should result in a total of zero polarization. But this is not the case, the presence of a torus is a simple configuration that prevents scattering in every directions. In order to obscure the BLR it is requiered that the size of the torus be in the parsec scale, but at the same time small enough not to obscure the NLR, which is distributed on the 10–100 pc scale (Bianchi, Maiolino & Risaliti, 2012).

Measuments in the X-ray bands obtained with ASCA, INTEGRAL, Chandra, XMM-Newton, Susaku, Beppo-SAX and other satellites provide strong evidence in favor of the unified scheme. Most type-2 Seyferts are detected in the hard X-rays ($E > 2$ keV), but remain elusive to soft X-ray ($E < 2$ keV) surveys. The hard X-ray spectra of Seyfert 2s can be modeled by a simple power-law, just as a type-1 AGN, but affected by a photoelectric absorption cutoff. In some cases (e.g. Bassani et al., 1999), the X-ray spectra of Seyfert 2s do not show a well defined cutoff but prominent Fe Kα line at 6.4 keV with FWHM > 500 eV is found.

In type 2 AGN a bi-conical morphology of the NLR is revealed due to the photoionization of a nuclear UV/X-ray source hidden by a toroidal structure responsible of the oscuration in our line-of-sight. The observational infered relative fraction between type 1 and type 2 AGNs, in the local universe, is in good

agreement with the estimated opening angle of those cones (Maiolino & Rieke, 1995). In general, the orientation of the ionization cone and the radio jet are aligned in the same direction, but there are exceptions, revealing a small misalignment (at parsec or sub-parsec scales) of the central engine and the dusty torus (Wilson & Tsvetanov, 1994).

The idea itself of a uniform dust and gas distribution has been almost completely abandoned and replaced by models considering a clumpy structure (see Figure 1.3) of the absorbing medium (Elitzur & Shlosman, 2006; Nenkova et al., 2008; Hönig & Kishimoto , 2010; Nikutta et al., 2009). These models are in a more general agreement with recent X-ray, IR and othe wavelength observations.

1.2.1 Absorption at difference scales

Even the unified model remains accepted in its general picture (i.e. the pesence of non-spherically symetric absorbers at the origin of the type 1/type 2 dichotomy) it is now not enough to explain the complex absorption structures recently observed, mostly in the X-ray and IR domain. Those new observations reveal the presence of multiple absorbers around the central engine over different physical scales.

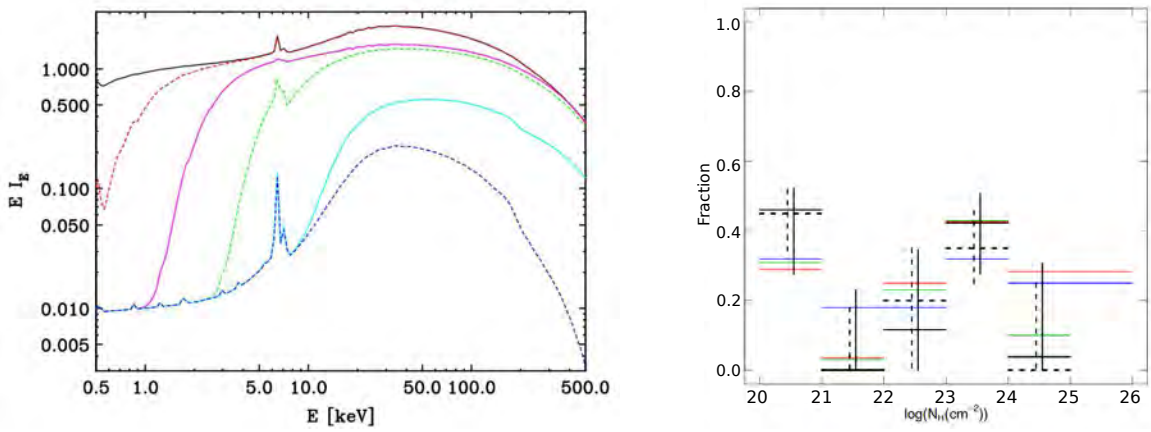

Figure 1.2: (*Left*) X-ray obscuration model of different neutral hydrogen column density AGNs from $\log(\mathrm{N_H}) = 20$ (black line) to $\log(\mathrm{N_H}) = 24$ (blue lines) in steps of $\Delta\log(\mathrm{N_H}) = 0.5$. Image taken from Ueda et al. (2014). (*Right*) Best fit $\mathrm{N_H}$ distribution using four different samples from literature. For details see Esposito et al. (2016).

Gas absorption

X-ray absorption variability measurments show that neutral hydrogen column density (N_H) variations are a common behaviour in local AGNs (see Figure 1.2). This variability implies that the circumnuclear absorber, or a component of it, must be clumpy material located at a sub-parsec scale from the central engine. A famous case is that of NGC 1365, where XMM-Newton, Chandra and Susaku X-ray observations revealed strong variations, from Compton-thin ($N_H \sim 10^{23}$ cm^{-2}) to CTK reflection-dominated ($N_H > 10^{24}$ cm^{-2}) on time scales from about 10 hours to a couple of days. These absorption events are related to clouds with velocities > 1000 km s^{-1} located at distances of the order of 10^4 gravitational radii from the BH. Physical sizes of these clouds are in agreement with the sizes of typical BLR clouds, suggesting that the X-ray absorber and the material producing the UV/optical broad emission lines are the same (Bianchi, Maiolino & Risaliti, 2012). In Figure 1.2(*right*) Esposito et al. (2016) show the results of the N_H distribution for several literature and own derived fraction.

Based on the observation of NGC 1365, Maiolino et al. (2010) argues that the presence of comet-like objects responsible for the absorption variations derived from X-ray detailed spectra. According to their model this cometary structure consist of a high density head, and an elongated tail gradually lowering density. It is estimated that the cloud head loses a siginificant mass fraction through time, implying the gradual evaporation of the cloud within a period o several months. In order to keep the long-term dynamical equilibrium it implies that the BLR must be continuously re-populated with gas clouds (Bianchi, Maiolino & Risaliti, 2012). More observations are still required to probe this model scenario.

1.2.2 Dust absorption

The ISM dust properties are obtained from the study of the emission and absorption spectral lines. From the mid-IR and near-IR bands we can measure in emission: the 3.3, 6.2, 7.7, 8.6, and 11.3 μm PAHs, and in absorption: the aliphatic hydrocarbon dust at 3.4 μm (often weak and dificult to identify and quantify), and the 9.7 and 17 μm amorphous silicate dust features. Also, there can be identified ice absorption features at 3.1 and 6.0 μm (H_2O), 4.67 μm(CO), 4.27 and 15.2 μm (CO_2), 3.54 and 9.75 μm (CH_3OH), 2.97 μm

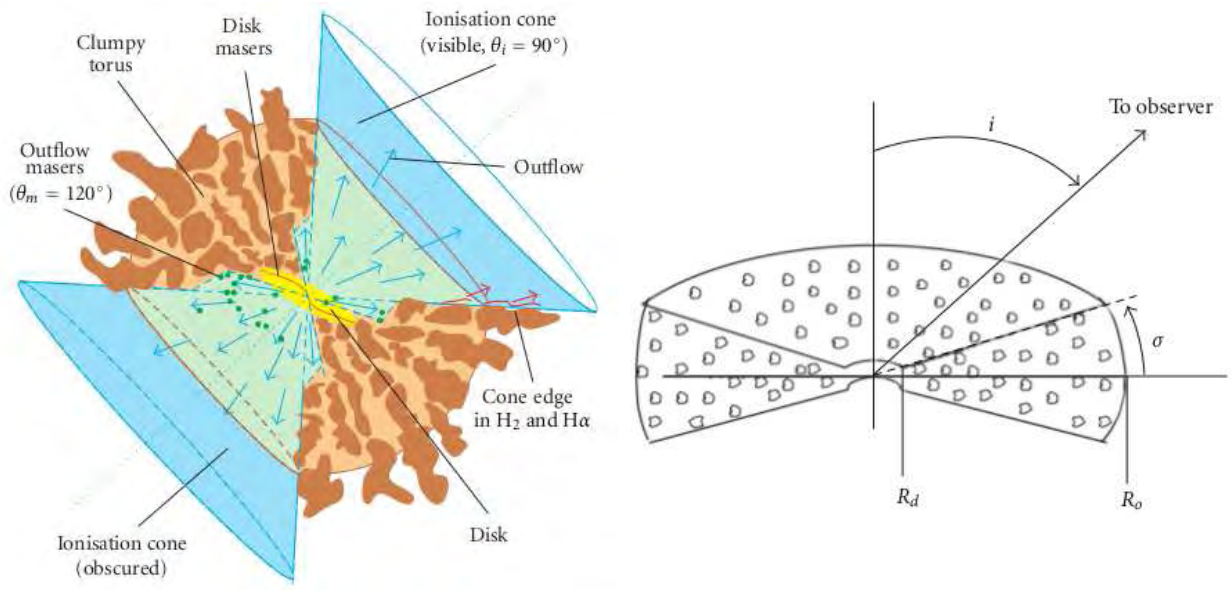

Figure 1.3: Dusty torus as derived from IR observations (*left*). Taken from Tristram et al. (2007). Dusty torus as a clumpy structure of the absorbing medium (*right*) taken from Nenkova et al. (2008).

(NH_3), 4.62 μm (XCN^-), 5.81 μm (H_2CO), and 7.68 μm (CH_4).

The strongest IR absorption features in the Galactic ISM are the 9.7 μm and 18 μm bands, which are almost certainly due to silicate minerals. The observed interstellar silicate bands are broad and relatively featureless, indicating that interstellar silicates are largely amorphous rather than crystalline (Li&Draine, 2001). Some sources may indicate differences in the dust composition, grain size distribution, or radiative transfer effects (e.g. Sturm et al., 2005).

1.2.3 AGN heated dust

Mid-IR spectrum can be explained by models of thermal re-radiation from dust. According to recent studies of dusty torus models, the observed circumnuclear mid-IR emission can be well reproduced assuming that the torus have a clumpy structure (e.g. Nenkova et al., 2008; Ramos-Almeida et al., 2011; Alonso-Herrero et al., 2011). Wu et al. (2009) have suggested a weak correlation between gas column density and silicate absorption strength based on mid-IR observations.

Recent mid-IR studies in the nuclei of Syefert 1 sources have shown the presence of hot dust, close to the

sublimation temperature (e.g. Alonso-Herrero et al., 2001, 2014). In this objects the sublimation radius is on sub-parsec scales and on parsec scales at quasar luminosities. Near-IR determinations of the location of this hot dust emitter are supported by long-term reverbeation studies, also constraining the $L_{44}^{1/2}$ dependence of the sublimation radius, where L_{44} is the AGN luminosity in units of 10^{44} $ergs^{-1}$. In this way, the sublimation temperature establish an upper-limit to the dust temperature ($1000 < T_d < 1500$ K). In some cases, in order to adequately reproduce the near-infrared continuum, a Planck distribution of T $\geq$ 1000 K is needed to account for the strong excess of emission over a featureless continuum of power-law form (e.g. Mrk 1239, Rodriguez-Ardila & Mazzalay (2004); NGC 7469, Marco & Alloin (2000)).

Some other authors have mentioned that there are difficulties in fitting their near-infrared SEDs (Ichikawa et al., 2014, and references there in). This difficulty is due to the complicated degeneracies, including the possible existence of an extra hot-dust ($\sim$ 1500 K) component originating from the vicinity of the AGN (Kishimoto al., 2011), and/or contamination/extinction from the host galaxies.

1.3 The Stellar and Starburst Components

The stellar photospheric emission from the host galaxies contributes to the total observed spectra in the near- and mid-infrared band. Particularly in non-resolved objects it is important to be able to adequately remove stellar contamination in the infrared spectra, especially at the blue end of the spectrum for the 2.5–5 μm and 5–14 μm bands studied here. Ichikawa et al. (2014) have proposed first to determine the stellar temperature by fitting the 2MASS J, H, and K_s photometric data with a blackbody model over the Akari/IRC 2.5–5 μm spectra. Once this adjustment has been made, the dust and starburst contributions can be calculated.

The term 'starburst' (SB) refers to intense star formation in galaxies, as first noticed by Weedman et al. (1981) while studying the galaxy NGC 7714. SBs heat a lot a dust, usually this dust is heated up to temperatures lower than those of the AGN-heated (see Section 1.2.3). The stuburst activity is related to (a) the gas available for the creation of new stars, (b) the intrinsical SFR of the galaxy, and (c) the timescale of the star-forming activity related to the dynamical timescale of the galaxy itsel (e.g. galactic rotation period). The mid- and near-infrared spectra of these objects is extremelly populated by PAH emission

features dominating in the IR-band. The SED of starburst systems can be constructed from the linear combination of numerous individual galactic HII regions (Kennicutt, 1998). Under this assumption, the total IR luminosity can be used a tracer of recent star formation in galaxies.

Total infrared (8–1000 μm) luminosity (L_{IR}), in units of solar luminosity, can be calculated from (Sanders & Mirabel, 1996) using the 12, 25, 60, and 100 μm Infrared Astronomical Satellite (IRAS) flux density in the unit of Jansky (Jy)

$$L_{IR}[M_{\odot}] = 2.1{\times}10^{39}{\times}D(Mpc)^{2}{\times}(13.48f_{12} + 5.16f_{25} + 2.58f_{60} + f_{100}) \tag{1.1}$$

Additionally, some systems show an enhancement of their IR emission. Warm IRAS colors ($f_{25}/f_{60} \geq 0.3$) are useful for diagnosing IR galaxies (De Grijp et al., 1985).

It is assumed that the observed IR and X-ray spectra are the sum of the starburst and AGN contributions along these bands. For objects that show an intense emission of PAH its bolometric lominosity is dominated by star formation. According to Kennicutt (1998) and Brandl et al. (2006), L_{IR} of starbursts is a good measure of the SFR given by

$$SFR\ [M_{\odot}\ yr^{-1}] = 4.5 \times 10^{-44}\ L_{IR}\ [erg\ s^{-1}] \tag{1.2}$$

The SFR can also be estimated by combining the L_{FIR}–$L_{3.3\ \mu m}$ relation Mouri et al. (1990) and the L_{FIR}–SFR relation Kennicutt (1998), respectively, into the realtion

$$\log(SFR\ [M_{\odot}yr^{-1}]) = \log(L_{3.3\ \mu m}\ [erg\ s^{-1}]) - 40.34 \tag{1.3}$$

Using the 11.3 μm PAH feature luminosities the SFR can be derived by applying the Diamond-Stanic & Reike (2012) relation

$$\mathrm{SFR}\ [\mathrm{M}_\odot\ \mathrm{yr}^{-1}] = 9.6 \times 10^{-9}\ (\mathrm{L}_{11.3\ \mu\mathrm{m}}\ [\mathrm{L}_\odot]) \tag{1.4}$$

As shown in Figure 1.4, the integrated near- and mid-infrared spectra can be a mixture of the contribution of recent star-forming events and radiation from the galactic central engine. Thus, $\mathrm{L_{IR}}$ can have significant contribution from dust powered by AGNs and we cannot simply use Equation 1.2 for estimating SFR. On the other hand, PAH emission features are powered by AGN emission very little and Equations 1.3 and 1.4 are much better SFR indicator in galaxies that harbours AGNs.

Figure 1.4: (Left) Geometry of energy sources and dust in a normal SB galaxy. The open star symbols indicate "stars" in a SB. PAH is observed plus a continuum, in spite of the dust extinction because PAH and continuum fluxes are similarly affected in this geometry. (Center) Geometry of the energy source and dust in a buried AGN. The energy source (compact mass-accreting SMBH) is centrally concentrated than the surrounding dust. (Right) A buried AGN and a SB composite. The observed spectrum is a superposition of PAH+continuum emission from the SB and PAH-free continuum from the buried AGN. For all cases, firstly, local galactic dust extinction shall be considered over the complete wavelength detection range before adjusting any model.

Our sample has been chosen under an X-ray selection criteria because, at $\log(\mathrm{L}_{14-195\mathrm{keV}}) > 42$ [erg s^{-1}] X-ray emission is almost solely powered by AGN activity, thus, little contamination from star-forming is expected in our sample.

1.4 PAH interstellar features

The term Polycyclic Aromatic Hydrocarbons (PAHs) refers to the fused, multi-cyclic hydro-carbons without substituents or any heteratoms within the ring structure (Fetzer , 2016). It is belived that PAHs (see Figure 1.5) are ubiquous in the Universe, observable in near objects and even in high redshift cosmological sources. Nevertheless, PAH features are still not attributed to specific molecular species. It has not been possible to

reproduce such low-density and high excitation level PAHs under laboratory conditions, making defficult to create a proper catalog which could be used as a reference for astronomical observations.

PAH absorb maily UV and visible photons, from rates of about once per week in the diffuse ISM (using as a reference the ovalene molecule, $C_{32}H_{14}$) to about once per hour in bright photodissociation region (PDR) with a photon density four orders of magnitude larger (Mulas et al., 2013). Once the molecule has absorbed a photon it moves from ground state to an excited electronic state. Now, the molecule can relax in several ways: by emitting and electron, trough several radiationless transitions, or by radiative transitions (releasing energy through fluorescence or phosphoresence). If PAH molecules are under the influence of a strong radiation field they also can also fragment. In the presence of a weaker radiation field they can just relax radiatively via delayed fluorescence and/or vibrational transitions (infrared cooling). In most of the cases, vibrational transitions are located at very near wavelengths creating a pile up effect and making the classical broad observable aromatic infrared bands (AIBs). UV-visible photon absorption events are widely more frequent than collisions, making collision events negligible.

Laboratory PAH photofragmentation experiments have shown that PAHs can lose sidegroups (hydrogens, methyl, di-methyls, etc.) if enough energy is available to broke that bound. Once the PAHs have been de-hydrogenated the fragmentation process continues breaking the carbon skeleton into smaller stable pieces (isomers), and so on, before being completely dissociated. Photofragmentation process happens along thermal cooling making AIBs even more complex. Photo-absorption spectrum of PAHs can now only be estimated by standard theoretical models. The quantity of species considered into these models is constantly being increased (including nitrogenated PAHs, superhydrogenated or dehydrogenated PAHs, aliphatic PAHs, deuterated PAHs, etc.).

Because of their prominency most astronomical studies on PAHs are focused on near-IR and mid-IR vibrational bands (e.g. Akari and Spitzer missions, respectively). AIBs contribute up to 10% of the power output, and 20-30% fo the total IR luminosity in star-forming galaxies (Joblin & Tielens, 2011). Because of the wavelength proximity of the emissions involving single or group bounds, those emisisons stack up producing very high integrated fluxes. The main responsable of band broadening is vibrational anharmonicity. PAH cooling process must be also detectable in all the infrared bands from near-IR to far-

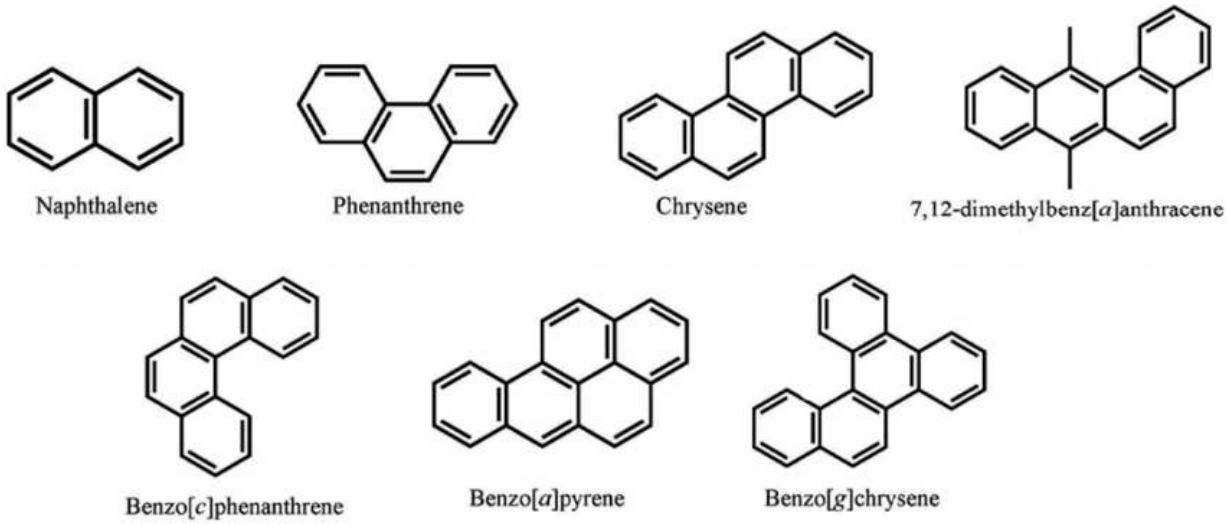

Figure 1.5: Example of PAH organic molecules. Image taken from Fetzer (2016).

IR, but modeling under those extreme densities and non-thermal equilibrium environments is still under development.

1.4.1 The 3.3 and 3.4 micron PAH features

The bluer-wavelength member of the PAH AIBs is an emision band at about 3.3 μm with a prominent peak centered at 3.28 μm. This particular feature has been extensively obverved in planeatry nebulae and HII regions (Tielens, 2008), in the general ISM (Giard et al., 1988), ultra-luminous infrared galaxies (Imanishi et al., 2010; Ichikawa et al., 2014), and into AGN circumnuclear environments (Castro et al., 2014; Esquej et al., 2014). This feature is also evidence of recent star formation and its a useful discriminator between star formation and an Seyfert activity in galactic nuclei. The intensity of this emission feature is found to be correlated to the stellar contribution but not to the thermal dust implying that they are mutually unrelated (Moorwood, 1986).

The main PAH infrared emission features (3.3, 3.4, 6.2, 7.7, 8.6 and 11.25 μm) have been attributed to UV fluorescence in molecular mantles on cold dust grains (Allamandola et al., 1979; Dwek et al., 1980). PAH molecules can be excited by an UV radiation field but under the proper physical conditions they can remain

without beeing destroyed enhancing excitation, vibrational transitions, photofragmentation and posterior thermal cooling resulting in the known PAH emission complexes in the IR band.

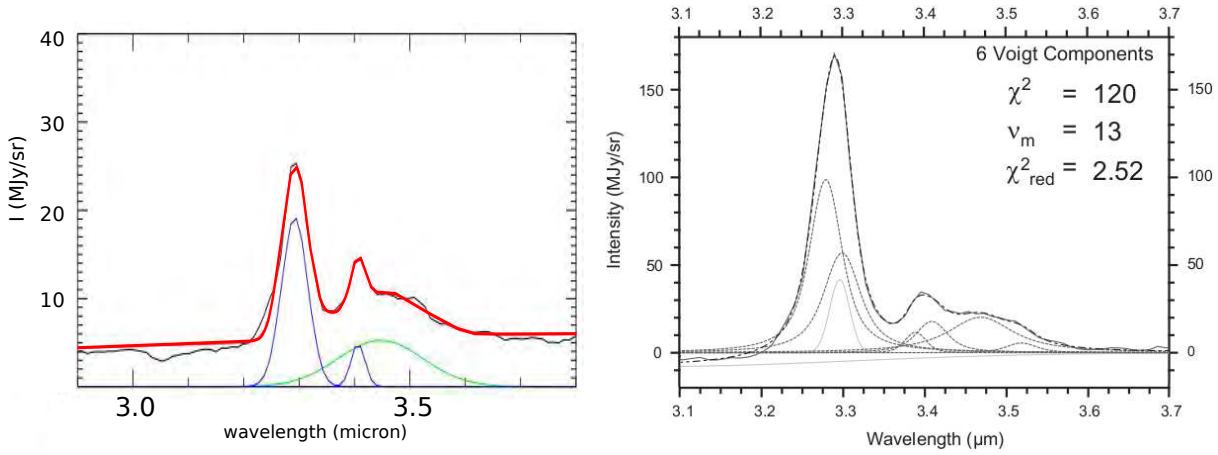

Figure 1.6: Two different fittings of the 3.3 μm complex: (left) 3 Gaussian model (Pilleri et al., 2015) and (right) 6 Voigt functions (Hammonds et al., 2015)

From a study of the HD 44179 nebula Song et al. (2003) proposed that the complex 3.3 μm band is composed of two blended sub-features at 3.28 μm and 3.30 μm and later supported by Candian et al. (2012). A weak side band is frequently detected at 3.4 μm, commonly accepted as an aliphatic hydrocarbon emission feature along this 3.3 μm band complex. Recently, Pilleri et al. (2015) proposed a 3 Gaussian components model the 3.3–3.4 PAH emission band. They used two narrow components with central wavelengths at 3.29 μm, 3.40 μm and a third broad component at 3.45 μm (see Figure 1.6/left). From their results we can see that fitting Gaussing profiles to the 3.3 μm feature is not enough being the lower part of the profile too wide and not well fitted. In addition, because Lorentzian profile are usually related to molecular emission bands, Hammonds et al. (2015) tested the Pilleri et al. (2015) 3 Gaussian model by using 6 Voigt functions to represent these PAH bands (see Figure 1.6/right). From their test using a sample of 63 Akari/IRC observations Hammonds et al. (2015) found that in many of the cases the 3.28 μm component is the dominant PAH carrier in the 3.3 μm complex. They also found that the inclusion a of second component at 3.30 μm matches the measured flux with a very good agreement supporting the hypothesis of Song et al. (2003). Further conclusions from this work are limited by spectral resolution, physical justification and statitistical

issues regarding the 3.4 μm sub-peak. Nevertheless, this method provides a precise approximation to the integrated flux of this AIB.

Chiar et al. (2000) reported a 3.28 μm band absorption towards the galactic center due to hydrogenated amorphous carbon (i.e. alkene). It has been also proposed by Dartois (2007) that the aliphatic content of the cold ISM could be the responsible of this IR absorption. In addition, 3.4 μm bare carbonaceous dust absorption has been reported in LIRGs and ULIRGs (Imanishi et al., 2010). According to Menella et al. (2001) this 3.4 μm dust absorption feature is absent from ice-covered dust grains. Other absoprtion features are also found in the 2.5–5 μm, including the narrow 4.26 μm CO_2, 4.67 μm CO and the broad H_2O 3.1 μm absorption features. The last feature overlap with the 3.3 μm complex and proper steps have to be taken in order to deblend from the PAH emission and the local continuum.

1.4.2 The 11.3 μm PAH feature

Another extensively studied emission lines in the mid-IR is the 11.3 μm PAH. Diamond-Stanic & Reike (2010) showed that the 11.3 μm PAH is a reliable indicator of the SFR in Seyfert-like AGN luminosities and kpc scales, while the 6.2, 7.7, and 8.6 μm features appear to be slightly suppressed (see Figure 1.7). This PAH emission is detected in the vicinity (ten to a few hundred parsecs) of the harsh environments of some AGN (Alonso-Herrero et al., 2014; Esquej et al., 2014; González-Martín et al., 2013). In some sources PAH molecules seem not to be completely destroyed near the AGN. In some way, they must be shielded from the AGN central engine radiation by molecular material with sufficient X-ray absorbing column densities or the accretion of new material must be enough to keep a dynamical equilibrium between PAH destruction and replenishment.

In particular, based in Gran Telescopio Canarias (GTC) high-resolution spectrography of a sample of 29 Seyfert galaxies drawn from the AGN Revised Shapley-Ames catalog (Esquej et al., 2014) found no evindence of strong suppression of the nuclear 11.3 μm PAH feature in the vicinity of the AGN, at least for the Seyfert-like AGN luminosities and physical nuclear regions (65 pc median value). In addition, they do not see a tendency for the equivalent width (EW) of the PAH to decrease for more luminous AGN. They also

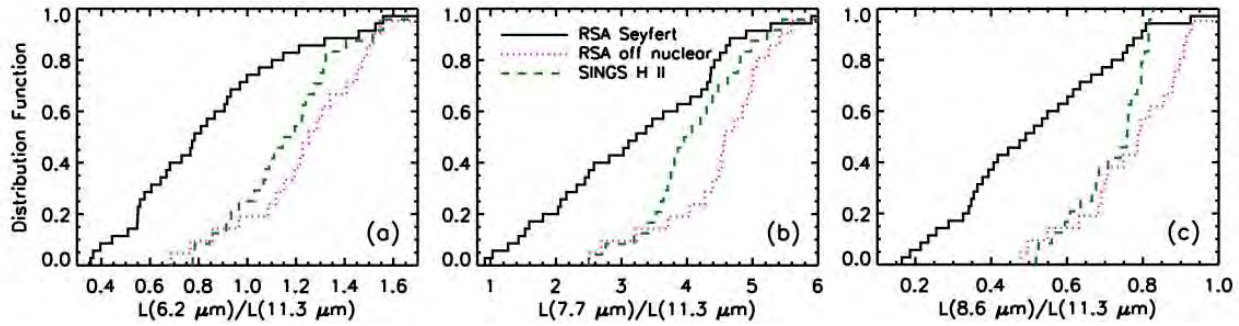

Figure 1.7: Diamond-Stanic & Reike (2010) show that the 6.2, 7.7, and 8.6 μm features are systematically weaker relative to the 11.3 μm feature for the Seyfert nuclei than for the off-nuclear regions or the Spitzer Infrared Nearby Galaxy Survey (SINGS; Kennicutt, 2003) HII galaxies.

measure significant reduction of the 11.3 μm PAH flux from circumnuclear ($\sim$600 pc) to nuclear regions ($\sim$65 pc), with a typical ratio of $\sim$5. However, the average SFR rate density in the nuclear regions of their sample is approximately 20 higher than in the circumnuclear regions. Indicating a highly concentrated star-forming activity in the nuclear regions in the studied sample of Seyfert galaxies.

In a similiar study, Alonso-Herrero et al. (2014) using GTC CanariCam 8.7 μm imaging and 7.5–13 μm spectroscopy of six local galaxies hosting AGNs, detected nuclear (inner $\sim$60–420 pc) and extended (a few hundred pc from the AGN) 11.3 μm PAH feature emission in all the AGNs. In their sample, the nuclear EW of the 11.3 μm PAH feature are always lower than those measured from Spitzer/IRS spectra (Diamond-Stanic & Reike, 2010) probing circumnuclear regions, which are typically factors of 7 larger in size than the nuclear regions. They explained the reduced nuclear EW of the 11.3 μm PAH feature as due to an increased AGN continuum contribution in the nuclear regions rather than destruction of the PAH carriers by the AGN radiation. Alonso-Herrero et al. (2014) conclude that the 11.3 μm PAH feature can be used as a proxy of the nuclear star-formation for Seyfert-like AGNs at least to distances to the AGN as close as 10 pc, assuming that the AGN contribution to the excitation of the 11.3 μm PAH feature is small or negligible.

1.5 Objectives

The main objective of this work is to investigate the relation between AGN activity and circum-nuclear SF activities. We use hard X-ray (14–195 keV) selected AGNs from the Swift/BAT survey as least biased sample of bright AGNs. We choose PAH features as proxies of star-formation and investigate the relation between AGN power and SFR. We also investigate the AGN type (Seyfert type 1 vs type 2) and the SFR to see if these two types have an intrinsic difference in their circum-nuclear environments.

We conduct a comparative study of the near- to mid-IR spectroscopic properties, with a focus on PAH features, of a sample of X-ray selected AGNs from the Swift/BAT 70-month all-sky hard X-ray (14–195 keV) survey. During the first stage, we use an early sample of 54 X-ray selected AGNs also observed with the Akari/IRC instrument in the near-IR band. In our second stage, we extend our X-ray selected sample to the mid-IR band including all the Spitzer/IRS observed Seyfert sources from the Swift/BAT 70-month catalog. This extended sample is integrated by 130 AGNs. QSO sources included in the early near-IR sample are excluded in the extended mid-IR sample and restricted to $z < 1$.

We use the 3.3 and 11.3 μm PAH emission lines detected in our spectral range as proxies for the circumnuclear star-forming activity in order to explore correlations between AGN activity, column densities towards the nucleus (when available), AGN type, and SFR.

CHAPTER 2

X-RAY SELECTED AGNS

The Swift Gamma-ray burst (GRB) observatory (Gehrels et al., 2004) was launched in November 2004, and has been continually observing the hard X-ray (14–195 keV) sky with the Burst Alert Telescope (BAT). The BAT instrument is a highly sensitive, large field-of-veiw (FOV) instrument designed to provide critical GRB triggers and 4-arcmin positions. The BAT survey provided long-term broadband spectroscopic monitoring with near 70% sky coverage each day. Within several seconds of detecting a burst, the BAT calculates an initial position and decides whether to observe it or not. This capability allowed transient detections within minutes and inmediate follow up with the onboard X-ray Telescope (XRT). When a burst is detected, the sky location and intensity are immediately sent to the ground and distributed to the community through the Gamma-Ray Burst Coordinates Network (GCN; Barthelmy et al., 2000)

While the main objective of the Swift mission is to observe GRBs, its BAT instrument keeps accumulating hard X-ray photons during slew manuevers, producing an all-sky hard X-ray map. With its coded mask, the X-ray source can be localized with a $\sim$4 arcmin position accuracy. Thus, while searching for bursts, the BAT performs an all-sky hard X-ray survey and monitors for hard X-ray transients. The BAT team published BAT survey catalogs covering the first three months of data Markwardt et al. (2005), AGN detected in the first 9 months of data Tueller et al. (2008), 22-month (Tueller et al., 2010) and 70-month (Baumgartner et al., 2013). Details of the BAT surverys are shown in Figure 2.1(*right*).

Many AGNs have absorbing columns enough to hide them from the line of sight in other IR, optical, UV and soft X-ray. This is because this kind of surveys suffer from attenuation due to the obscuring material

present in the AGNs (see also Awaki et al., 2000). Therefore, the Swift/BAT survery allows us to include sources with larger obscurations (e.g. more Seyfert 2 sources) even up to moderately CTK column densities ($\log(N_H)[cm^{-2}] \leq 25$). These very hard X-ray surveys provide an efficient way of constructing a clean and highly unbiased sample.

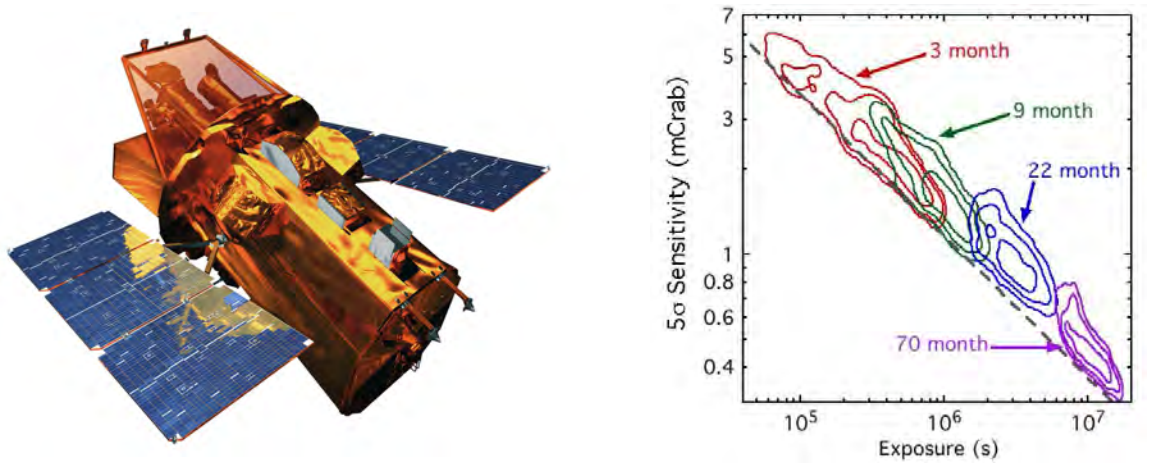

Figure 2.1: (*Left*) The Swift GRB observatory Gehrels et al. (2004) was launched in November 2004. (*Right*) Measured 5-σ BAT sensitivity limit for pixels in the all-sky map, as a function of effective exposure time, T, for the 3-month (red; Markwardt et al., 2005), 9-months (green; Tueller et al., 2008), 22-months (blue; Tueller et al., 2010) and 70-months (red; Baumgartner et al., 2013) surveys. Right image taken from Baumgartner et al. (2013).

2.1 The Swift/BAT 70-month Catalog

The main advances of the Swift/BAT 70-month survey compared to previous Swift/BAT surveys (9-months, Markwardt et al. (2005); 22-month ,Tueller et al. (2008) and 58-month (Baumgartner et al., 2013) include better sensitivity resulting from a complete reprocessing of the data with an improved data reduction pipeline, the publication of 8 channel spectra, lightcurves sampled every month throughout the mission, and a lower flux threshold resulting from nearly a factor of three more integration time.

The Swift/BAT 70-month survey has compiled a uniform catalog by using a well-defined significance threshold and energy band for inclusion of sources into the catalog. Particular attention has been paid to the identification of sources, for which examination of 3–10 keV X-ray data is crucial. The BAT survey

catalogs of Cusumano et al. (2010a) and Cusumano et al. (2010b) often base their counterpart identification on nearby ROSAT sources; Tueller et al. (2010) have shown that the soft X-ray (0.1–2 keV) ROSAT fluxes are not well correlated with BAT fluxes and could lead to incorrect counterpart associations, especially in the galactic plane. The BAT catalogs of Ajello et al. (2012), Burlon et al. (2011) and Voss & Ajello (2010) often use the counterpart associations of Cusumano et al. (2010b), and utilize only part (15–55 keV) of the full BAT energy band (14–195 keV).

The all-sky Swift/BAT 70-month survey detected 1171 hard X-ray sources in the 14–195 keV band down to a significance of 4.8σ. The majority of the sources in this survey are AGNs. In particular, it includes 292 Seyfert I (1.0–1.5) and 261 Seyfert II (1.7–2.0), 49 blazars, and 86 QSOs. We selected all the Seyfert sources with available Spitzer/IRS and Akari/IRC data available that meet the criteria stated in this Chapter.

2.2 Sample selection

2.2.1 The early sample

In a first stage of the research, we investigated the 2.2–5 μm low-resolution (R$\sim$120) spectra obtained with the InfraRed Camera (IRC) instrument on the space infrared observatory Akari for a sample of 54 AGNs (the 'early sample'; see Castro et al. (2014)) with various levels of obscuration selected from the 9-month catalog (Tueller et al., 2008) of the Swift/BAT survey, which is sensitive to very high X-ray energies (14–195 keV). Our selected sample also has detailed X-ray spectroscopy (0.3–12 keV; Winter et al., 2009; Ichikawa et al., 2012a). For all objects in our sample X-ray-derived N_H were obtained mainly by analyzing spectra from the XMM-Newton, ASCA, Suzaku, and Swift X-ray/XRT. Infrared 2.2–5 μm spectroscopy is a powerful tool for the diagnosis of buried AGNs, because the effect of dust extinction is relatively small in comparison with optical bands (Imanishi et al., 2010). It allows a study of sources in which both an AGN and a starburst (SB) are present.

Thirty-two Akari/IRC observed AGNs are from our own observations made as a part of the "AGNUL" (AGN and ULIRG) group proposal for the Akari Mission Program 3 (MP3), which covers the post-helium

phase of the Akari mission. In the fist cycle of MP3, we have selected our objects among highly absorbed AGNs ($\log(\mathrm{N_H}) > 23.5[\mathrm{cm}^{-2}]$) and well-known bright AGNs. In the second cycle, we selected our targets such that the sample is spread over all $\log(\mathrm{N_H})$ levels. The remaining 22 have been observed by other groups and we obtained the data from public archives.

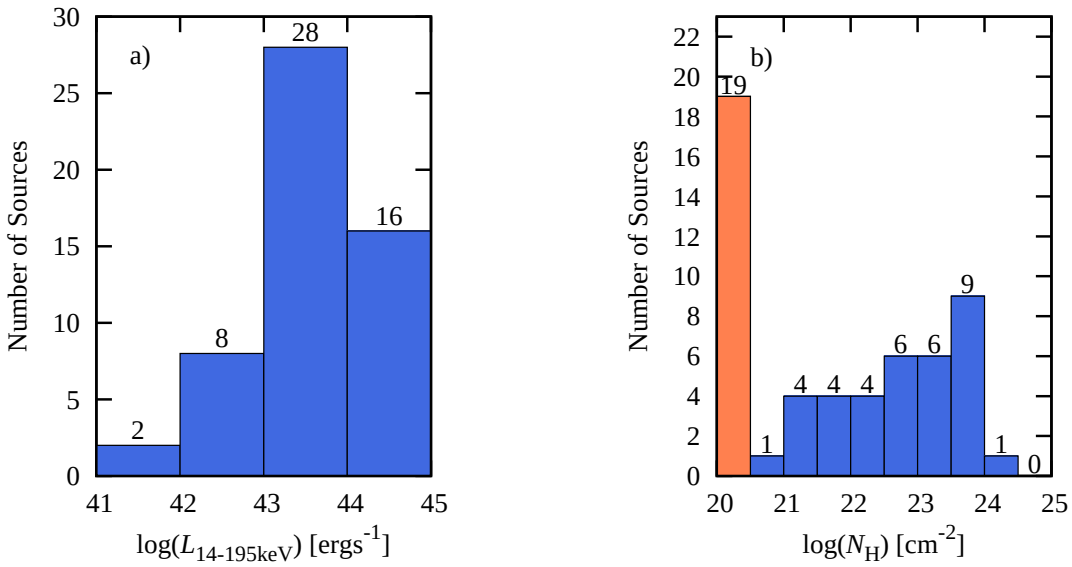

Figure 2.2: (*a*) Distribution of the $\log(\mathrm{L_{14-195keV}})$ of the sample. (*b*) Distribution of the absorbing column density ($\mathrm{N_H}$ in units of cm^{-2}) obtained from softer X-ray ($\mathrm{E} < 10$ keV) spectra of our sample (Winter et al. (2009); Ichikawa et al. (2012a)).

The archival data that we have used for our analysis were from observations with the same instrumental configuration. We intended to obtain spectra of almost all remaining non-blazar AGNs in the 9-month Swift/BAT catalog during the third cycle of the MP3 program. However, it became impossible due to the unfortunate failure of the mechanical cryogenic cooler on board Akari, which happened in the winter of 2010. While obtaining spectra for all the AGNs in a complete sample is desirable, the selection criteria of our current sample are mainly based on the X-ray absorption (first cycle) and visibility considerations (both cycles), rather than the far infrared properties or any star-formation indicator. From the abstracts of the proposals of the observers of the archival data show we checked that they did not select based on star-formation indicators.

In our early sample (see table 3.1), 26 AGNs are optical type 1 AGNs (Seyfert optical type ≤ 1.5) and

28 type 2 AGNs (Seyfert optical type > 1.5). This selected sample also has detailed X-ray spectra from the XMM-Newton, Chandra, ASCA, Suzaku, and Swift/XRT in $0.3 \lesssim \mathrm{E[keV]} \lesssim 12$ (Winter et al., 2009; Ichikawa et al., 2012a). The distribution of $\log(\mathrm{L}_{14-195\ \mathrm{keV}})$ for the overall sample is shown in figure 2.2(*a*). For all objects in our sample X-ray-derived $\mathrm{N_H}$ were obtained from these spectra. Figure 2.2(*b*) shows the $\mathrm{N_H}$ distribution of the sample. In the cases where N_{H} value is not explicitly provided by Winter et al. (2009) (in those cases where the original X-ray spectra were well fit by a simple absorbed power law model and thus, consistent with a un-absorbed AGN) we took the $\mathrm{N_H}$ value from Ichikawa et al. (2012a).

2.2.2 The extended sample

In a second stage of the present research we have extended our X-ray selected sample to the mid-IR band including all the Spitzer/IRS observed Seyfert sources (the 'extended sample'; see Figures 2.4 and 2.5 at Section 2.2.2) from the Swift/BAT 70-month catalog [1] (Baumgartner et al., 2013) in the 14-195 keV range. This extended sample is integrated by 130 AGNs (see Figure 2.3 for further details). The power-strength of the 11.3 μm PAH feature detected in our mid-IR spectral range is also used as a reliable proxy for the SF activity.

Our extended mid-IR sample is integrated by 130 AGNs with z < 0.1 and $42 \leq \mathrm{L}_{14-195\mathrm{keV}} \leq 45$. Details on the hard X-ray flux and luminosities plotted against redshifts are shown in Figure 2.3(*right*). All of those sources were selected from the Swift/BAT 70-month survey and have low-resolution ($\sim$ 60–120) Spitzer/IRS spectral in the $\sim$5–12 μm range. All the archival data that we have used for our analysis were from observations with the same instrumental configuration. A red-filter mosaic of images obtained from the Digital Sky Survey (DSS) is shown in Figure 2.7 as a reference to the reader of the studied sources.

Although our first criterion was to choose galaxies classified as type Seyfert in the Swift/BAT 70-month survey table we decided not to include sources below 10^{42} erg s^{-1}with the intention of reducing the number of objects with potential contamination from other X-ray emitters beside the central machine (e.g. high-mass X-ray binaries, heated plasma, supernova remnants, etc.)

[1] http://swift.gsfc.nasa.gov/results/bs70mon/

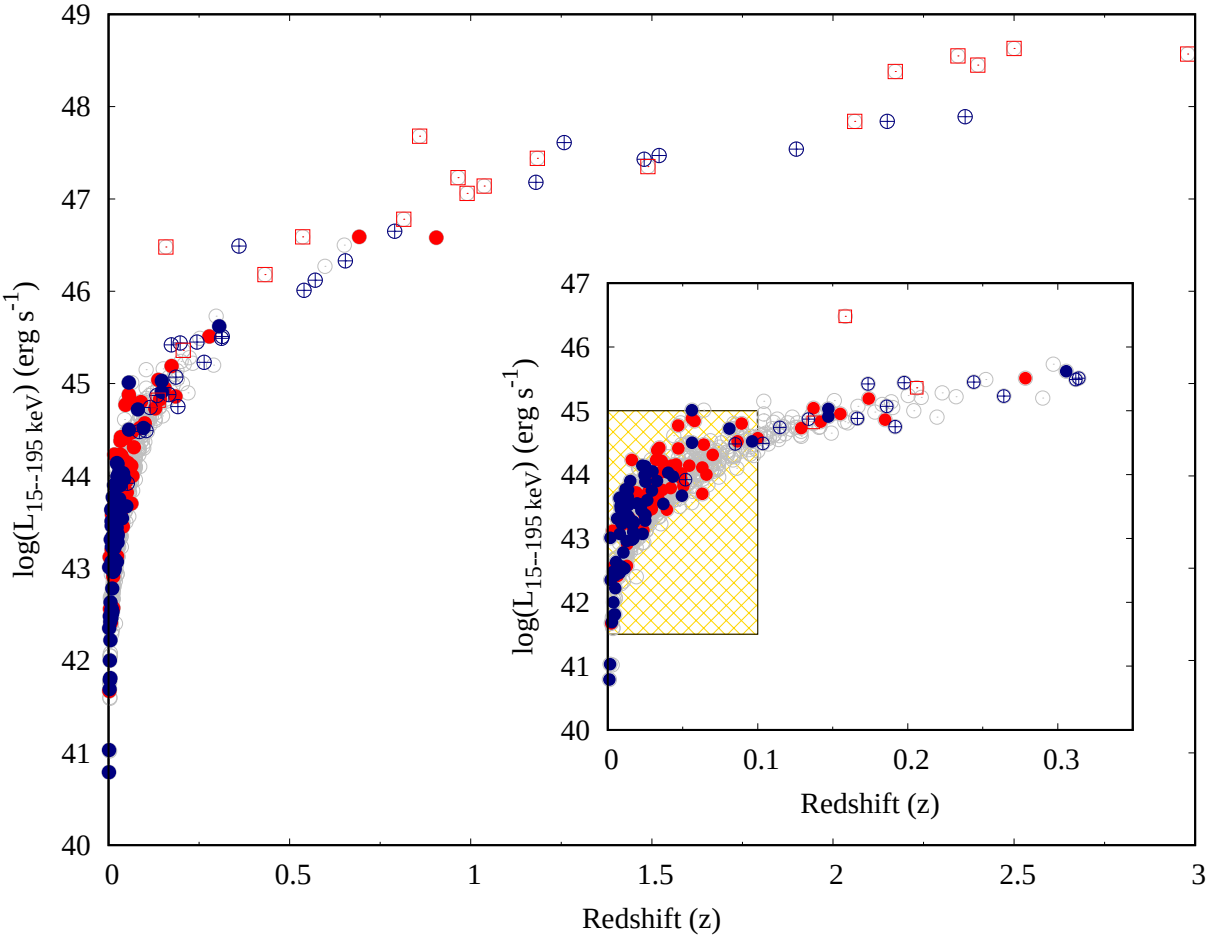

Figure 2.3: All AGNs of the Swift/BAT 70-month survey were pre-selected. Those AGNs without Spitzer/IRS spectra are kept in gray color. Blue strikethrough-circles are overplotted on QSOs and red squares are for blazar sources. Filled red circles ares for Seyfert 1 sources and filled blue circles for Seyfert 2s with Spitzer/IRS spectra available. In the right hand is shown a zoom-in region in the z = 0–0.3 redshift range. The golden cross-hatched region corresponds to the final z vs. $\log(\mathrm{L}_{14-195\mathrm{keV}})$ region of interest of the present work. Our selection includes only Seyfert-type sources. The optical type was taken from the Swift/BAT 70-month website.

Some of those sources in this extended mid-IR sample also have available public Akari/IRC archival data (with the sample intrumental configuration than the early sample) that we have used in our analysis (see Table 3.1). Also the abstracts of the proposals of the observers of the public archival data show that they did not select based on star-formation indicators. This is in contrast with other studies that use ULIRGS/LIRGS. Thus our sample enables us to probe the star formation in AGNs in an unbiased manner. For the objects with

both Akari/IRC and Spitzer/IRS observations it is possible to measure the PAH emission lines at 3.3, 6.2, 8.6, and 11.3 μm on kpc scales, as well as other emission/absoprtion features, in order to explore possible correlations in the sample.

Our extended mid-IR sample (see Table 3.2) contains 65 optical type 1 AGNs (Seyferts with optical type ≤ 1.5), and other 65 type 2 AGNs (Seyferts with optical type > 1.5). Figure 2.5(*right*) shows the redshift (z) distribution of the sample. For 69 of the objects in our selection the X-ray-derived N_H is also known. In the cases where N_H value is not explicitly provided by Winter et al. (2009) (those cases where the original X-ray spectra was well fit by a simple absorbed power-law model and thus, consistent with a un-absorbed AGN) we took the N_H value from Ichikawa et al. (2012a). WISE and IRAS photometric data were collected (see Figure 2.6) from the NASA/IRSA webpage. IRAS photometric data is used to determine the IR luminosity in the 8–1000 μm band (L_{IR}). A paper regarding the analysis of the mid-IR PAH emission features of those AGNs sample is beeing prepared.

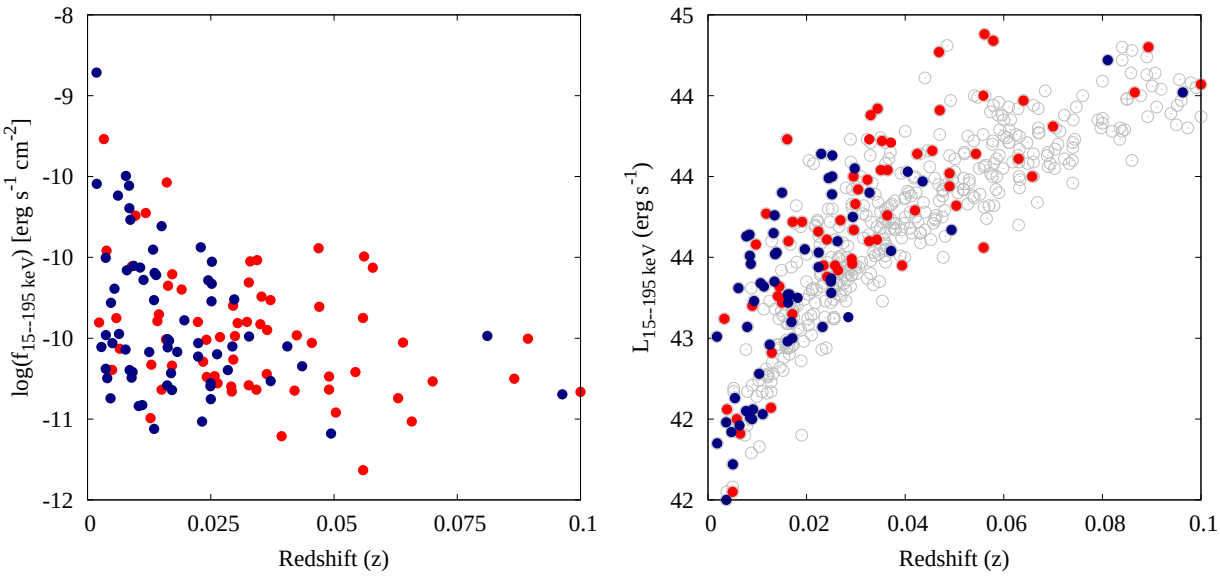

Figure 2.4: X-ray luminosity and flux of the selected sample plotted against redshift. Our final selection of Seyfert sources is on the range $0.0 \leq z \leq 0.1$ and $42 \leq \log(L_{14-195\ \mathrm{keV}}) \leq 45$. Red points are for Sy1 sources and blue navy points are for Sy2 sources.

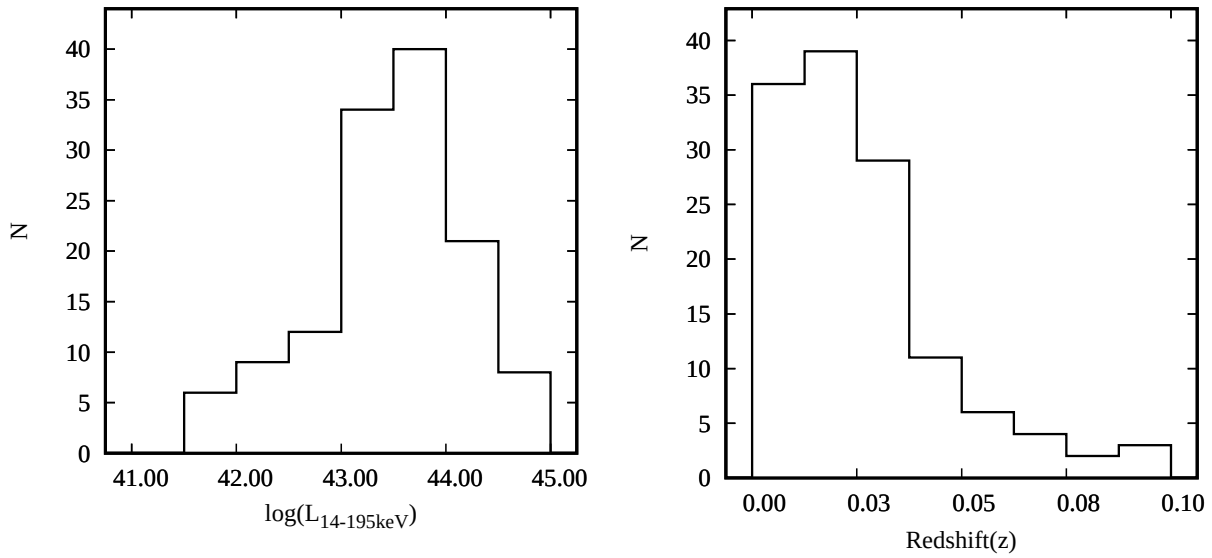

Figure 2.5: Properties distribution of the overall sample: (*left*) distribution of $\log(L_{14-195keV})$, and (*right*) z distribution of the X-ray selected sample with public available Spitzer/IRS spectra.

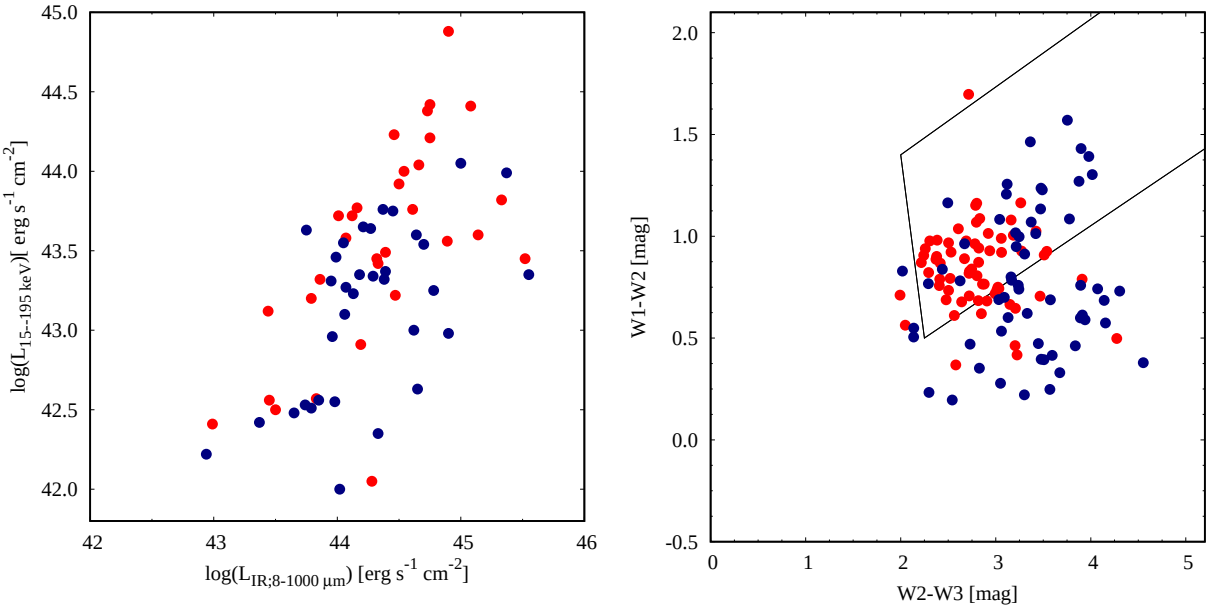

Figure 2.6: Some our X-ray selected sources have IRAS and WISE IR photometry available. L_{IR} vs. $\log(L_{14-195keV})$ (*left*) for those objects having both Swift X-ray and IRAS IR luminosities available. WISE (W2-W3, W1-W2) mid-IR color-color diagram (*right*) in units of Vega magnitude. The black lines are the Mateos et al. (2012) demarcation for mid-IR AGNs identification. Red points are for Sy1 sources and blue navy point are for Sy2 sources. Total infrared luminosity (L_{IR}:8–1000 μm) in units of solar luminosity, was calculated from $L_{IR} = 2.1 \times 10^{39} \times D(Mpc)^2 \times (13.48 f_{12} + 5.16 f_{25} + 2.58 f_{60} + f_{100})$ (Sanders & Mirabel, 1996).

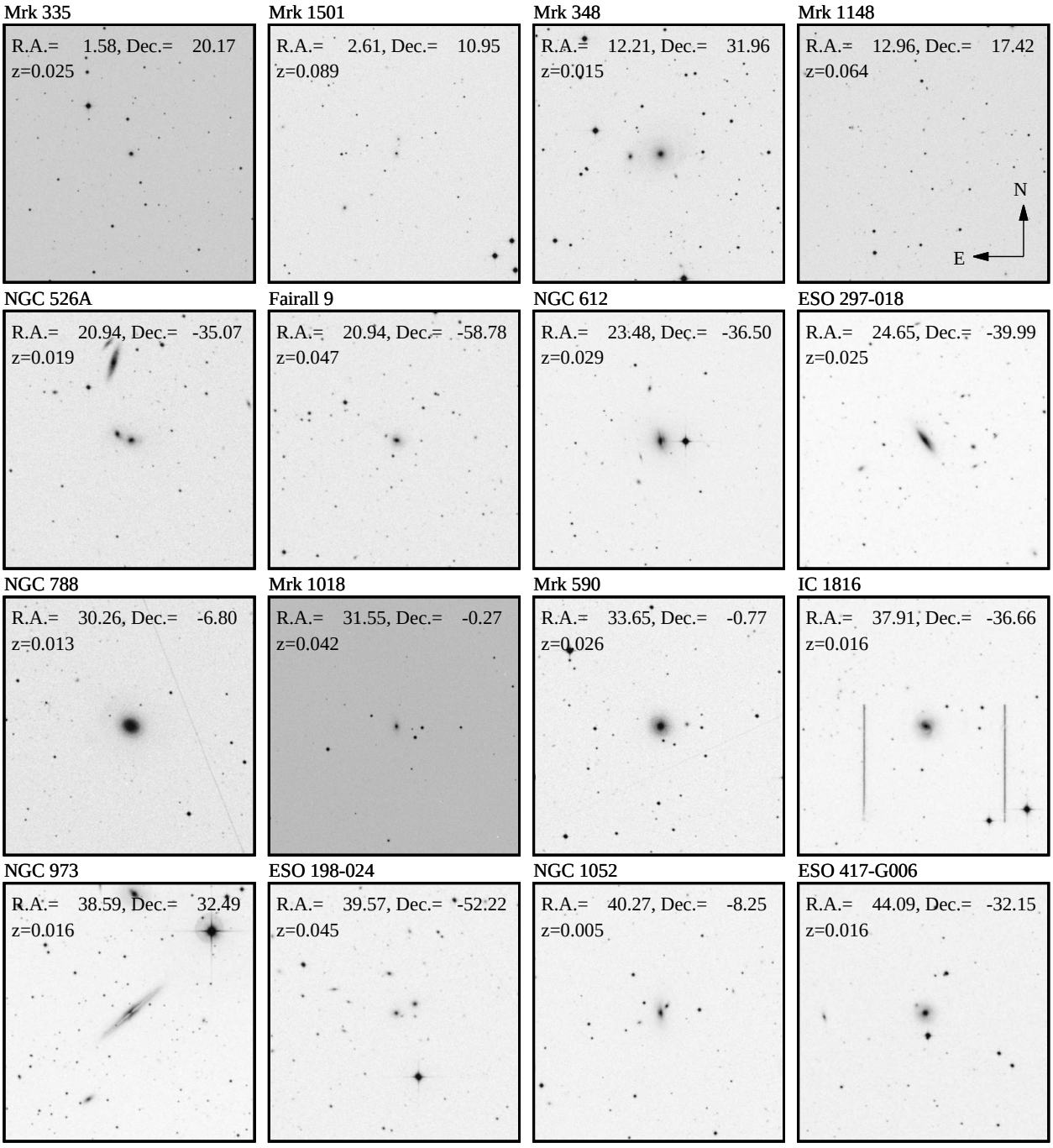

Figure 2.7: 10×10 arcmin R-filter images from the Second Digitized Sky Survey (DSS) in the field of each studied object (for illustrative purpooses). Images were downloaded through the ESO distributed dss2 script. The images of these surveys are based on photographic data obtained using the Oschin Schmidt Telescope on Palomar Mountain and the UK Schmidt Telescope.

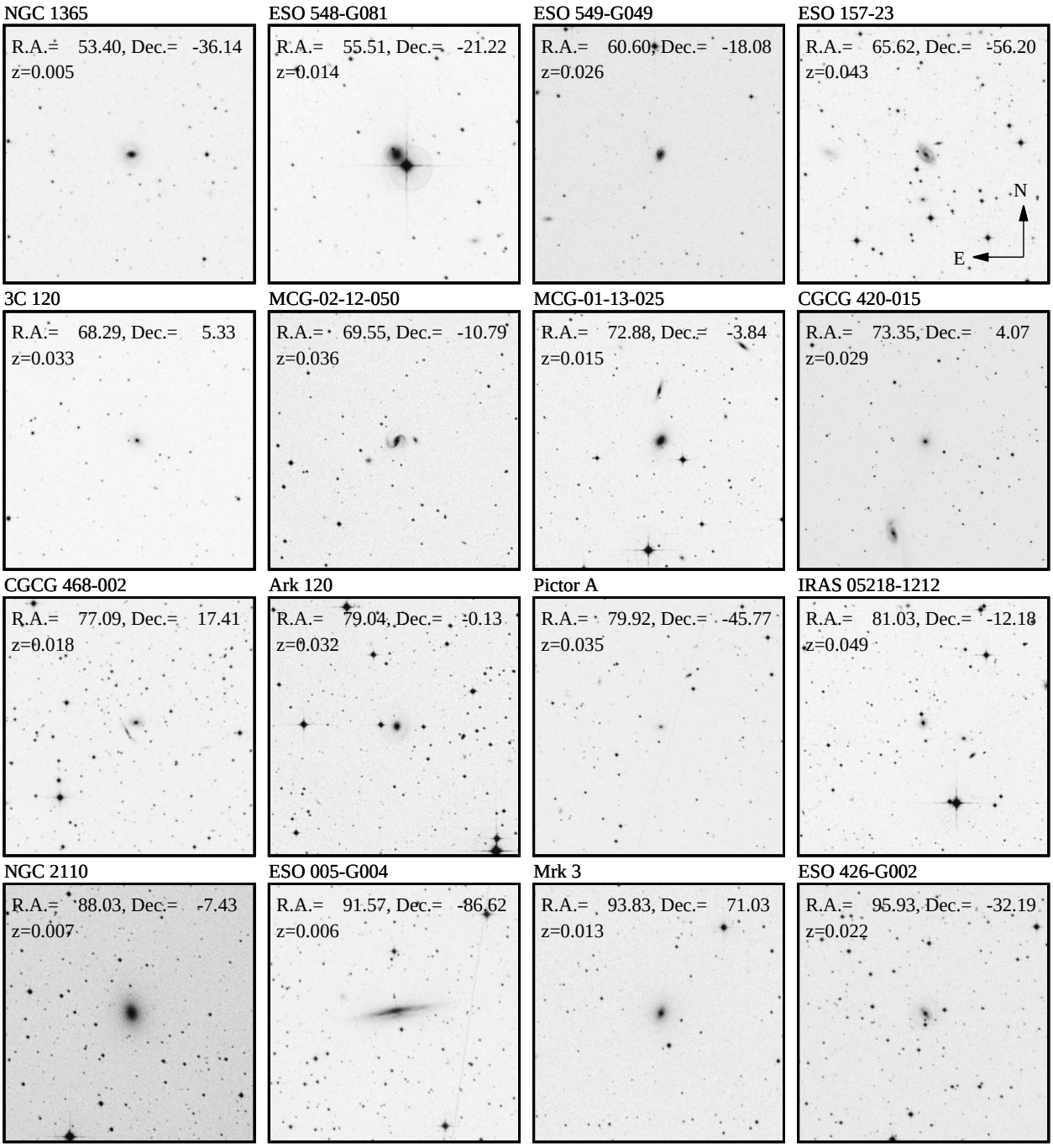

Figure 2.7: (Continued). X-ray surveys provide the most reliable method for AGN selection. Soft X-rays ($E \lesssim 10$ keV) penetrate low to moderate columns of obscuring dust and gas but miss a significant fraction of moderately obscured AGNs ($\sim 25\%$ at $N_H = 10^{23}$ cm^{-2}; Donley et al. (2012)). However, the hard X-ray Swift/BAT survery (14–195 keV) allows us to include sources up to moderately CTK column densities. ($\log(N_H)[cm^{-2}] \leq 25$).

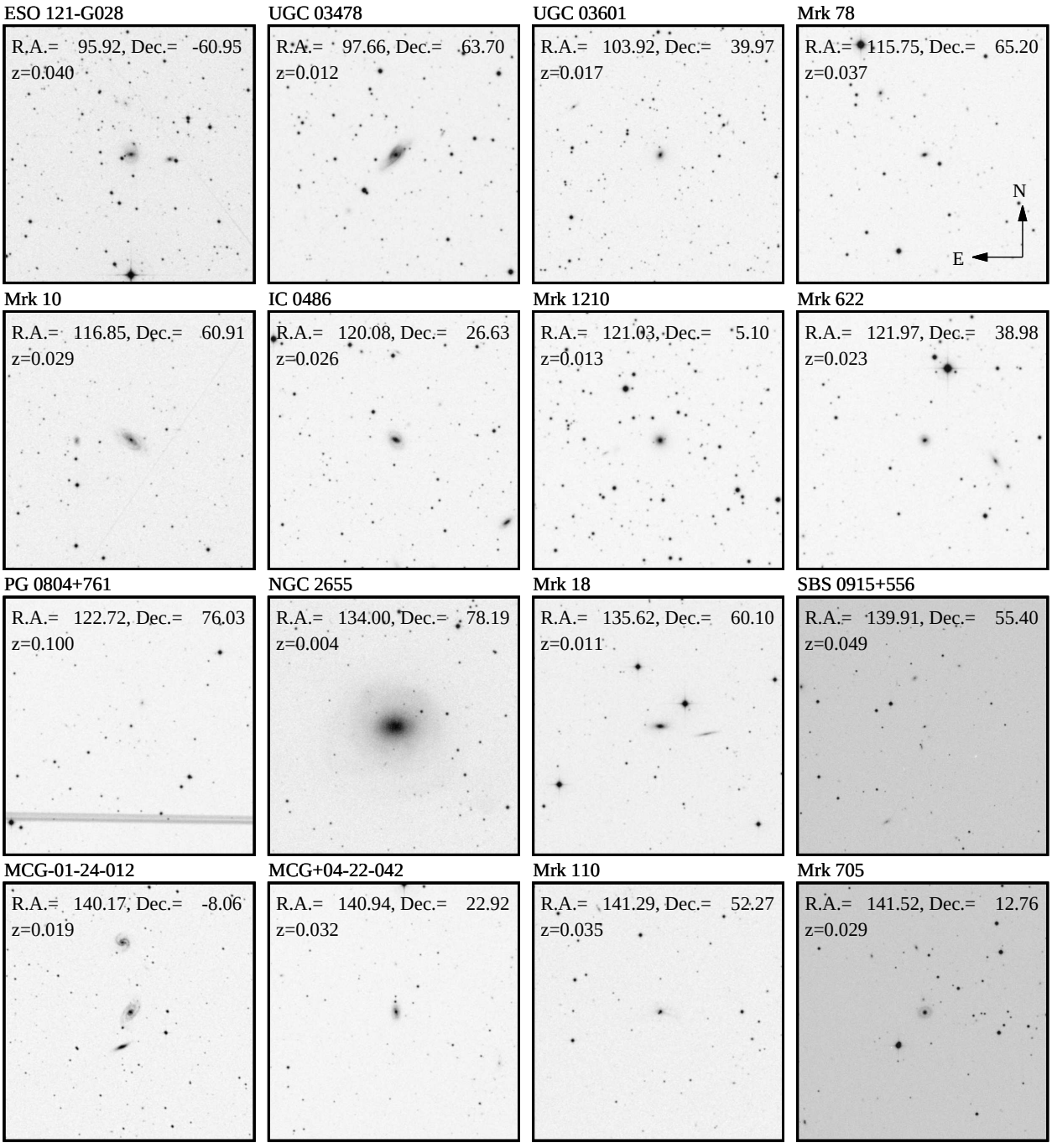

Figure 2.7: (Continued).

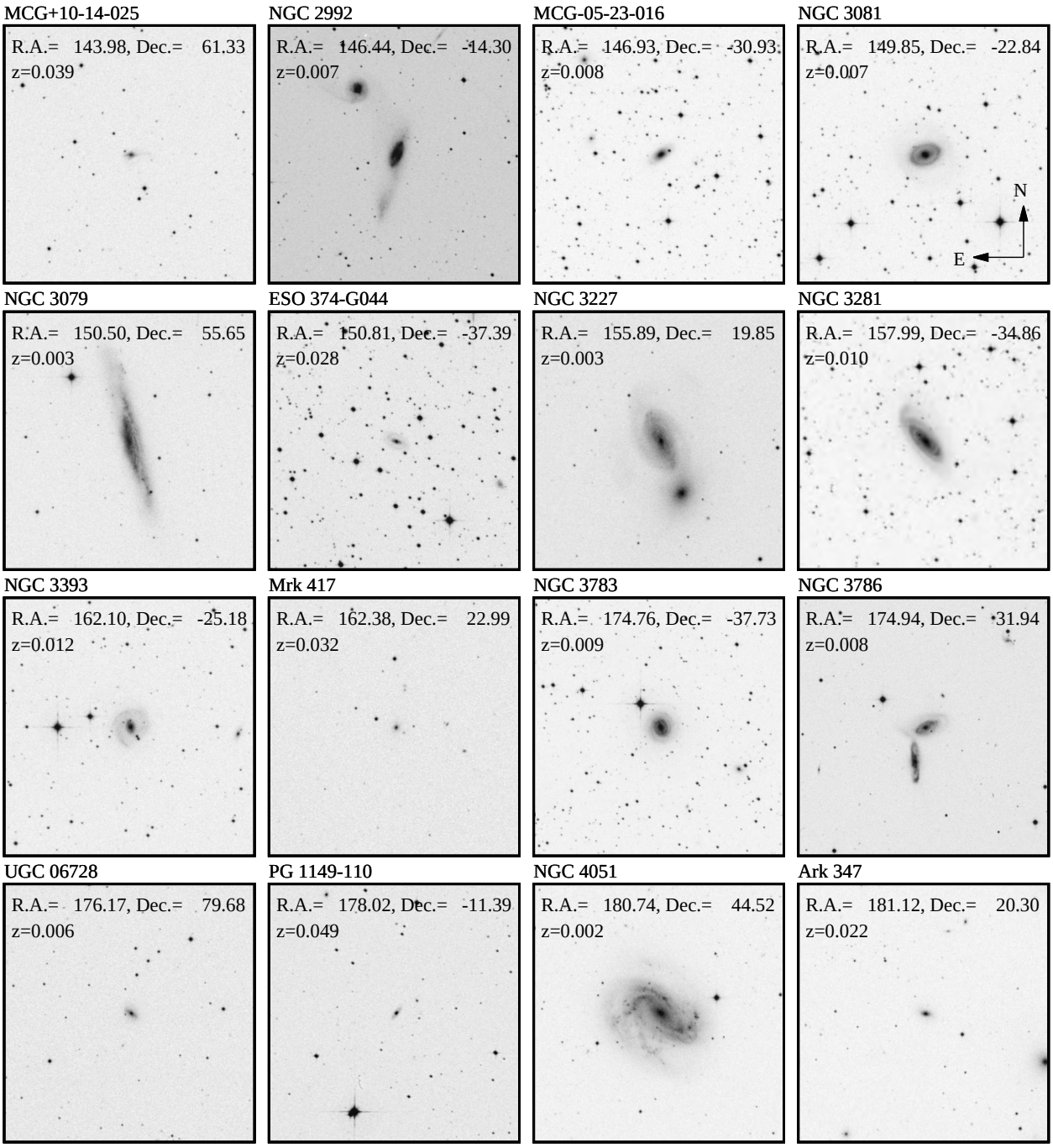

Figure 2.7: (Continued). NGC 2992 is a known galaxy pair studied in multiple wavelengths. It shows intense star-forming activity (Quillen et al., 1999), with large-scale outflows observed in Hα, [OIII]λ5007 and soft X-rays. In NGC 3227 Davies et al. (2006) found a resolved nuclear star-forming region around the Seyfert 1 nucleus, on scales of a few parsecs to a few tens of parsecs. According to them, the most recent episode of intense star formation began $\sim$ 40 Myr ago.

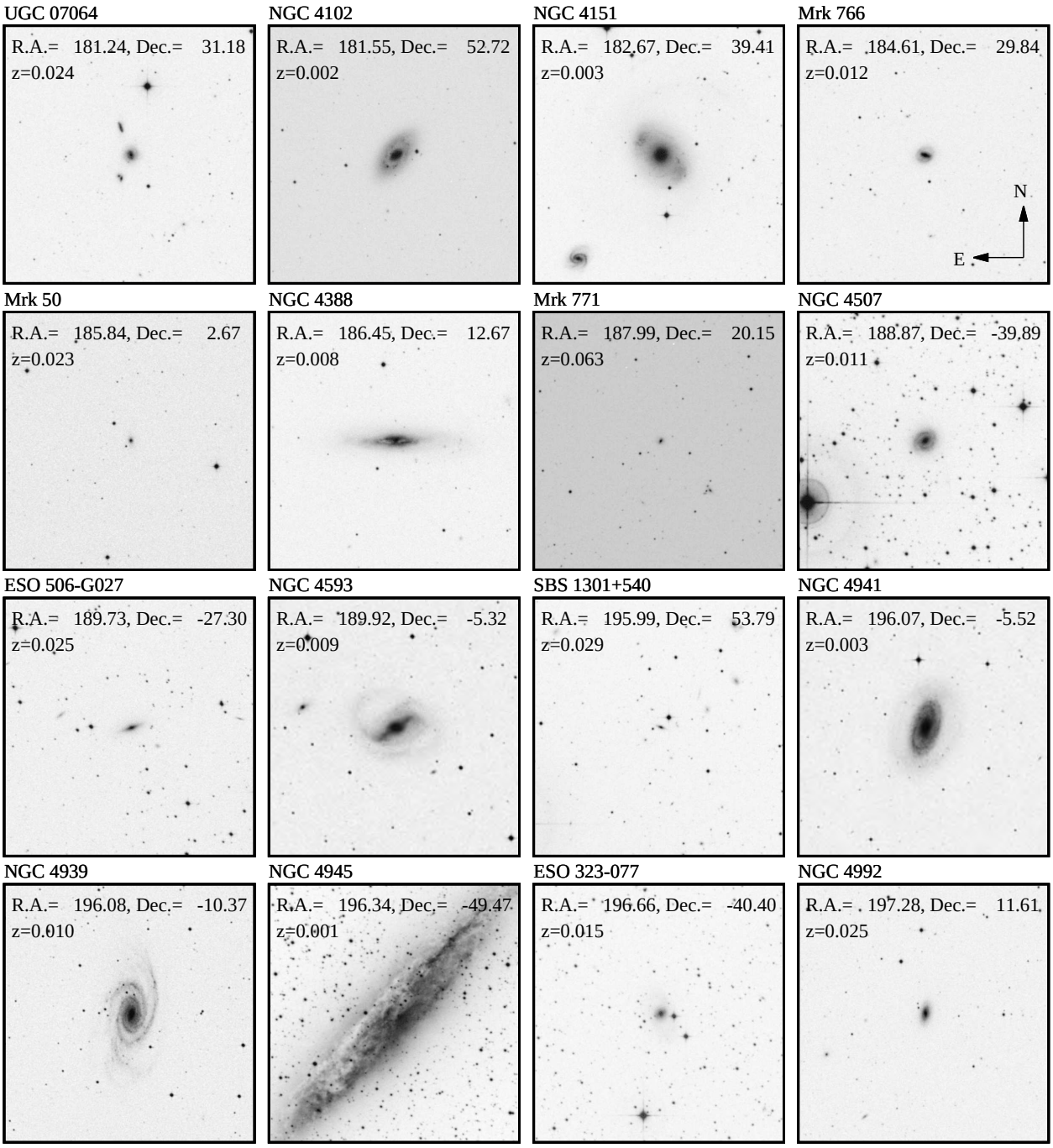

Figure 2.7: (Continued).

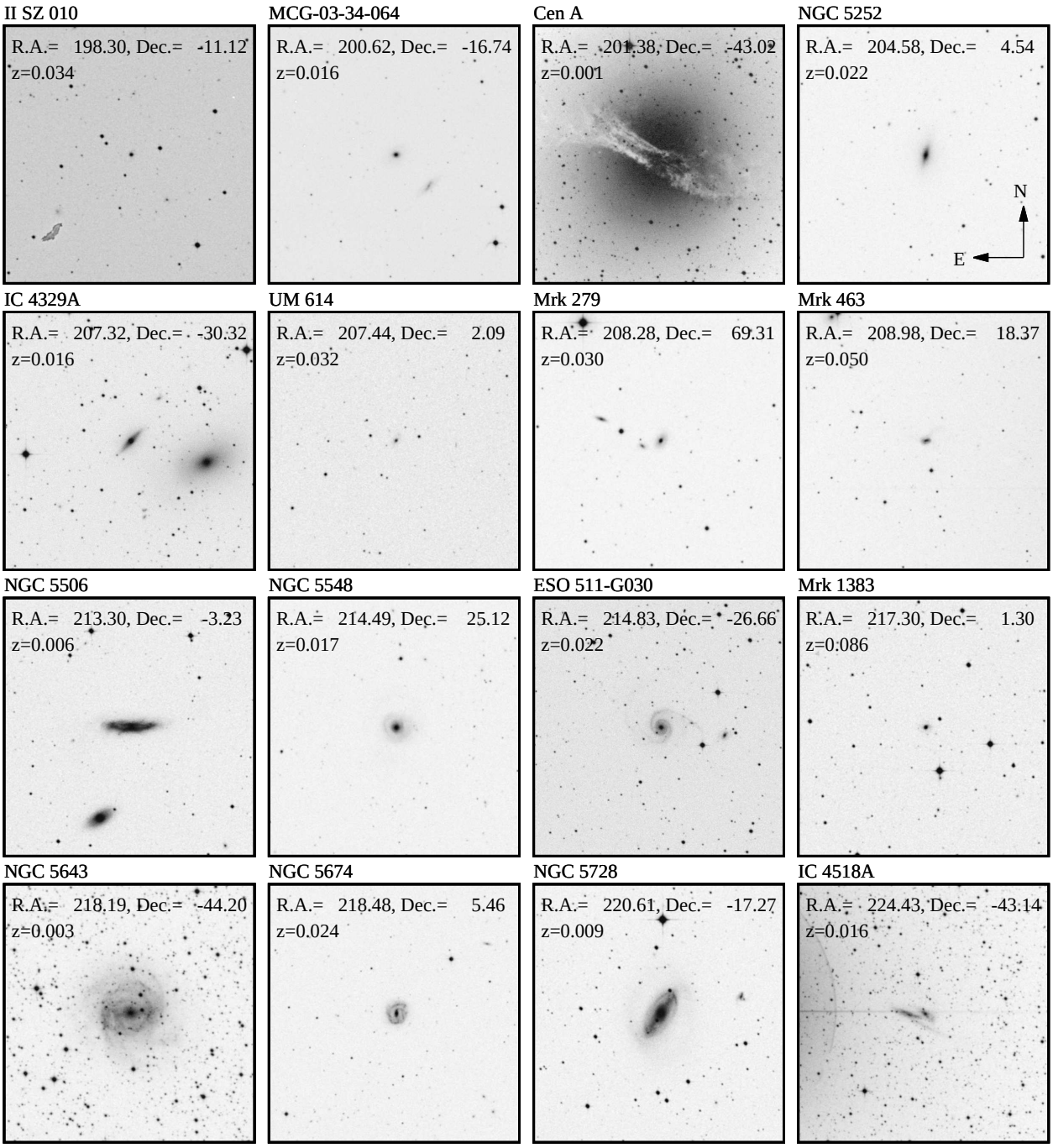

Figure 2.7: (Continued).

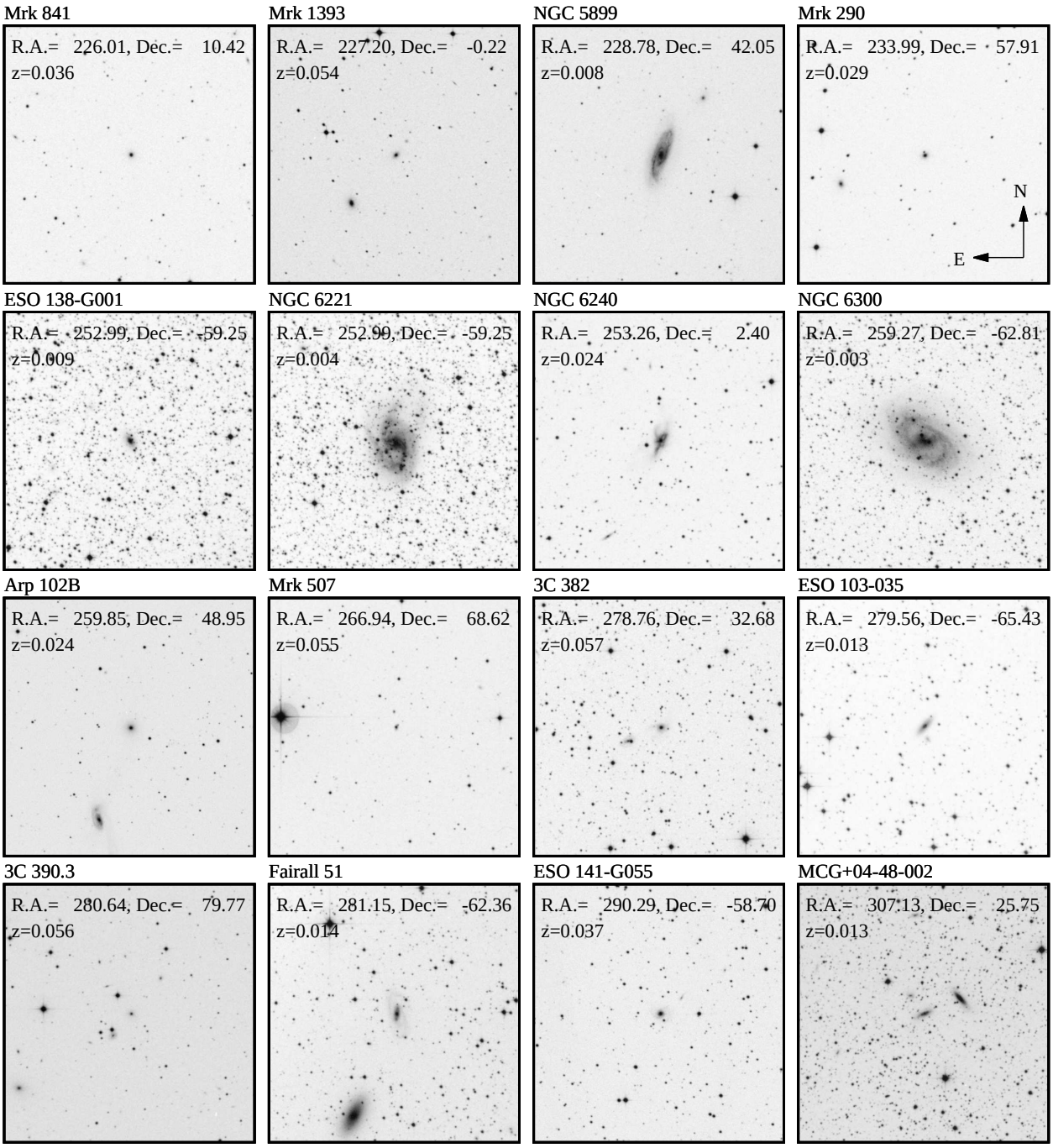

Figure 2.7: (Continued).

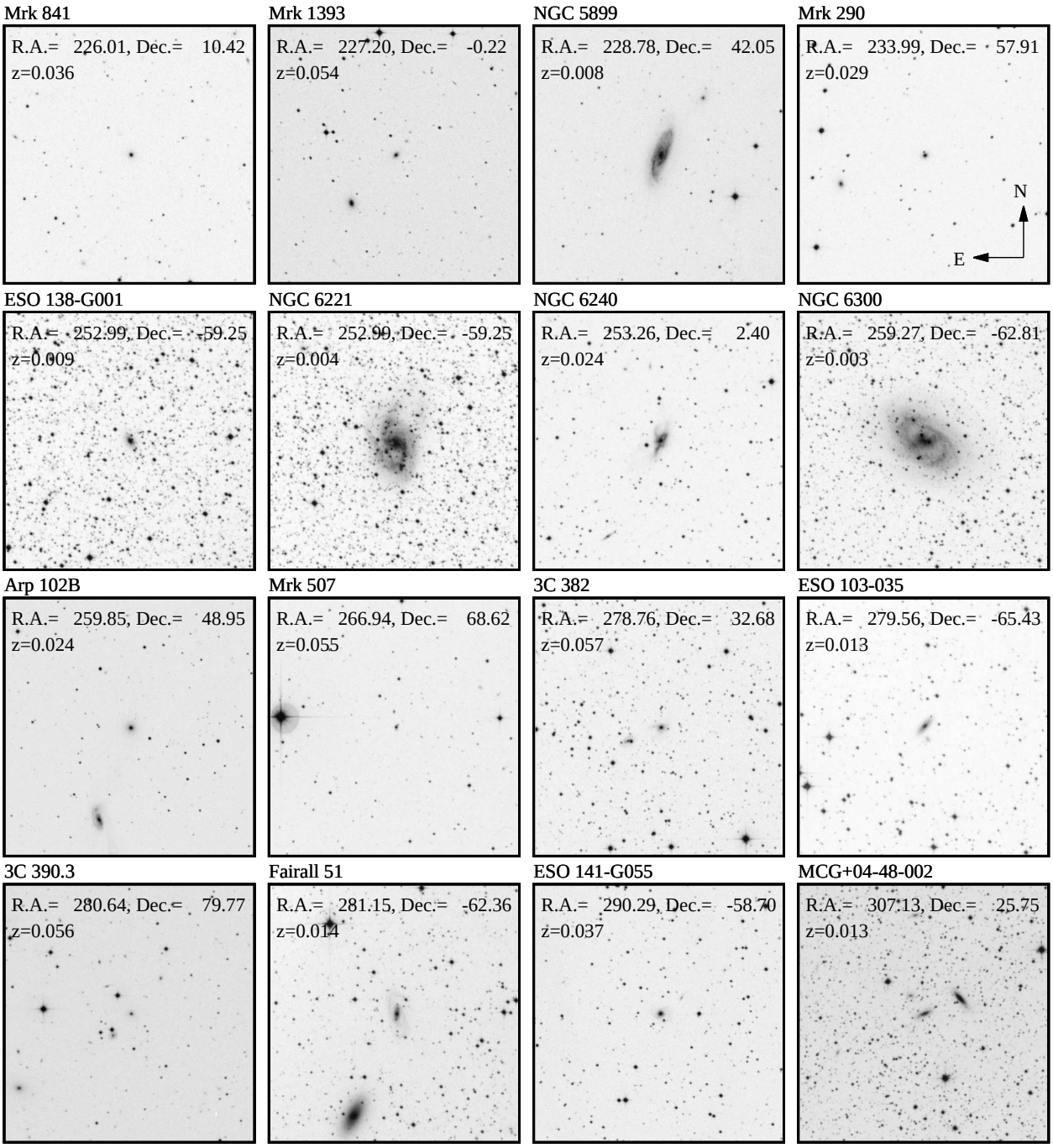

Figure 2.7: (Continued).

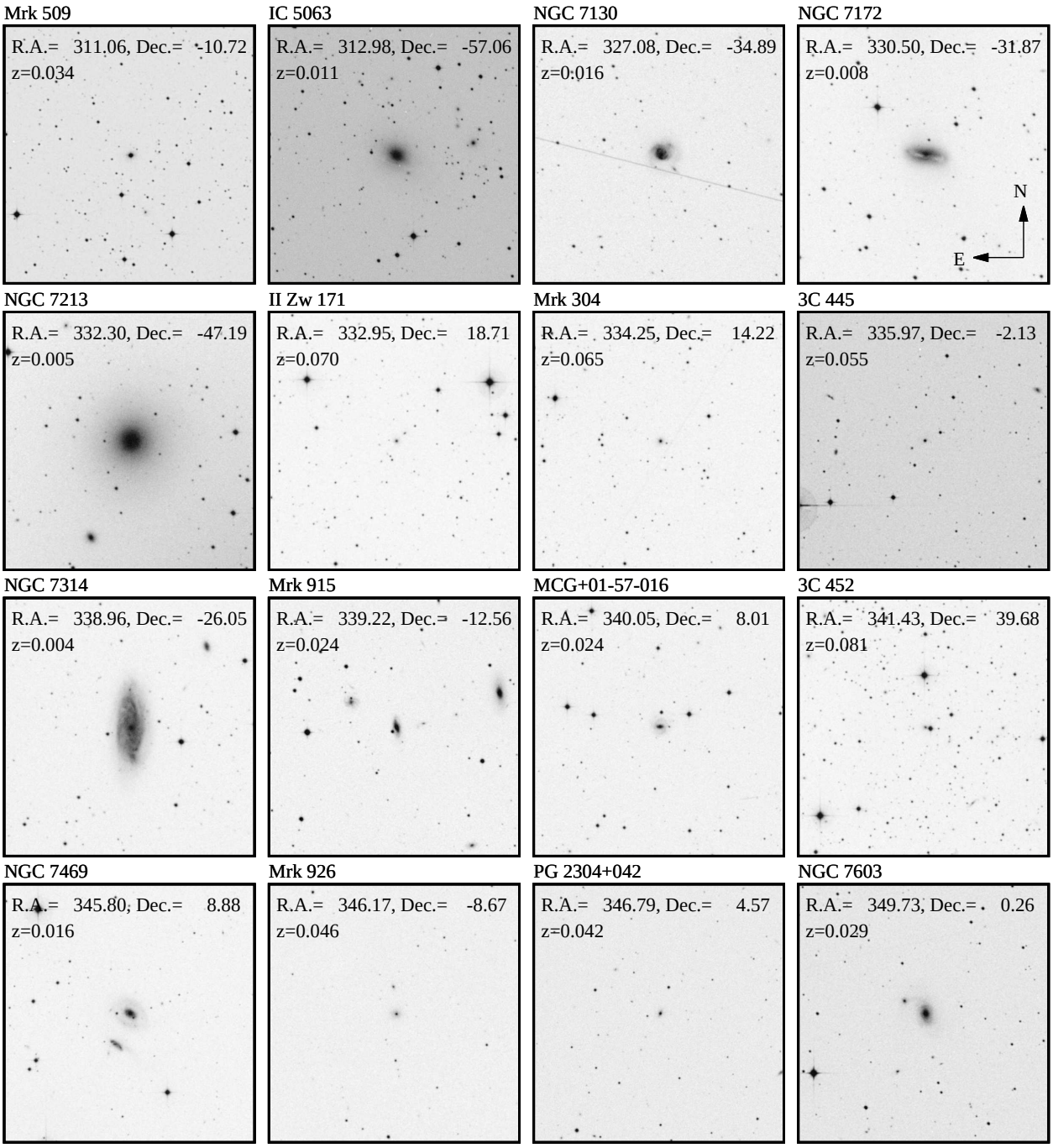

Figure 2.7: (Continued).

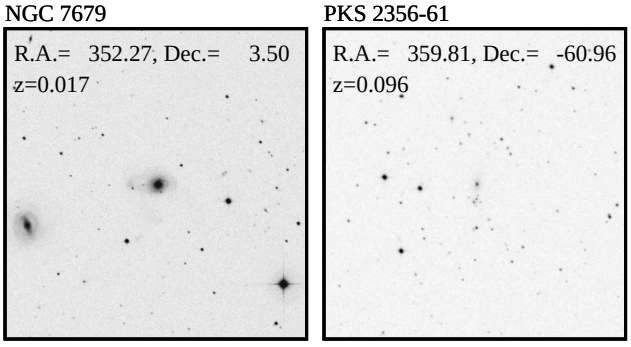

Figure 2.7: (Continued).

CHAPTER 3

OBSERVATIONS

3.1 The near-IR Camera Onboard the Akari Satellite

The 2.5–5 μm spectroscopic observations of the AGNs have been made with the Infra Red Camera IRC on board Akari. The Infrared Camera (IRC) was designed to make wide-field deep imaging and low-resolution spectroscopic observations in the pointing mode of the Akari satellite. It consists of three units (which are referred to as "channels"), one unit of Near Infrared camera (the near-IR-channel), which covers the 2–5 μm range, and two units of mid-IR cameras, the MIR-S and MIR-L channels (see Figure 3.1(*right*)) covering 5–12 μm and 12–26 μm respectively.

All the units can be operated in both imaging and spectroscopy modes. When the liquid helium boiled off in August 26, 2007, the Akari mission entered Phase 3 (the post-helium phase), when a mechanical cooler was able to keep the temperature low enough only for the IRC/NIR camera. The MIR cameras of the IRC (as well as the Far Infrared Surveyer, FIS) were turned off.

As a part of the AGNUL working group of the Akari team, we have made near-IR (2.5-5 μm) spectroscopic observations of a sample of bright hard X-ray selected AGNs during phase 3 using the Grism spectrometer attached to the near-IR channel (NG) of IRC. In our extended sample we included both public and property observations a as part of the AGNUL team observation proposal (P.I. T. Nakagawa) under the Akari MP3 (Mission Program Phase 3) program over two cycles, MP3-I (for observations from approximately April 2008 to September 2009) and MP3-II (after approximately October 2009). Due to the

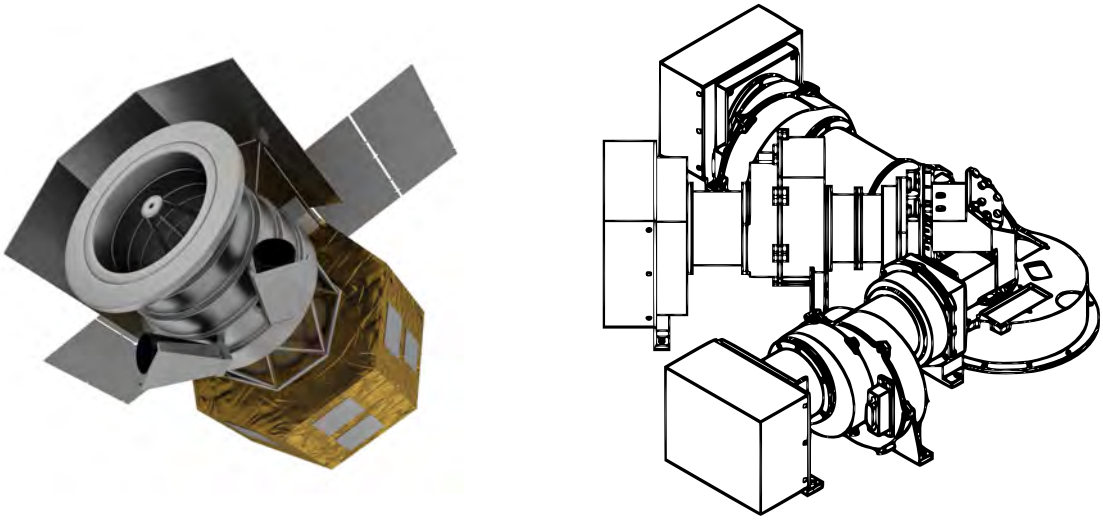

Figure 3.1: Overall views of (left) the Akari spacecraft, and the (right) IRC camera (Onaka et al., 2007) on board.

increased number of hot pixels during the Phase 3 period not all of the downloaded observations had quality enough to be included in the sample, and some objects had only one or two orbits of observations (as shown in column 'Observation ID' in Table 3.1).

Table 3.1: Akari/IRC observation log of hard X-ray selected AGNs.

Swift Name	Counterpart Name	Observation ID[a]	Observation Date	Early[b,d]	Ext.[c,d]
J0006.2+2012	Mrk 335	1340442-1,2,3	2008-06-30	×	◯
J0010.5+1057	Mrk 1501	1341139-2,3	2009-12-28	×	◯
J0048.8+3155	NGC 262 (Mrk 348)	1122156-1	2010-01-15	◯	◯
J0051.9+1724	Mrk 1148	1920037-1	2008-12-31	×	◯
J0123.9-5846	Fairall 9	1340445-1,3	2008-12-01,02	◯	◯
J0134.1-3625	NGC 612	1120076-1,2,4,5	2008-06-24,26	◯	◯
J0138.6-4001	ESO 297-018	1120074-1,2,3,4,5	2008-06-23	◯	◯
J0214.6-0049	Mrk 590	1340446-1,2	2009-07-24	◯	◯
J0238.2-5213	ESO 198-024	1122056-1,2,3,4,5	2009-12-25	◯	◯
J0433.0+0521	3C 120	1340447-1,2,3	2009-02-25	◯	◯
J0516.2-0009	Ark 120	1340448-1,2,3	2008-09-09	◯	◯
J0601.9-8636	ESO 005-G004	1120073-1,2,3,4,5	2008-09-19,20	◯	◯
J0615.8+7101	Mrk 3	1120001-1,2,3	2008-09-23	◯	◯
J0810.9+7602	PG 0804+761	1340449-1,2	2008-10-04	×	◯
J0902.0+6007	Mrk 18	1122043-1,2,3,4,5	2009-10-20	◯	◯
J0920.8-0805	MCG-01-24-012	1122045-1	2009-11-17	◯	◯
J0925.0+5218	Mrk 110	1340451-1,2,3	2009-04-25	◯	◯
J0945.6-1420	NGC 2992	3750049-1,2,3	2009-11-25,26	◯	◯
J0947.6-3057	MCG-05-23-016	1122050-1,2,3	2009-12-03,05	◯	◯
J0959.5-2248	NGC 3081	1120082-1,2,3,4,5	2009-06-02	◯	◯
J1031.7-3451	NGC 3281	1120075-1,2	2009-06-17	◯	◯
J1049.4+2258	Mrk 417	1120083-1,2	2009-05-26	◯	◯
J1139.0-3743	NGC 3783	1340453-1,2,3	2008-07-03	◯	◯
J1143.7+7942	UGC 06728	1122054-1,2,4,5	2009-10-15	◯	◯
J1203.0+4433	NGC 4051	1340473-1	2009-05-29	◯	◯
J1206.2+5243	NGC 4102	1120232-1,1122090-1	2009-05-25,2009-11-27	◯	◯
J1210.5+3924	NGC 4151	1122024-1,1340454-1,2,3	2008-06-03,2009-12-05	◯	◯
J1225.8+1240	NGC 4388	1120080-1,2,3	2009-06-21	◯	◯

Table 3.1(Continued.)

Swift Name	Counterpart Name	Observation ID[a]	Observation Date	Early[b,d]	Ext.[c,d]
J1232.1+2009	Mrk 771	1340456-1,2,3	2009-06-20	×	◯
J1238.9-2720	ESO 506-G027	1120078-1,2,3,1120079-1,2	2009-01-10,2009-07-11	◯	◯
J1239.6-0519	NGC 4593	1340475-1,2	2008-07-02,2009-01-01	◯	◯
J1303.8+5345	SBS 1301+540	1122053-1,2,3,4,5	2009-12-04,05	◯	◯
J1305.4-4928	NGC 4945	3180009-1	2007-01-27	◯	◯
J1322.2-1641	MCG-03-34-064	1120084-1,2,3,4,5	2008-07-17	◯	◯
J1338.2+0433	NGC 5252	1120085-1,2,3,4,5	2009-07-12,13	◯	◯
J1349.3-3018	IC 4329A	3750054-1,2,3	2010-01-26	◯	◯
J1352.8+6917	Mrk 279	1340458-1,2,3	2008-11-14,15,16	◯	◯
J1355.9+1822	Mrk 463	3750038-1,2,3	2010-01-09	×	◯
J1413.2-0312	NGC 5506	1120068,1,2	2008-07-24	◯	◯
J1417.9+2507	NGC 5548	1340460-1,2,3	2008-07-13,14	◯	◯
J1442.5-1715	NGC 5728	1120086-1,2,3	2009-08-05,06	◯	◯
J1504.2+1025	Mrk 841	1340548-1	2009-08-02	×	◯
J1535.9+5751	Mrk 290	1340550-1,2,3	2008-06-29,2009-01-01	◯	◯
J1652.9+0223	NGC 6240	3370014-1,2	2009-03-01	×	◯
J1842.0+7945	3C 390.3	1340466-1,2,3	2008-09-10	◯	◯
J2028.5+2543	MCG+04-48-002	1120077-1,2,1122037-1,2	2009-05-09,2009-11-09	◯	◯
J2044.2-1045	Mrk 509	1340467-1,2,3	2009-04-30	◯	◯
J2052.0-5704	IC 5063	1122041-3,4,5	2009-10-20,21	◯	◯
J2148.3-3454	NGC 7130	1120236-1,2,3	2008-11-08,09,10	×	◯
J2201.9-3152	NGC 7172	1122046-1,2,3	2009-11-13,14	◯	◯
J2209.4-4711	NGC 7213	1120069-1,2,3	2008-11-08	◯	◯
J2211.7+1843	II Zw 171	1341174-1,2	2009-12-03,05	×	◯
J2217.0+1413	Mrk 304	1920263-1,2	2009-06-01,02	×	◯
J2223.9-0207	3C 445	1920265-1,2	2009-05-27,28	×	◯
J2303.3+0852	NGC 7469	1120055-1,3	2008-06-10	◯	◯
J2318.9+0013	NGC 7603	3750045-1	2009-12-12	×	◯
J2328.9+0328	NGC 7679	1122290-1,2	2009-12-15	×	◯

Table 3.1(Continued.)

Swift Name	Counterpart Name	Observation ID[a]	Observation Date	Early[b,d]	Ext.[c,d]
J0319.7+4132	NGC 1275	1120056-1	2009-08-21	◯	×
J0426.2-5711	1H 0419-577	1920103-1,2	2009-01-16	◯	×
J0519.5-3140	ESO 362-G021	1920114-1,2	2009-03-04	◯	×
J0554.8+4625	MCG+08-11-011	1120063-1,2,3	2009-09-21	◯	×
J0623.9-6058	ESO 121-G028	1122044-1,2,3,5	2009-10-18,24	◯	×
J0651.9+7426	Mrk 6	1120064-1,2,3	2008-09-27	◯	×
J0742.5+4948	Mrk 79	1340470-1,2,3	2008-10-10	◯	×
J1106.5+7234	NGC 3516	1122032-1,2,3,4	2009-10-25	◯	×
J1628.1+5145	Mrk 1498	1920237-1	2009-07-31	◯	×
J1959.4+4044	Cygnus A	1420108-1	2009-05-09	◯	×
J2318.4-4223	NGC 7582	1122034-2,3,4	2009-11-23	◯	×

[a] Internal Object ID.

[b] Early sample: the 54 Akari/IRC observed sources from Castro et al. (2014).

[c] Extended sample: 130 Spitzer/IRS observed AGNs + 57 Akari/IRC observed AGNs (43 AGNs from Castro et al. (2014) and 14 new AGNs).

[d] If present in this sample the object is marked with the simbol '◯'.

3.2 Akari/IRC Spectroscopy and Data Reduction

3.2.1 Akari/IRC Spectroscopy

Infrared 2.5–5 μm spectroscopy of our hard X-ray selected AGNs was performed with the IRC spectrograph (Onaka et al., 2007, 2009) on board the Akari Infrared satellite (Murakami et al., 2007) during the Phase 3-mission program. The NIR channel of IRC has two dispersion spectroscopic elements, NP (low resolution prism) and NG (high resolution grism). The spectroscopic observations can be made with or without a slit. The spectra in the 2.5–5 μm band were taken with the high resolution grism (NG), acheiving a spectral resolution $R = \lambda/\delta\lambda = 120$ at $\lambda = 3.6$ μm (Ohyama et al., 2007) for point sources. Among the three

slit/window sizes available, the $1' \times 1'$ square window was used for all of our observations. This window size is optimized for the spectroscopy of the point sources, where the size was determined such that the aperture is larger than the absolute pointing accuracy of the satellite ($\leq 30''$). The Astronomical Observation template (AOT) of our observations was IRCZ4. More details about the spectroscopic exposures and observing mode can be found in Imanishi et al. (2010), Castro et al. (2014), and Ichikawa et al. (2014). All Akari/IRS raw spectra were downloaded using the search tool for the Akari pointing observation [1].

Following the method summarized in Section 3.2.3, we apply the adopted extinction law and the relation A_λ/A_{K_S} (Román-Zúñiga et al., 2007; Nishiyama et al., 2009) in order to do the flux correction considering the proper line-of-sight Galactic extinctions to the studied AGNs across the 2.5–5 μm range. For ilustrative purposes, in Figure 3.2 are shown 3 Akari/IRC 2.5–5 μm spectra. Figure 3.7 show the principal emission and absorbing lines in the near-IR band. For details about the complete hard X-ray selected Akari/IRC sample see Castro et al. (2014).

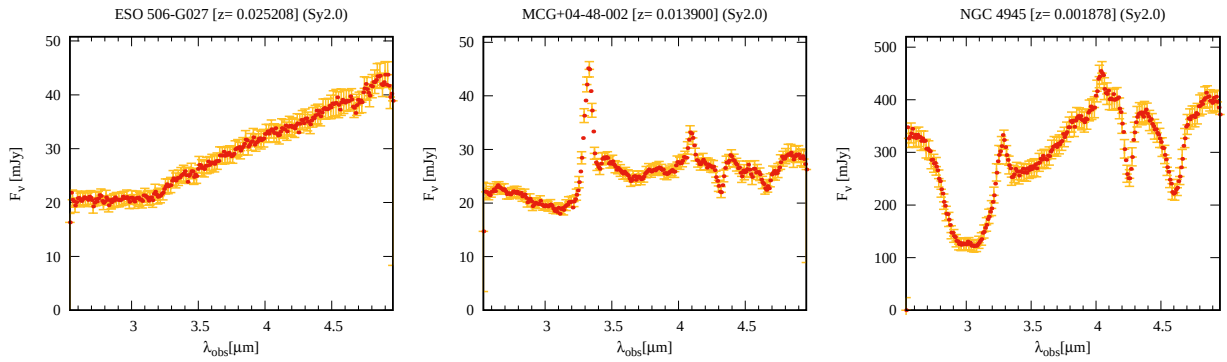

Figure 3.2: Single plots were generated for every reduced Akari/IRC low-resolution spectra. Here we show three randomly selected spectra. These spectra are plotted against the observed wavelength.

3.2.2 Akari/IRC Data Reduction

The spectra have been reduced using the IDL package, "IRC Spectroscopy Toolkit for Phase 3 data Version 20110301" (Ohyama et al., 2007) [2] (hereafter referred to as "the toolkit"). The toolkit performs the basic reduction pipeline of linearity correction, background and dark subtraction and the division by flat frames of

[1] http://www.darts.isas.ac.jp/astro/akari/akarilog/top.do
[2] http://www.ir.isas.jaxa.jp/ASTRO-F/Observation/

the two-dimensional (2D) spectra (Onaka et al., 2009). During the pipeline processing, the toolkit removes the hot and bad pixels upon coadding individual images and/or upon correcting the image by its own dark image. For the NG grism, the 2D spectra corresponds to $d\lambda = 0.0097$ μm/pix along the dispersion and the $1''.46$/pix perpendicular to it (Ohyama et al., 2007). We adopted a narrow aperture of 3 pixels (`nsum=3`; $4''.38$), corresponding to the typical full-width of the image PSF for achieving the best S/N in creating the 1-dimensional (1D) spectra. For some cases small shifts of the aperture position on the sky were required. The 1D spectra from different orbits of an object have been averaged to obtain the final spectrum.

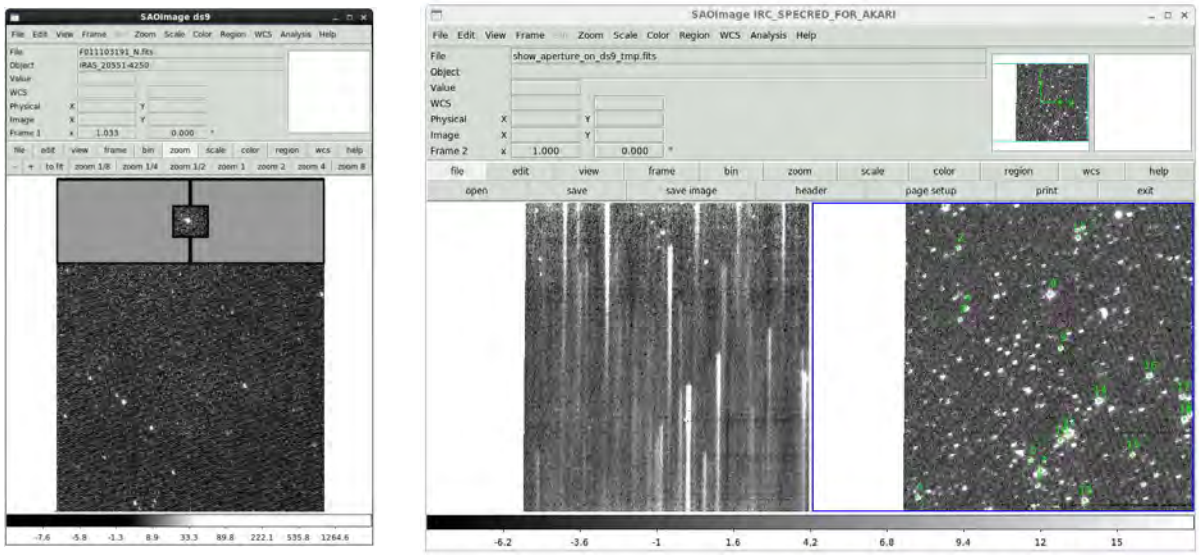

Figure 3.3: Data reduction interface for the Akari/IRC instrument. The toolkit run IDL, IRAF and the visual SAO DS9 interface. The middle 1'$\times$1' square part, referred to as 'Np' is for spectroscopy of point sources.

The IRCZ4 data reduction pipeline rotates of the NIR (the NIR-channel) images at the first step. After the NIR rotation, the dispersion directions are the same for all the dispersers in spectroscopy images. The IRC imaging data reduction toolkit is developed to address and correct any IRC instrument features, such as linearity, flat fielding, dark subtraction, background subtraction, image stacking, distortion, wavelength calibration, etc., and converts the raw ADU signal to physically meaningful units (i.e. flux). (Onaka et al., 2009).

The toolkit runs on IRAF and consists of three main steps: pre-pipeline, pipeline, and post-pipeline. Some basic tasks are performed during the pre-pipeline step such as the header formatting, slicing of IRC 3D images into usual 2D ones, and the creation of the observing log files. Basic science data is produced in the pipeline step where the toolkit performs some impoertant task like: normalization (to all the frames), linearity correction, dark subtraction, scattered light pattern subtraction, cosmic ray rejection, and flat fielding. During the post-pipeline process a mask is applyied in order to remove bad/dead/hot pixels, aspect ratio is corrected (for all the frames), individual frames are co-added and flux calibrated.

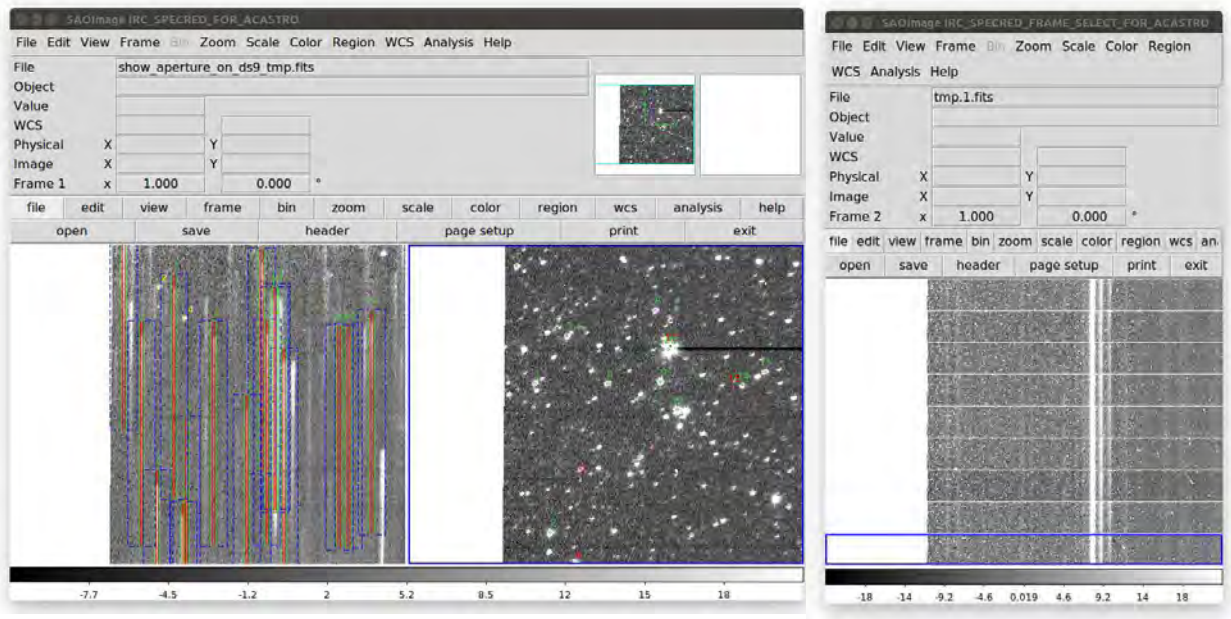

Figure 3.4: IRC extraction of bright reference sources. Once object frames have been correctly matched and the sky brightness adjusted, they are stacked to produce the final co-added image.

Particularly, the coadding processor is resposible of performing the following tasks: extract bright reference sources (see Figure 3.4), calculate shift and rotation to match frames (lists of the bright sources are used to calculate the relative shift and rotation values between individual frames), adjust sky level (each calculated image median value is subtracted from each corresponding frame), image stacking (co-adding), and finally, after the co-add wrapper has been completed, this module updates WCS information to the

stacked FITS images by matching with 2MASS or WISE catalog (Egusa et al., 2016). The pipeline can be run automatically or interactively step by step.

The calibration uncertainties of Akari/IRC spectra become large when $\lambda_{\rm obs} > 4.8$ μm. We arbitrarily excluded the $\lambda_{\rm obs} < 2.55$ μm and $\lambda_{\rm obs} > 4.85$ μm edges in order to avoid bad S/N data. The resultant Akari/IRC near-IR spectra, in the observed-frame wavelength, $\lambda_{\rm obs} = \lambda_{\rm rest} \times (1 + z)$, after Galactic extinction correction (see Section 3.2.3) are shown in the left panels of Figure 3.10.

The aperture size corresponds to ~ 2 kpc at the distance of ~ 100 Mpc and thus our spectra are collected from regions weighted towards the central bulge-sized region around the nucleus and the contributions of disks are relatively suppressed.

3.2.3 Near-IR Correction for Galactic Extinction

Before proceeding further, we have corrected our 2.5–5 μm spectra for Galactic extinctions as follows. Galactic extinctions in the K-band at 2.2 μm (A_K) were taken from the NED ExtraGalactic Catalog. Extinction values agree with Schlegel et al. (1998) infrared-based dust map from the COBE/DIRBE and IRAS/ISSA which assumes a Cardelli et al. (1989) extinction law. Nishiyama et al. (2006) determined the ratios of total to selective extinction in the IRSF/SIRIUS near-infrared (J,H,K_S) and established that the extinction in the 2-3 μm wavelength range is well fitted by a power-law with a steep decrease $A_\lambda \propto \lambda^{-2}$ toward the Galactic centre. We have made a small correction from A_K to A_{K_S} ($\lambda_{\rm eff} = 2.14$ μm) using this relation. Then, we apply the adopted extinction law and the relation A_λ/A_{K_S} (Nishiyama et al., 2009; Román-Zúñiga et al., 2007) in order to do the flux correction considering the proper line-of-sight Galactic extinctions to the studied AGNs across the whole 2.5–5 μm range (see Figure 3.5). As can be observed in Figure 3.6 extinction in the near- and mid-IR bands is negligible for practical purposes. We included this correction for more precise results.

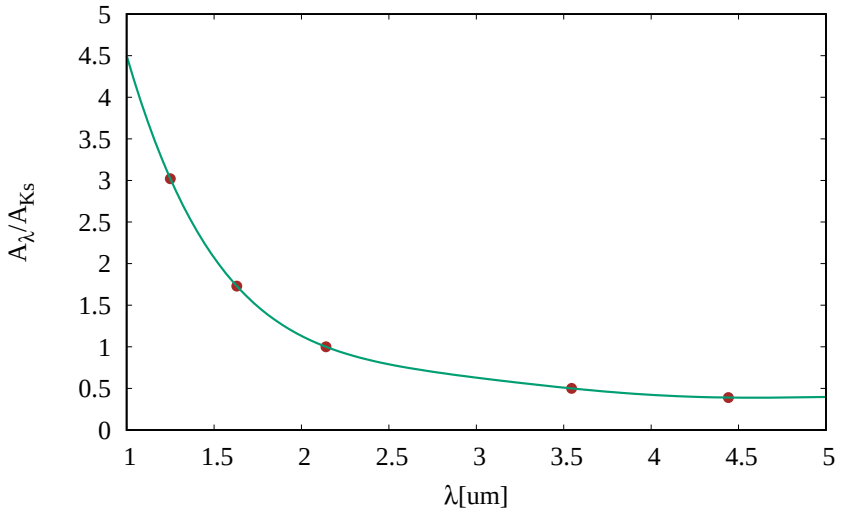

Figure 3.5: Adopted extinction curve in the 2.5-5 μm band. A polynomial regression was performed based on Nishiyama et al. (2006) extinction measurement data points in the near-IR band.

3.3 Spitzer/IRS spectroscopy

The InfraRed Spectrograph (IRS; see Figure 3.8/right) provided spectroscopic capabilities to the Spitzer Space Telescope. The IRS has four modules which provided low-resolution spectroscopy: Short-Low (SL; 5.2–14.5 μm at 60 $<$ R $<$ 128), Long-Low (LL; 14.0–38.0 μm at 57 $<$ R $<$ 126), Short-High (SH; 14.0–38.0 μm at 57 $<$ R $<$ 126), and Long-High (LH; 9.9–19.6 μm at R 600). Spectroscopy could be obtained in either Staring Mode or Mapping Mode. Further details can be consulted at the IRS Instrument Handbook [3].

Spitzer/IRS spectra were acquired using the staring-mode spectroscopy, the basic operating mode of the IRS. In this mode, sources were placed on the IRS slit during a specific integration time. We downloaded fully-calibrated fully-processed data from the NASA/IPAC Infrared Science Archive[4] enhanced products. The enhanced products are integrated by two elements: 1) a collection of low-resolution merged spectra presented in an ASCII format containing a detailed header, and 2) a catalog of source positions and other parameters. From the 4 low-resolution slits (SL2, SL1, LL2, LL1), for the purpose of the present study we

[3] http://irsa.ipac.caltech.edu/data/SPITZER/docs/irs/irsinstrumenthandbook/
[4] http://irsa.ipac.caltech.edu/frontpage/

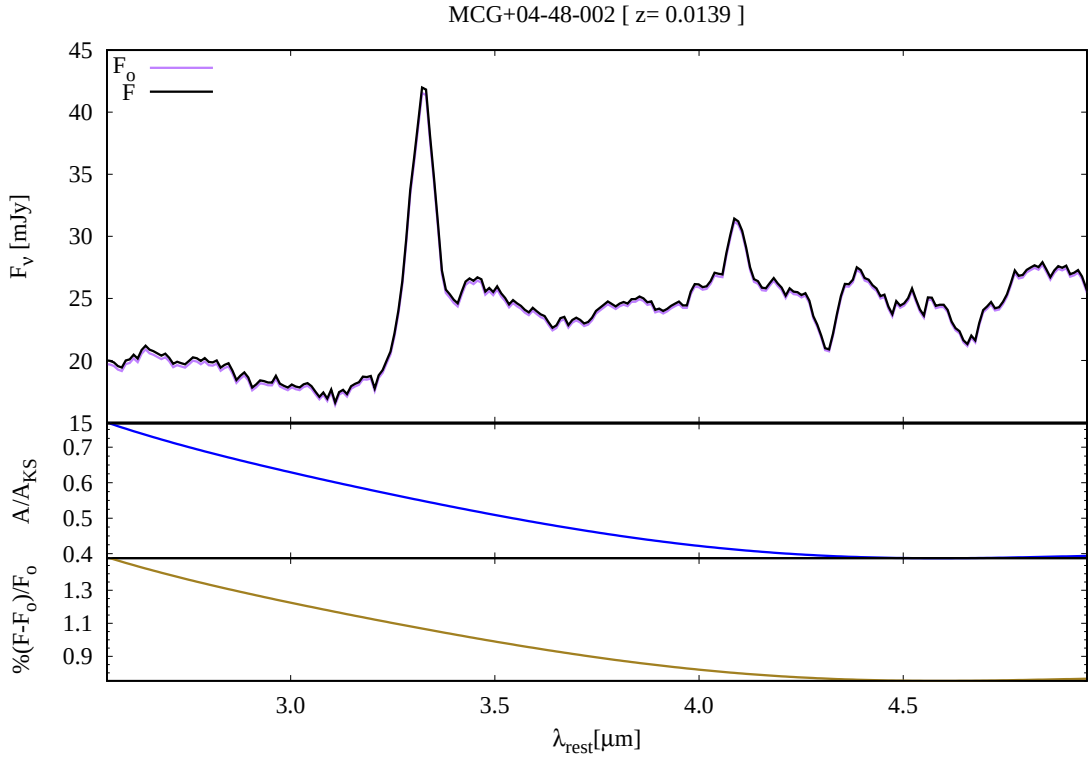

Figure 3.6: Galactic extinction in the 2.5-5 μm band. However, extinction is only about 1% in the bluer side of the waverange and negligible at the red wing of the observed IRC band. In this example is shown the Akari/IRS spectra of MCG+04-48-002, one of the objects with more extinction in our sample. It is shown in purple the observed flux while the flux corrected by Galactic extinction is shown in black. In the middle panel is shown the A/A_{Ks} extinction ratio. In the lower panel it is shown the error porcentage between the corrected and the observed flux $(F-F_o)/F_o$.

only used the SL2 and SL1 (order 1 and order 2, respectively) data resulting in a resultant spectra spanning in the 5.21–14.28 microns band. The SL slit width is 3.7 arcsec. The width of each slit is constant to 1% over its length.

A total of 130 AGNs from the Swift/BAT 70-month catalog were observed with Spitzer/IRS using the short-low (SL) spectral resolution (R $\sim$ 60–127) module. Table 3.2 summarizes the mid-IR observations. The Spitzer/IRS mid-IR spectra, in the observed-frame wavelength, are shown in the right panels of Figure 3.10.

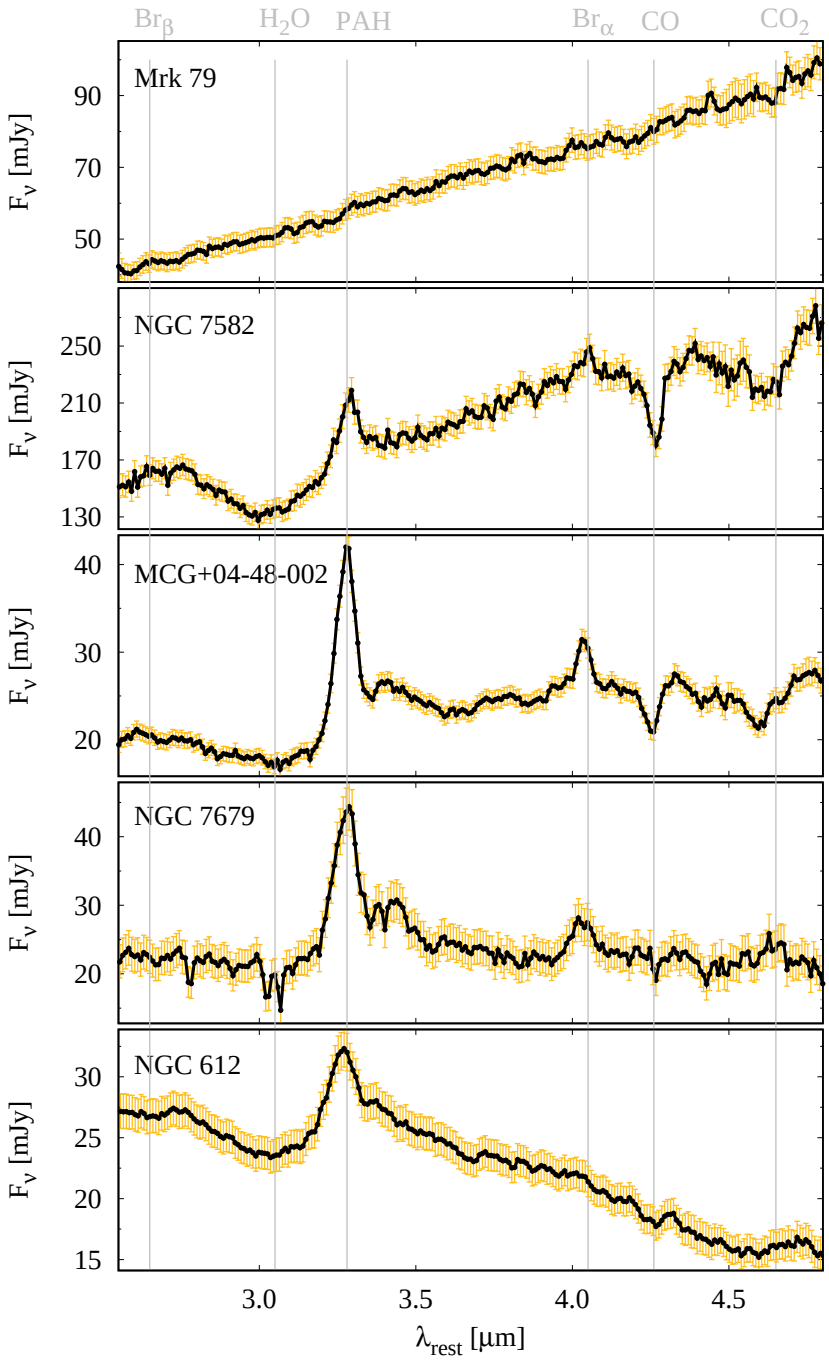

Figure 3.7: Example of a selection of low-resolution Akari/IRC spectra. No particular selection criteria was applied for the shown sources. Some of the most importat emission lines (2.6 μm Br$_\beta$, 3.28 μm PAH and 4.05 μm Br$_\alpha$) and absorption (3.1 μm H$_2$O, 4.26 μm CO and 4.65 μm CO$_2$) the 2.5–5 μm band can be ovserved. See Table 3.3

Table 3.2: Spitzer/IRS and AKARI/IRC observation log for hard X-ray selected AGNs.

No.	Swift/BAT ID	Dec*	R.A.*	Counterpart Name†	Redshift	Type	L_X	A††
1	SWIFT J0006.2+2012	1.580	20.178	Mrk 335	0.025785	1.2	43.45	◯
2	SWIFT J0010.5+1057	2.612	10.953	Mrk 1501	0.089338	1.2	44.80	◯
3	SWIFT J0048.8+3155	12.217	31.961	Mrk 348	0.015034	2.0	43.90	◯
4	SWIFT J0051.9+1724	12.965	17.425	Mrk 1148	0.064000	1.0	44.47	◯
5	SWIFT J0123.8-3504	20.944	-35.071	NGC 526A	0.019097	1.5	43.72	×
6	SWIFT J0123.9-5846	20.947	-58.785	Fairall 9	0.047016	1.2	44.41	◯
7	SWIFT J0134.1-3625	23.481	-36.504	NGC 612	0.029771	2.0	44.05	◯
8	SWIFT J0138.6-4001	24.659	-39.991	ESO 297-018	0.025200	2.0	44.00	◯
9	SWIFT J0201.0-0648	30.262	-6.806	NGC 788	0.013603	2.0	43.52	×
10	SWIFT J0206.2-0019	31.554	-0.279	Mrk 1018	0.042436	1.5	44.14	×
11	SWIFT J0214.6-0049	33.657	-0.777	Mrk 590	0.026385	1.2	43.42	◯
12	SWIFT J0231.6-3645	37.915	-36.666	IC 1816	0.016945	1.8	43.10	×
13	SWIFT J0234.1+3233	38.598	32.498	NGC 973	0.016195	2.0	43.27	×
14	SWIFT J0238.2-5213	39.576	-52.225	ESO 198-024	0.045500	1.0	44.16	◯
15	SWIFT J0241.3-0816	40.275	-8.257	NGC 1052	0.005037	2.0	42.22	×
16	SWIFT J0256.4-3212	44.091	-32.158	ESO 417-G006	0.016291	2.0	43.26	×
17	SWIFT J0333.6-3607	53.405	-36.149	NGC 1365	0.005457	1.8	42.63	×
18	SWIFT J0342.0-2115	55.513	-21.227	ESO 548-G081	0.014480	1.0	43.32	×
19	SWIFT J0402.4-1807	60.609	-18.087	ESO 549-G049	0.026291	2.0	43.60	×
20	SWIFT J0422.7-5611	65.622	-56.202	ESO 157-23	0.043530	2.0	43.97	×
21	SWIFT J0433.0+0521	68.292	5.339	3C 120	0.033010	1.0	44.38	◯
22	SWIFT J0438.2-1048	69.553	-10.793	MCG-02-12-050	0.036352	1.2	43.76	×
23	SWIFT J0451.4-0346	72.881	-3.844	MCG-01-13-025	0.015894	1.2	43.25	×
24	SWIFT J0453.4+0404	73.354	4.073	CGCG 420-015	0.029390	2.0	43.75	×
25	SWIFT J0508.1+1727	77.090	17.412	CGCG 468-002	0.018193	2.0	43.25	×
26	SWIFT J0516.2-0009	79.049	-0.138	Ark 120	0.032713	1.0	44.23	◯
27	SWIFT J0519.5-4545	79.922	-45.777	Pictor A	0.035058	1.0	44.04	×
28	SWIFT J0524.1-1210	81.031	-12.189	IRAS 05218-1212	0.049000	1.0	44.02	×

Table 3.2(Continued.)

No.	Swift/BAT ID	Dec*	R.A.*	Counterpart Name†	Redshift	Type	L_X	A††
29	SWIFT J0552.2-0727	88.039	-7.434	NGC 2110	0.007789	2.0	43.63	×
30	SWIFT J0601.9-8636	91.570	-86.626	ESO 005-G004	0.006384	2.0	42.46	◯
31	SWIFT J0615.8+7101	93.836	71.037	Mrk 3	0.013509	2.0	43.76	◯
32	SWIFT J0623.8-3215	95.938	-32.193	ESO 426-G002	0.022429	2.0	43.44	×
33	SWIFT J0623.9-6058	95.922	-60.956	ESO 121-G028	0.040521	2.0	44.03	×
34	SWIFT J0630.7+6342	97.663	63.708	UGC 03478	0.012769	1.2	42.57	×
35	SWIFT J0655.8+3957	103.926	39.975	UGC 03601	0.017122	1.5	43.15	×
36	SWIFT J0743.0+6513	115.759	65.209	Mrk 78	0.037150	2.0	43.54	×
37	SWIFT J0747.5+6057	116.854	60.912	Mrk 10	0.029255	1.2	43.46	×
38	SWIFT J0800.1+2638	120.086	26.633	IC 0486	0.026875	1.0	43.73	×
39	SWIFT J0804.2+0507	121.038	5.101	Mrk 1210	0.013496	2.0	43.35	×
40	SWIFT J0807.9+3859	121.971	38.988	Mrk 622	0.023229	2.0	43.07	×
41	SWIFT J0810.9+7602	122.726	76.032	PG 0804+761	0.100000	1.0	44.57	◯
42	SWIFT J0856.0+7812	134.003	78.194	NGC 2655	0.004670	2.0	41.81	×
43	SWIFT J0902.0+6007	135.621	60.107	Mrk 18	0.011088	2.0	42.53	◯
44	SWIFT J0919.2+5528	139.913	55.403	SBS 0915+556	0.049400	2.0	43.67	×
45	SWIFT J0920.8-0805	140.177	-8.064	MCG-01-24-012	0.019644	2.0	43.55	◯
46	SWIFT J0923.7+2255	140.947	22.925	MCG+04-22-042	0.032349	1.2	43.98	×
47	SWIFT J0925.0+5218	141.295	52.274	Mrk 110	0.035291	1.0	44.22	◯
48	SWIFT J0926.2+1244	141.526	12.769	Mrk 705	0.029150	1.2	43.49	×
49	SWIFT J0935.9+6120	143.983	61.335	MCG+10-14-025	0.039367	1.5	43.45	×
50	SWIFT J0945.6-1420	146.448	-14.302	NGC 2992	0.007710	2.0	42.55	◯
51	SWIFT J0947.6-3057	146.934	-30.938	MCG-05-23-016	0.008486	2.0	43.51	◯
52	SWIFT J0959.5-2248	149.858	-22.847	NGC 3081	0.007976	2.0	43.07	◯
53	SWIFT J1001.7+5543	150.503	55.651	NGC 3079	0.003723	2.0	42.00	×
54	SWIFT J1003.4-3726	150.812	-37.399	ESO 374-G044	0.028453	2.0	43.13	×
55	SWIFT J1023.5+1952	155.898	19.851	NGC 3227	0.003859	1.5	42.56	×
56	SWIFT J1031.7-3451	157.990	-34.863	NGC 3281	0.010674	2.0	43.34	◯
57	SWIFT J1048.4-2511	162.105	-25.180	NGC 3393	0.012509	2.0	42.96	×

Table 3.2(Continued.)

No.	Swift/BAT ID	Dec*	R.A.*	Counterpart Name†	Redshift	Type	L_X	A††
58	SWIFT J1049.4+2258	162.383	22.996	Mrk 417	0.032756	2.0	43.90	◯
59	SWIFT J1139.0-3743	174.761	-37.736	NGC 3783	0.009730	1.0	43.58	◯
60	SWIFT J1139.8+3157	174.945	31.948	NGC 3786	0.008933	1.8	42.50	×
61	SWIFT J1143.7+7942	176.174	79.680	UGC 06728	0.006518	1.2	42.41	◯
62	SWIFT J1152.1-1122	178.020	-11.391	PG 1149-110	0.049000	1.0	43.94	×
63	SWIFT J1203.0+4433	180.749	44.524	NGC 4051	0.002336	1.5	41.67	◯
64	SWIFT J1204.5+2019	181.125	20.306	Ark 347	0.022445	2.0	43.53	×
65	SWIFT J1204.9+3105	181.249	31.182	UGC 07064	0.024997	1.9	43.28	×
66	SWIFT J1206.2+5243	181.556	52.725	NGC 4102	0.002823	2.0	41.69	◯
67	SWIFT J1210.5+3924	182.674	39.417	NGC 4151	0.003319	1.5	43.12	◯
68	SWIFT J1218.5+2952	184.611	29.848	Mrk 766	0.012929	1.5	42.91	×
69	SWIFT J1223.7+0238	185.846	2.679	Mrk 50	0.023433	1.2	43.45	×
70	SWIFT J1225.8+1240	186.453	12.679	NGC 4388	0.008419	2.0	43.64	◯
71	SWIFT J1232.1+2009	187.999	20.159	Mrk 771	0.063010	1.0	44.11	◯
72	SWIFT J1235.6-3954	188.871	-39.891	NGC 4507	0.011801	1.0	43.77	×
73	SWIFT J1238.9-2720	189.734	-27.309	ESO 506-G027	0.025208	2.0	44.13	◯
74	SWIFT J1239.6-0519	189.922	-5.329	NGC 4593	0.009000	1.0	43.20	◯
75	SWIFT J1303.8+5345	195.994	53.796	SBS 1301+540	0.029900	1.0	43.83	◯
76	SWIFT J1304.3-0532	196.079	-5.529	NGC 4941	0.003696	2.0	41.79	×
77	SWIFT J1304.3-1022	196.083	-10.374	NGC 4939	0.010374	2.0	42.78	×
78	SWIFT J1305.4-4928	196.341	-49.472	NGC 4945	0.001878	2.0	42.35	◯
79	SWIFT J1306.4-4025A	196.663	-40.404	ESO 323-077	0.015014	1.2	43.22	×
80	SWIFT J1309.2+1139	197.283	11.617	NGC 4992	0.025137	2.0	43.89	×
81	SWIFT J1313.1-1108	198.300	-11.122	II SZ 010	0.034267	1.0	43.61	×
82	SWIFT J1322.2-1641	200.622	-16.748	MCG-03-34-064	0.016541	1.8	43.27	◯
83	SWIFT J1325.4-4301	201.381	-43.026	Cen A	0.001825	2.0	43.01	×
84	SWIFT J1338.2+0433	204.580	4.544	NGC 5252	0.022975	1.9	44.14	◯
85	SWIFT J1349.3-3018	207.323	-30.326	IC 4329A	0.016054	1.2	44.23	◯
86	SWIFT J1349.7+0209	207.445	2.099	UM 614	0.032700	1.0	43.60	×

Table 3.2(Continued.)

No.	Swift/BAT ID	Dec*	R.A.*	Counterpart Name†	Redshift	Type	L_X	A††
87	SWIFT J1352.8+6917	208.288	69.313	Mrk 279	0.030451	1.5	43.92	◯
88	SWIFT J1355.9+1822	208.984	18.371	Mrk 463	0.050355	1.0	43.82	◯
89	SWIFT J1413.2-0312	213.308	-3.236	NGC 5506	0.006181	1.9	43.31	◯
90	SWIFT J1417.9+2507	214.497	25.127	NGC 5548	0.017175	1.5	43.72	◯
91	SWIFT J1419.0-2639	214.839	-26.663	ESO 511-G030	0.022389	1.0	43.66	×
92	SWIFT J1429.2+0118	217.301	1.303	Mrk 1383	0.086570	1.0	44.52	×
93	SWIFT J1432.8-4412	218.193	-44.207	NGC 5643	0.003999	2.0	41.80	×
94	SWIFT J1433.9+0528	218.488	5.463	NGC 5674	0.024931	1.9	43.35	×
95	SWIFT J1442.5-1715	220.613	-17.270	NGC 5728	0.009353	2.0	43.23	◯
96	SWIFT J1457.8-4308	224.437	-43.140	IC 4518A	0.016261	2.0	43.22	×
97	SWIFT J1504.2+1025	226.017	10.427	Mrk 841	0.036422	1.0	44.04	◯
98	SWIFT J1508.8-0013	227.208	-0.221	Mrk 1393	0.054348	1.5	44.14	×
99	SWIFT J1515.0+4205	228.788	42.053	NGC 5899	0.008546	2.0	42.51	×
100	SWIFT J1535.9+5751	233.996	57.916	Mrk 290	0.029577	1.0	43.67	◯
101	SWIFT J1652.0-5915A	252.999	-59.252	ESO 138-G001	0.009140	2.0	42.56	×
102	SWIFT J1652.0-5915B	252.999	-59.252	NGC 6221	0.004999	1.0	42.05	×
103	SWIFT J1652.9+0223	253.267	2.407	NGC 6240	0.024480	2.0	43.99	◯
104	SWIFT J1717.1-6249	259.271	-62.813	NGC 6300	0.003699	2.0	42.48	×
105	SWIFT J1719.7+4900	259.850	48.959	Arp 102B	0.024167	1.0	43.38	×
106	SWIFT J1747.8+6837A	266.942	68.621	Mrk 507	0.055900	1.0	43.56	×
107	SWIFT J1835.0+3240	278.766	32.688	3C 382	0.057870	1.0	44.84	×
108	SWIFT J1838.4-6524	279.565	-65.435	ESO 103-035	0.013286	2.0	43.65	×
109	SWIFT J1842.0+7945	280.640	79.775	3C 390.3	0.056100	1.0	44.88	◯
110	SWIFT J1844.5-6221	281.158	-62.368	Fairall 51	0.014178	1.0	43.26	×
111	SWIFT J1921.1-5842	290.290	-58.707	ESO 141-G055	0.037109	1.2	44.21	×
112	SWIFT J2028.5+2543	307.134	25.753	MCG+04-48-002	0.013900	2.0	43.53	◯
113	SWIFT J2044.2-1045	311.061	-10.728	Mrk 509	0.034397	1.2	44.42	◯
114	SWIFT J2052.0-5704	312.980	-57.067	IC 5063	0.011348	2.0	43.32	◯
115	SWIFT J2148.3-3454	327.084	-34.897	NGC 7130	0.016151	2.0	42.98	◯

Table 3.2(Continued.)

No.	Swift/BAT ID	Dec*	R.A.*	Counterpart Name†	Redshift	Type	L_X	A††
116	SWIFT J2201.9-3152	330.500	-31.871	NGC 7172	0.008683	2.0	43.46	◯
117	SWIFT J2209.4-4711	332.302	-47.198	NGC 7213	0.005839	1.5	42.50	◯
118	SWIFT J2211.7+1843	332.955	18.717	II Zw 171	0.070000	1.0	44.31	◯
119	SWIFT J2217.0+1413	334.251	14.224	Mrk 304	0.065762	1.0	44.00	◯
120	SWIFT J2223.9-0207	335.973	-2.131	3C 445	0.055879	1.0	44.50	◯
121	SWIFT J2235.9-2602	338.964	-26.059	NGC 7314	0.004763	1.9	42.42	×
122	SWIFT J2236.7-1233	339.221	-12.568	Mrk 915	0.024109	1.0	43.61	×
123	SWIFT J2240.2+0801	340.057	8.017	MCG+01-57-016	0.024974	1.8	43.37	×
124	SWIFT J2246.0+3941	341.435	39.685	3C 452	0.081100	2.0	44.72	×
125	SWIFT J2303.3+0852	345.800	8.883	NGC 7469	0.016317	1.2	43.60	◯
126	SWIFT J2304.8-0843	346.172	-8.677	Mrk 926	0.046860	1.5	44.77	×
127	SWIFT J2307.1+0433	346.798	4.576	PG 2304+042	0.042000	1.0	43.79	×
128	SWIFT J2318.9+0013	349.737	0.268	NGC 7603	0.029524	1.5	44.00	◯
129	SWIFT J2328.9+0328	352.279	3.506	NGC 7679	0.017139	2.0	43.00	◯
130	SWIFT J2359.3-6058	359.813	-60.960	PKS 2356-61	0.096306	2.0	44.52	×

* Equatorial coordinates (J2000.0) taken from Baumgartner et al. (2013) as listed in the Swift-BAT 70-month all sky hard X-ray survey webpage [5].

† Counterpart names taken from Baumgartner et al. (2013).

†† AGNs with both Spitzer/IRS and Akari/IRC spectra available are marked with the simbol '◯'.

3.4 Other features in the near- and mid-IR band

In addition to the emission lines at 3.3, 6.2 and 11.3 μm associated with the emission of PAHs, other features in emission and absorption are observable in the 2.5–14 μm band (see Table 3.3). Figure 3.7 shows the main dust and gas emission/absorption lines visible with the Akari/IRC instrument. At 3.4 μm carbonaceous dust absorption and 3.1 μm H_2O ice absorption, whose profile is very broad, extending over at least λ_{rest} = 2.8–3.3 μm in the rest-frame (Smith et al., 1989), are present. The detection of strong ($\tau_{3.1} > 0.6$) 3.1 μm

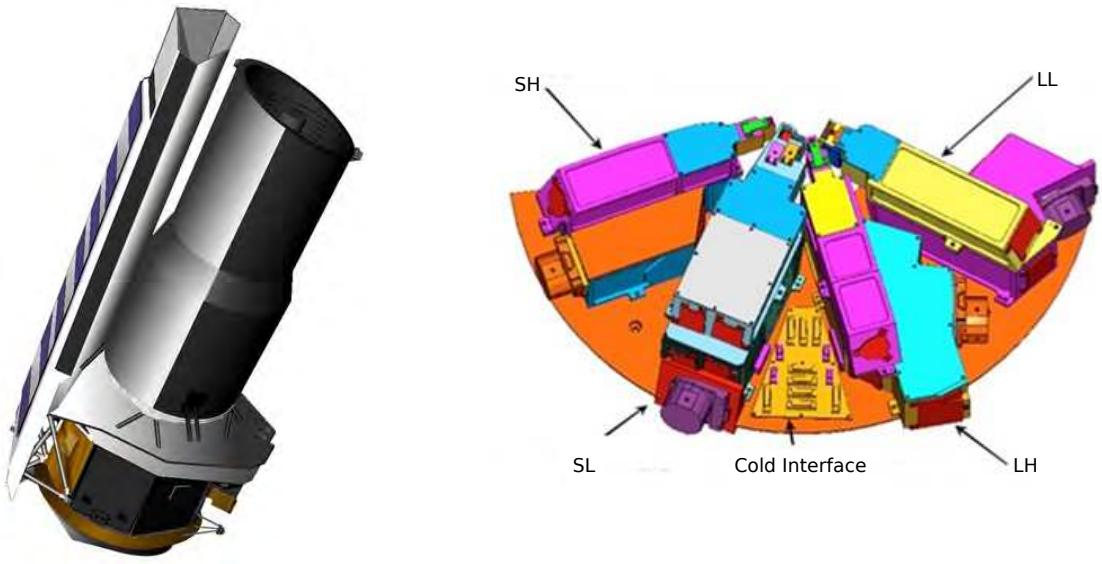

Figure 3.8: Artist view of the Spitzer infra-red space telescope (*left*) . We are including data obtained with the IRS (*right*) instrument on-board through the SL module (R $\sim$ 60–127) over 5.2–14.3 μm. Image takem from the IRS Intrument Handbook.

H_2O ice absorption can provide stringent constraints on the nature of the buried energy sources at the nuclei (Imanishi & Maloney, 2003)

The 3.4 μm carbonaceous and 9.7 μm silicate dust absorption features are detectable if an adequate amount of dust in the diffuse inter-stellar medium is present in front of the continuum-emitting energy sources (Imanishi & Maloney, 2003). The strength of these dust features are expected to be dependent on the specific geometry and optical depth of the torus (e.g. Fritz et al., 2006; Schartmann et al., 2008). Also, a weak correlation between gas column density (N_H) and silicate (Si) absorption strength has been observed from Spitzer mid-IR spectroscopy (e.g. Wu et al., 2009).

A detailed study of the the observed optical depths of the 3.1 μm H_2O absorption ($\tau_{3.1}$) as well as the 3.4 μm carbonaceous dust absorption ($\tau_{3.4}$) and 9.7 μm silicate absorption for our entire X-ray selecition of AGNs it is being prepared (Castro et al., in prep.). Another interesting emission line detected for a limited number of objects within our sample observed with Akari/IRC is the [MgIV] 4.48 μm intermediate-ionization line described in Spinoglio et al. (2005) and Tokunaga (1991), but poorly studied in the literature (see Figure 3.9).

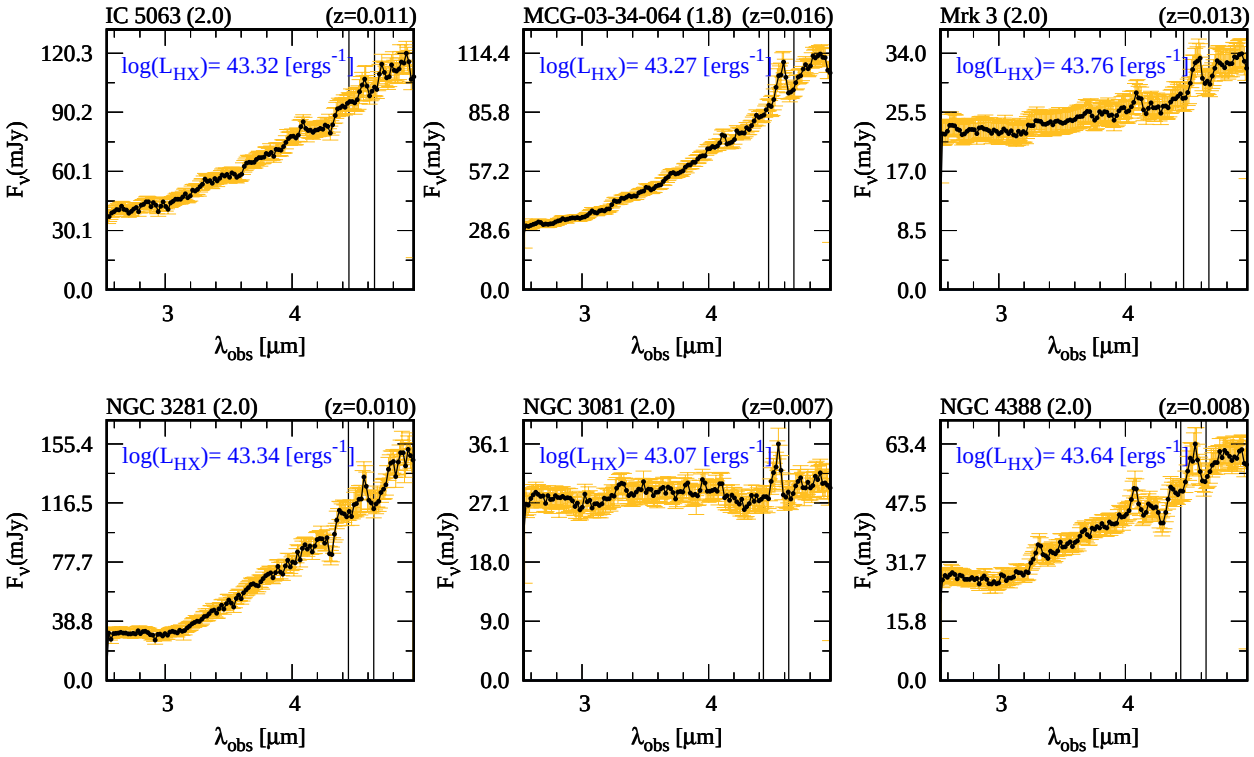

Figure 3.9: Candidates for [MgIV] detection in the Akari/IRC sample of our X-ray selecion of AGNs. It can be seen that all the sources are high X-ray luminosity Seyfert 2s.

Table 3.3: Prominent emission and absorption features detectable in the 2.5–14 μm IR band

Emission line				PAH	Dust absorption	
Feature	$\lambda(\mu m)$	Feature	$\lambda(\mu m)$	$\lambda(\mu m)$	Feature	$\lambda(\mu m)$
Brβ	2.63	H2 S(4)	8.02	3.3	H_2O	3.1
Brα	4.05	[Ar III]	8.99	6.2	CO_2	4.3
[MgIV]	4.48	H2 S(3)	9.66	7.7	XCN	4.6
H2 S(7)	5.51	[S IV]	10.51	8.6	CO	4.7
H2 S(6)	6.10	H2 S(2)	12.27	11.3	Si	9.7
H2 S(5)	6.90	[Ne II]	12.81	12.6		
[Ar II]	6.98					

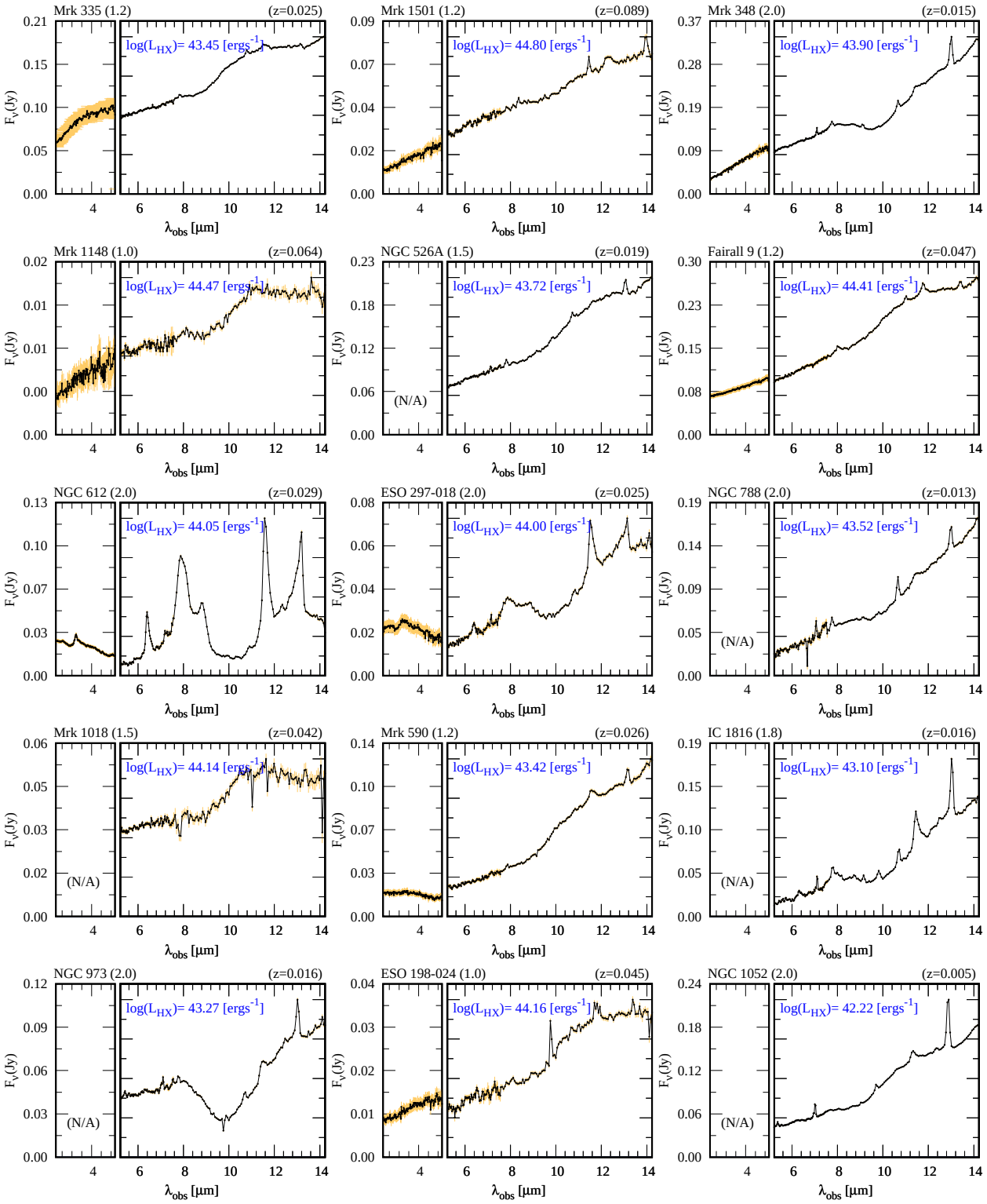

Figure 3.10: Mosaic of our whole X-ray selected AGN sample showing infrared 2.5–5 μm Akari/IRC (left panel), when available, and 5–14 Spitzer/IRS spectra (right panel). The abscissa is the wavelength ($\lambda_{\rm rest}$) and the ordinate is the flux F_ν in Jy. It is shown the AGNs name, redshift, and X-ray luminosity ($L_{14-195{\rm keV}}$; in units of $\rm erg\,s^{-1}$).

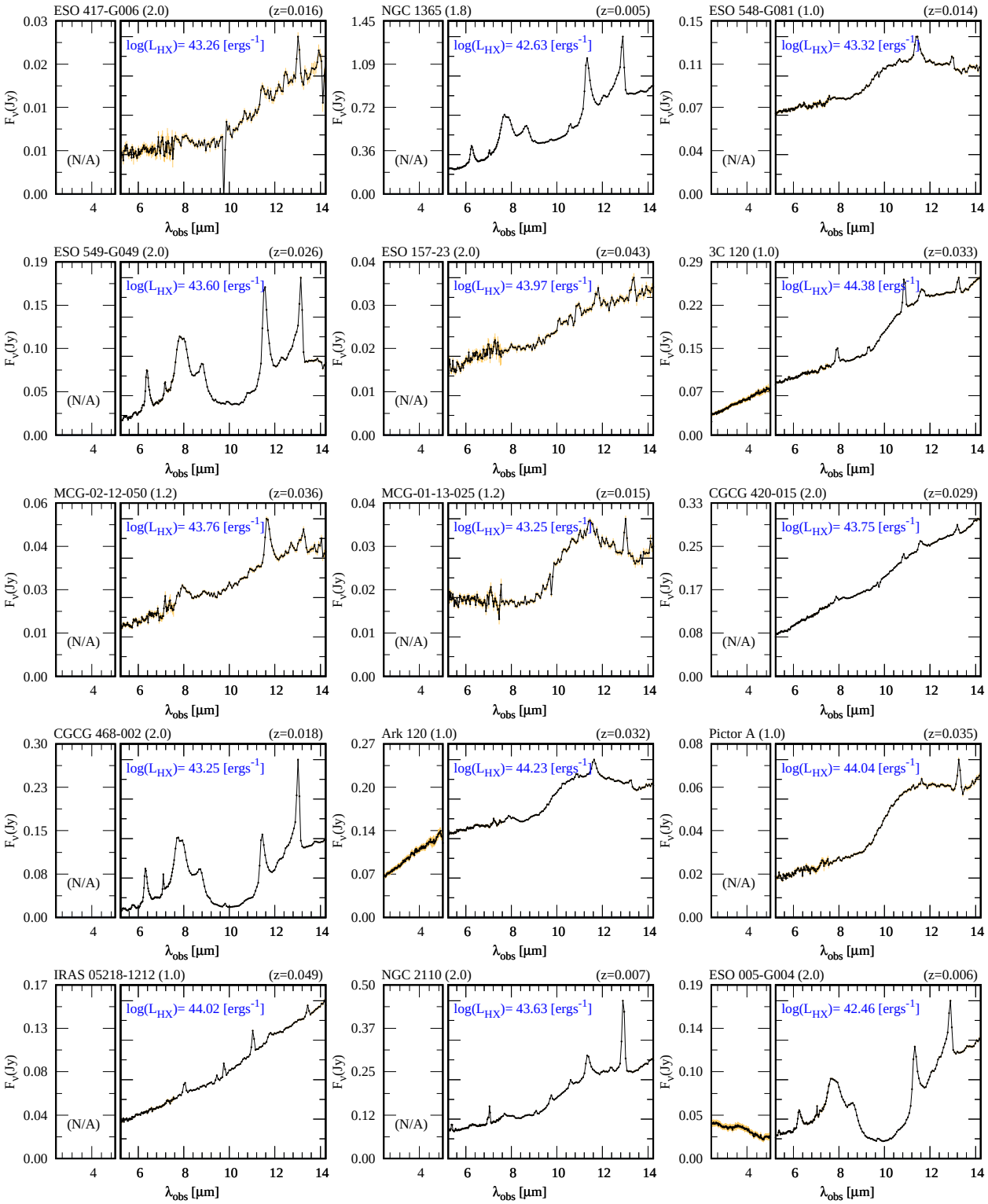

Figure 3.10: (Continued) Some objects show some miscalibration on the first order (SL1) subslit in the left-wing of the IRS band (e.g. NGC 3281, Mrk 771, IC 4329A, 3C 382, and ESO 103-035).

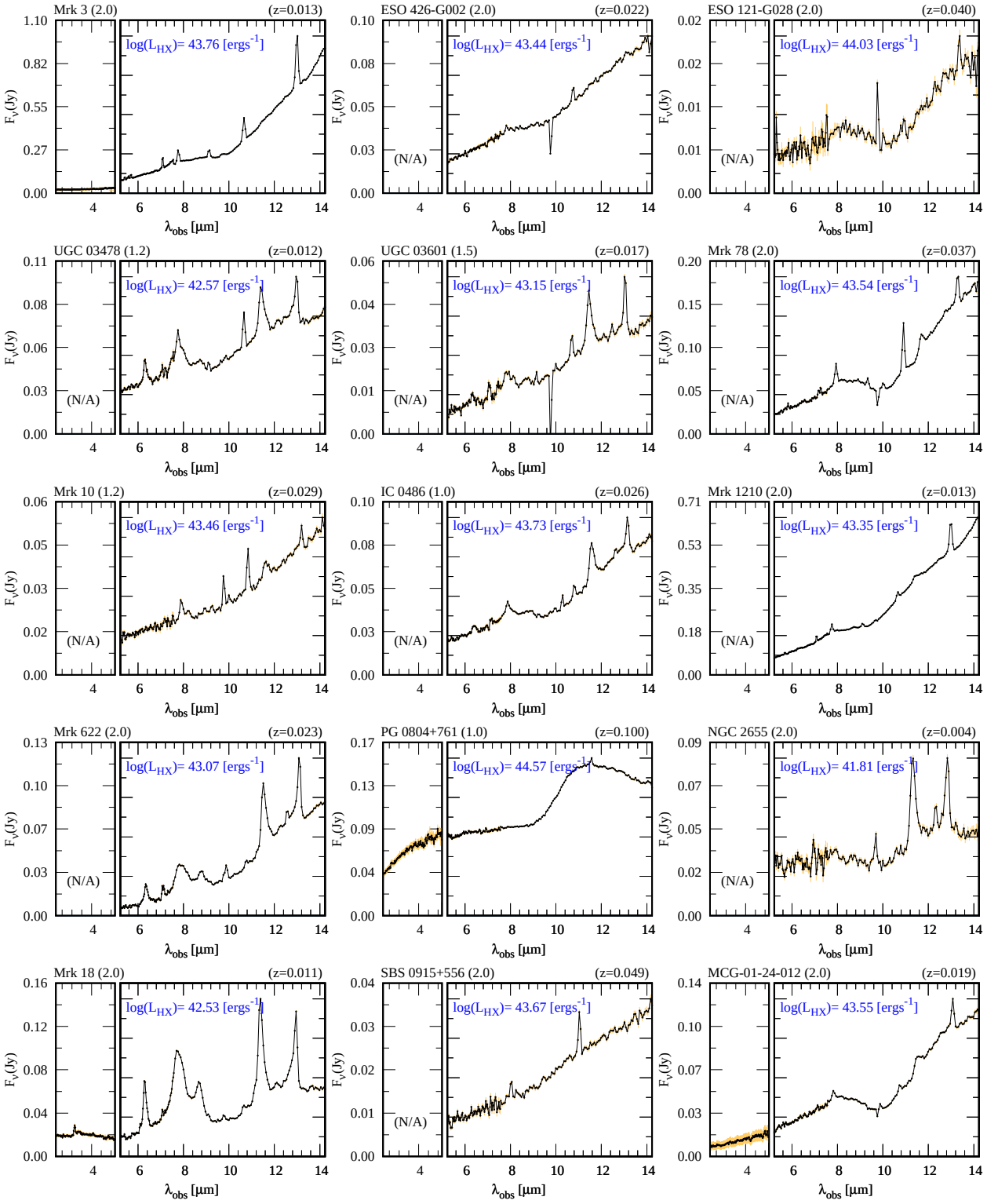

Figure 3.10: (Continued) ESO 426-G002, ESO 417-G006, ESO 198-024 and UGC 03601 show a $\sim$ 9.5 μm narrow absorption feature that seems to be artificial. We have to develope a spike-removing routine for future analysis.

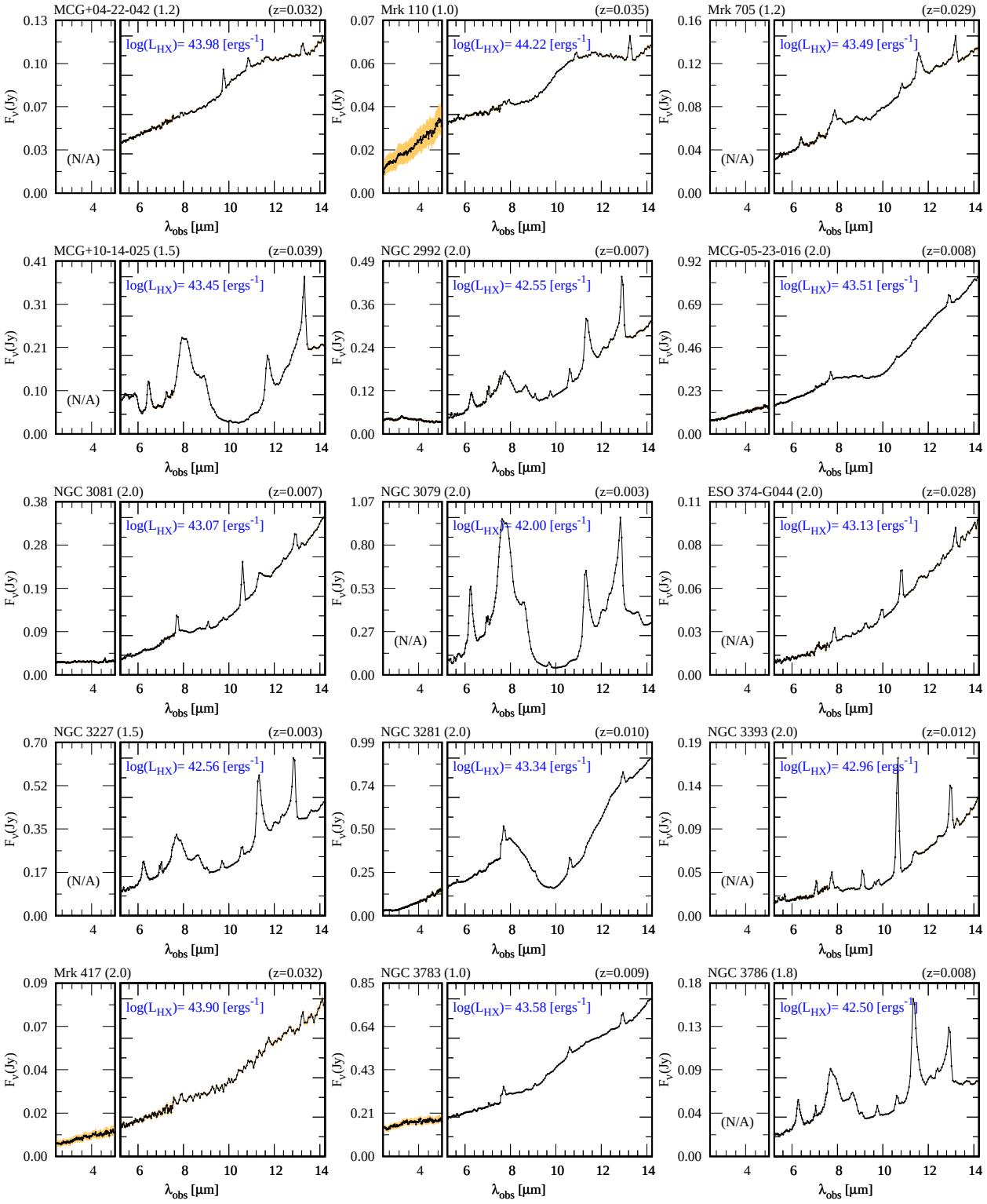

Figure 3.10: (Continued) Some spectra show significant continuum flux misalignment (e.g. SBS 1301+540, NGC 5252, IC 4329A, 3C 390.3, NGC 7172, and II Zw 171) between the Akari/IRC and Spitzer/IRS observations. Considering the apertures of the different slits employed this difference needs to be studied in detail.

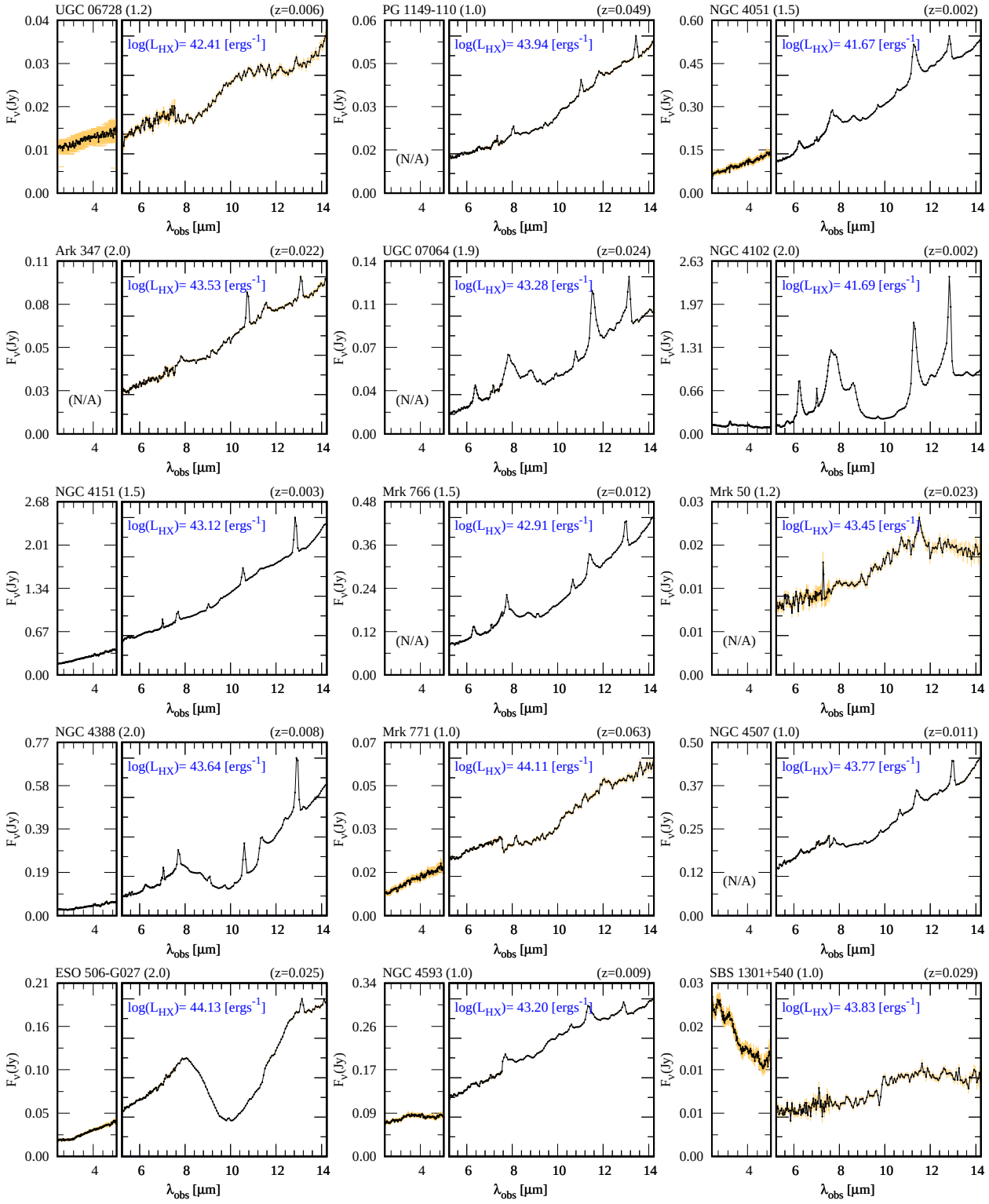

Figure 3.10: (Continued) SBS 1301+540 Akari/IRC spectra need to be cerefully repeated. Posible strong SB component or stellar contamination is present. WISE and IRAC photometry could confirm the significant change on the slope between the near- and mid-IR spectra.

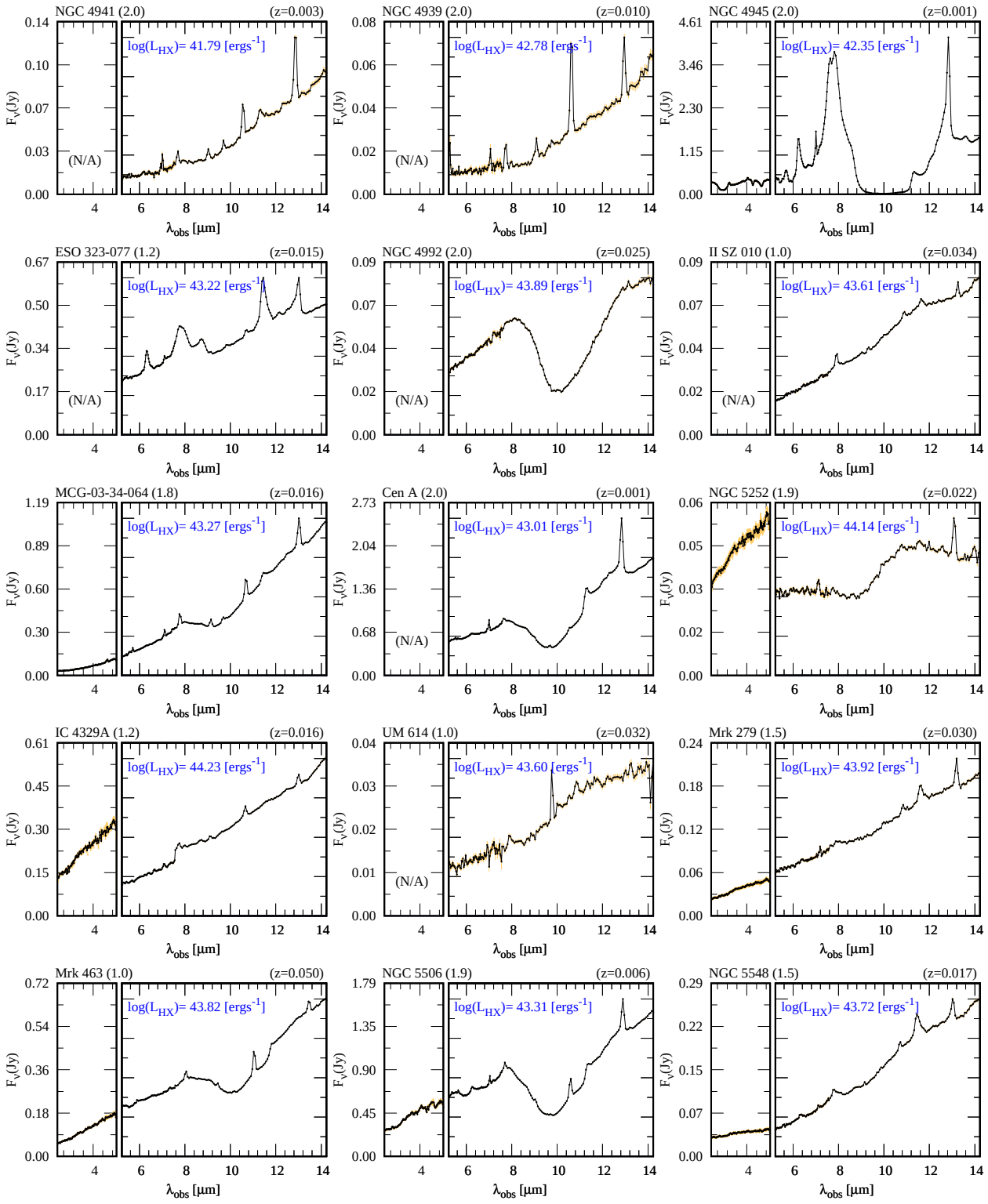

Figure 3.10: (Continued)

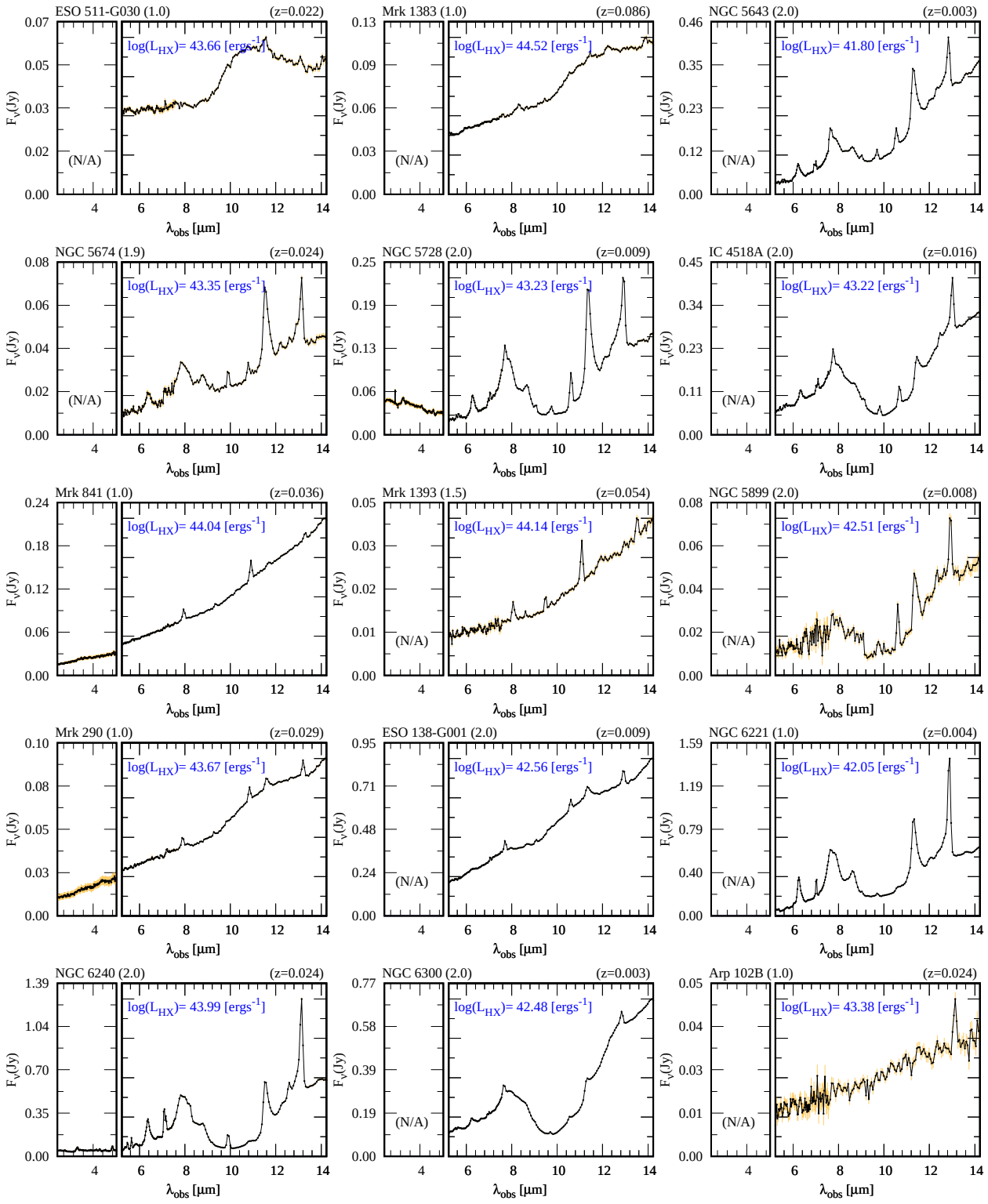

Figure 3.10: (Continued)

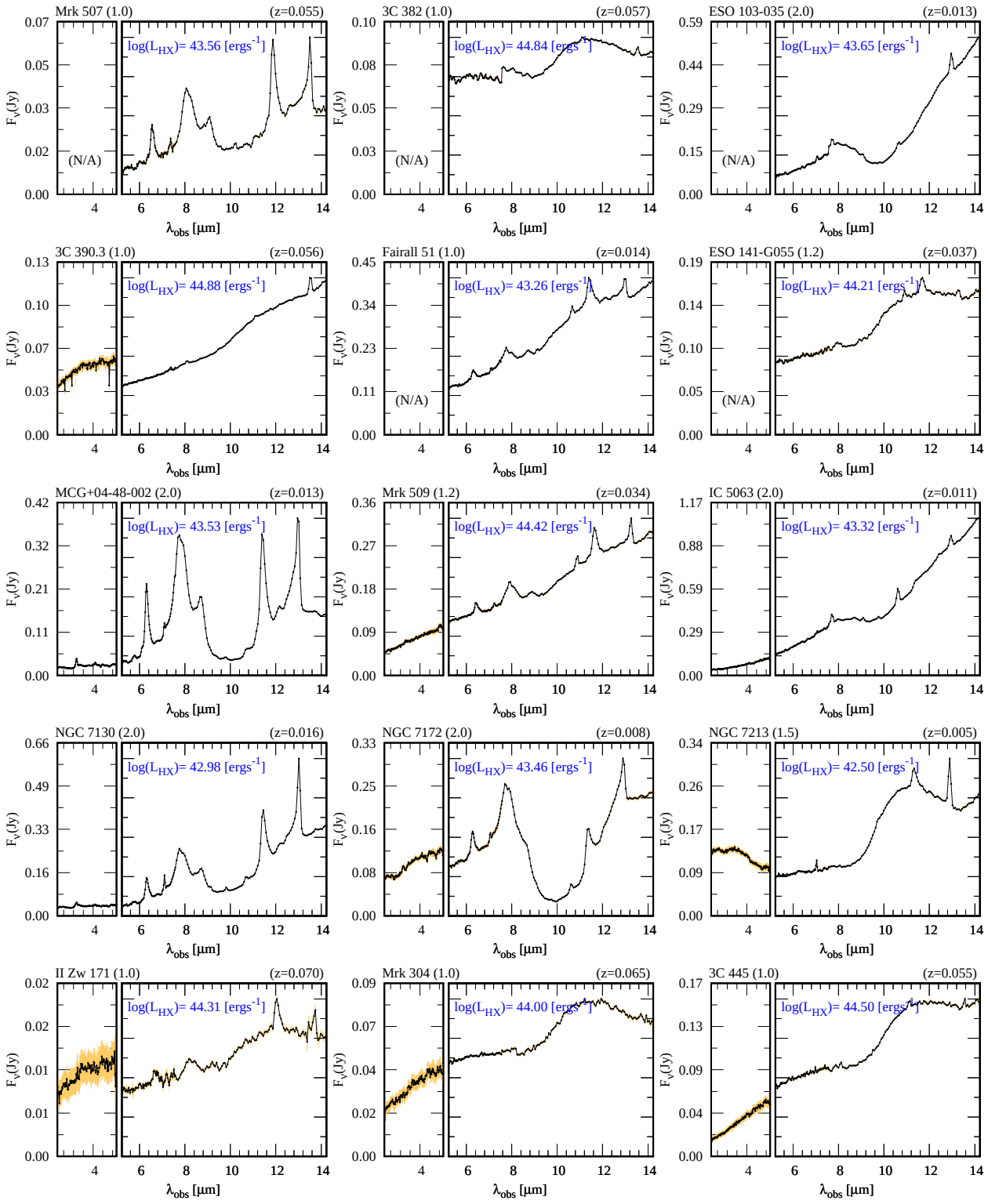

Figure 3.10: (Continued)

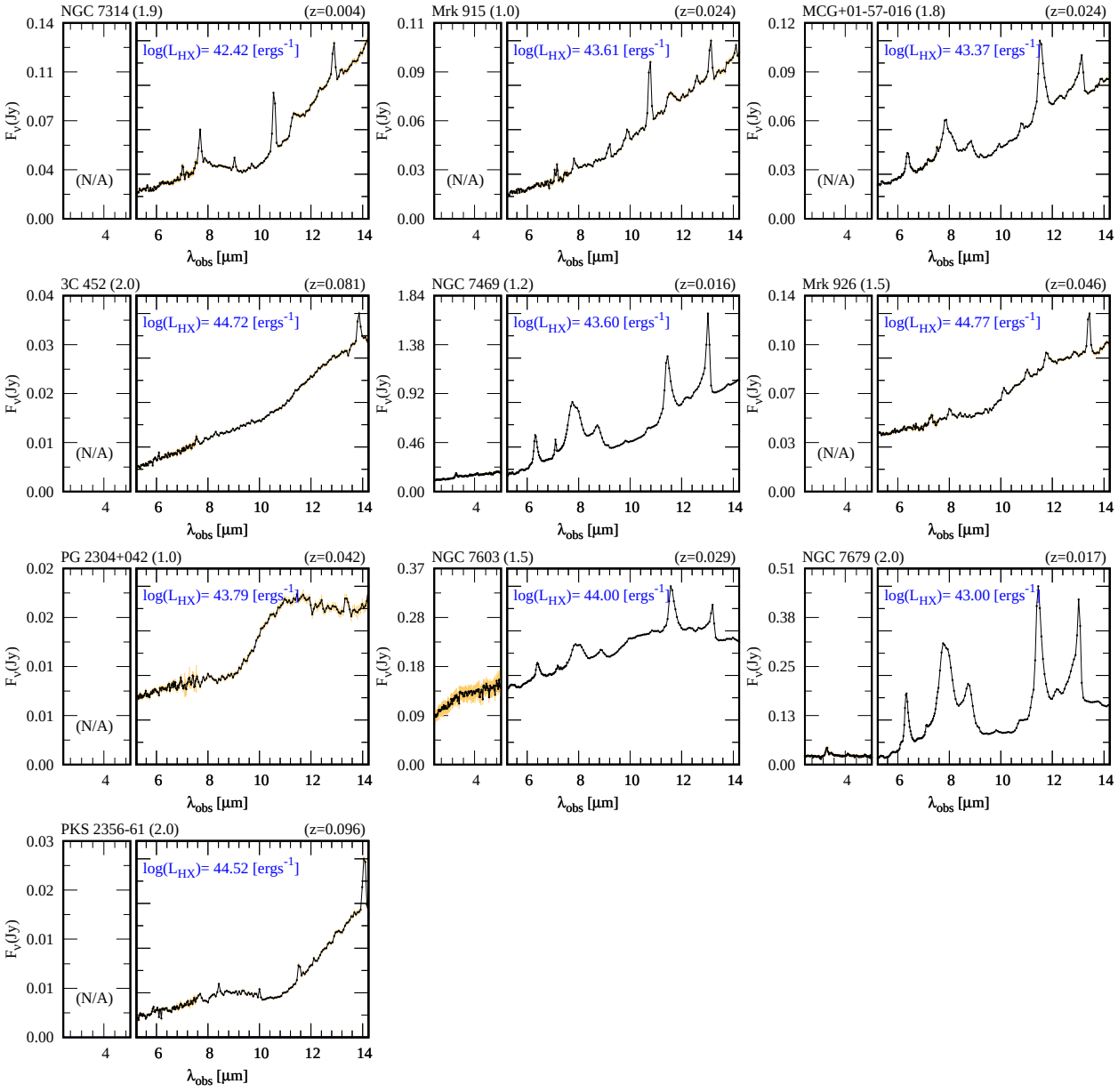

Figure 3.10: (Continued)

CHAPTER 4

PAH LINE STRENGTHS

4.1 The 3.3-3.4 μm AIB Complex

The software package MINUIT (James & Roos, 1975) has been used to obtain the fitted parameter values and errors for the following analysis. PAH emission is believed to originate from solid-state molecules, the line profile becomes Lorentzian (Smith et al., 2007; Yamada et al., 2013). However, for simplicity we model all the PAH lines by assuming Gaussian profiles (e.g. Imanishi et al., 2010; Ichikawa et al., 2014; Castro et al., 2014) By assuming a single Gaussian component for the 3.3 μm PAH emission feature we determined the flux peak, the central wavelength and the dispersion σ of the line profile based on the χ^2 minimization over a local continuum. The line flux is the integration over the Gaussian profile.

We have modeled a local continuum level in the rest-frame wavelength range between 3.15 and 3.35 μm with a power-law, if no notable feature exists near 3.3 μm. In some cases, there are nearby features such as the 3.1 μm H_2O ice covered dust and the 3.4 μm PAH sub-peak. In these cases, we have included these features in the fitting process (see Figure 4.1). In all cases with apparent PAH 3.3 μm emission feature, we see the 3.1 μm absorption. In some cases, we see the 3.4 μm PAH sub-peak. In order to determine the 3.3 μm feature parameters, we fit the rest-frame $2.75 < \lambda[\mu m] < 3.85$ sprectrum $[f_{\rm rest}(\lambda)]$ with the form

$$f_{\rm rest}(\lambda) = A_{\rm PL}\lambda^{-\Gamma}\, e^{-\tau_{3.1}\, G(\lambda-\lambda_{3.1},\sigma_{3.1})} + f_{3.3}\, G(\lambda-\lambda_{3.3},\sigma_{3.3}) + f_{3.4}\, G(\lambda-\lambda_{3.4},\sigma_{3.4}) \qquad (4.1)$$

The fitting parameters are $A_{\rm PL}$, Γ, $\tau_{\rm X}$,$f_{\rm X}$,$\lambda_{\rm X}$ and σ_X, where the subscript X (3.1,3.3 or 3.4) represents the nominal wavelength (in μm) of the feature. The first term represents the underlying power-law continuum with normalization $A_{\rm PL}$ and index Γ, multiplied by the 3.1 μm ice covered dust absorption feature with an effective optical depth $\tau_{3.1\ \mu{\rm m}}$ simultaneously fitted. The second and third terms represent the PAH 3.3 μm emission feature and the 3.4 μm sub-peak respectively with line fluxes $f_{\rm X}$ and width $\sigma_{\rm X}$. The function $G(\lambda,\sigma) = 1/(\sqrt{2\pi}\sigma)\exp(-\lambda^2/2\sigma^2)$ is the Gaussian function normalized to unity. The central wavelengths are allowed to vary slightly near the nominal wavelength of each feature during the fit. The third term (the 3.4 μm PAH emission sub-peak) is included in the fit if the sub-peak is clearly visible.

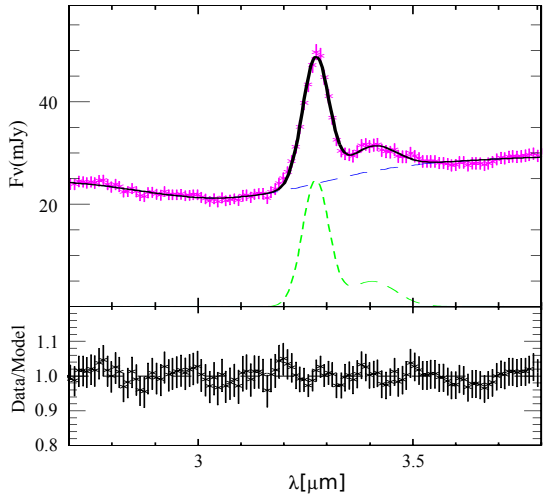

Figure 4.1: Fitting of the 3.3 μm PAH feature using a local power-law local continuum and a Gaussian emission profile. When are present, the 3.1 μm H_2O ice and 3.4 μm sub-peak are also considered.

In some particular cases presenting nearby features, such as the 3.1 μm H_2O ice covered dust and the PAH 3.4 μm sub-peak, we included these features in the fitting process using the Equation 4.1.

From the subsample of detected 3.3 μm PAH emission features Gaussian $\sigma_{3.3}$ parameter was found to range from 0.025 μm to 0.04 μm, with an average value of 0.030 μm. For those objects for which the PAH 3.3 μm is not visible or only marginally visible, we fixed the parameters $\lambda_{3.3}$ and $\sigma_{3.3}$ to 3.28 and $0.030\ \mu m$ respectively and investigated the variation of χ^2 as a function of $f_{3.3} \geq 0$. If the minimum χ^2 (best-fit case) is smaller than 2.7 below the χ^2 value at $f_{3.3} = 0$, we consider the line detected and report the best-fit $f_{3.3}$, otherwise, we consider it a non-detection and report the 90% upper limit to $f_{3.3}$ corresponding to $\Delta\chi^2 = 2.7$

from the best-fit value.

All fitted fluxes and luminosities of the 3.3 μm PAH emission lines of the AGNs from our X-ray AGN selected sample are summarized in Table 5.5. For the PAH fluxes, 1σ errors are reported for detections and the 90% upper limits are reported for non-detections. We have converted our 3.3 μm flux to the line luminosity according to relation

$$\mathrm{L}_{\lambda,\mathrm{line}} = 4\pi \mathrm{D_L}^2 \mathrm{F}_{\lambda,\mathrm{line}} \tag{4.2}$$

where $\mathrm{D_L}$ is the luminosity distance of the source. This quantity was computed through numerical integration by the Romberg's method using the equation

$$\mathrm{D_L} = (1+z)\,\frac{\mathrm{c}}{\mathrm{H_o}} \int_0^z \frac{dz'}{[\Omega_m(1+z)^3+\Omega_\Lambda]^{0.5}} \tag{4.3}$$

Throughout thiswork,we have considered the cosmological parameters H_o = 75 km s^{-1} Mpc^{-1}, $\Omega_m = 0.3$ and $\Omega_\Lambda = 0.7$. The infrared flux density from a point source is commonly given in units of Jansky (Jy), we have to consider that 1 Jy = 10^{-23} erg s^{-1} cm^{-2} Hz^{-1} = 10^{-26} W m^{-2} Hz^{-1} = F_ν, and then convert F_ν to F_λ using

$$\mathrm{F}_{\lambda,\mathrm{line}} = \mathrm{F}_{\nu,\mathrm{line}} \times c/(\lambda_{\mathrm{line}})^2 \tag{4.4}$$

Also, given that for the Akari/IRC data the wavelengths are provided in units of μm, flux densities in units of mJy and that source where observed at a particular redshift (z), the actual conversion is

$$\mathrm{F}_{\lambda,\mathrm{line}}[\mathrm{erg\ s^{-1}\ cm^{-2}}] = \mathrm{g_{norm}}[\mathrm{mJy\ \mu m}] \times 10^{26}[\mathrm{erg\ s^{-1}\ cm^{-2}\ Hz^{-1}}] \times \frac{3\mathrm{x}10^{24}[\mu\mathrm{m\ Hz}]}{(\lambda[\mu\mathrm{m}])^2} \times (1+\mathrm{z}) \tag{4.5}$$

where g_{norm} is the normalization factor from the fitted Gaussian function.

4.2 The 6.2 μm and 11.3 μm emission fittings

A procedure similar to that described in Section 4.1 used for fitting the 3.3 μm PAH emission line was used to fit the emission from the 6.2 μm and 11.3 μm PAH lines in the mid-IR band using data from the Spitzer/IRS instrument. In this cases we used a simpler model described by a local power-law continuum and a Gaussian emission line

$$f_{\rm rest}(\lambda) = A_{\rm PL}\lambda^{-\Gamma} + f_X\ G(\lambda - \lambda_X, \sigma_X) \tag{4.6}$$

where X can be the 6.2 or the 11.3 μm lines. An example of this fittings is shown in Figure 4.2. The derived luminosities are summarized in Table 5.5 besides other useful IR data (e.g. IRAS derived $L_{\rm IR}$ in the 8–1000 μm band and the 2MASS J, H and K magnitudes).

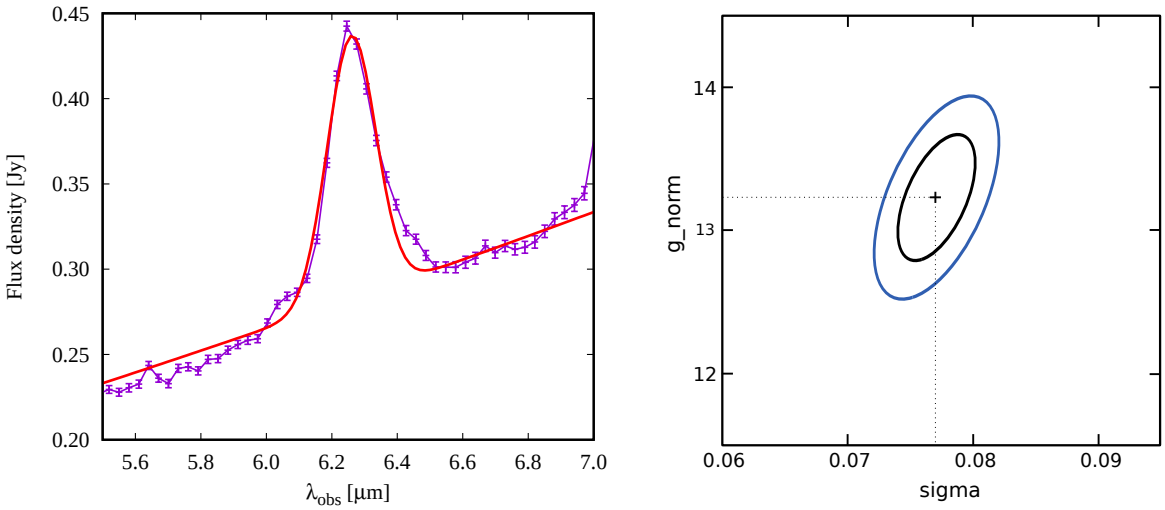

Figure 4.2: Fitting example of the 6.2 μm line *(left)* for a random source of our X-ray/IR AGN selection, and the σ–$g_{\rm norm}$ confidence contours for a different randomly selected source 6.2 μm fitting. 30 points were used along each axis and the range was calcualted automatically The two contours are drawn at the 68.3% (in blue) and 90% confidence levels (in black).

CHAPTER 5

RESULTS

5.1 Circumnuclear SFR properties derived from the early near-IR sample

This section is taken from

Castro et al. 2014, PASJ, 66, 110

Published: Nov. 21, 2014

In Castro et al. (2014) we explored the relationships between the 3.3 μm PAH feature and AGN properties of an early sample of 54 hard X-ray selected bright AGNs, including both Seyfert 1 and Seyfert 2 type objects, using spectroscopic data from the Akari/IRC instrument. The sample was selected from the 9-month Swift/BAT survey in the 14–195 keV band and all of them have measured X-ray spectra at E $\leq$ 10 keV. These X-ray spectra provide $\mathrm{N_H}$ measurements towards the AGNs. We use $\mathrm{L_{3.3\ \mu m}}$ as a proxy for SF activity and $\mathrm{L_{14-195keV}}$ as an indicator of the AGN activity. We search for possible differences in SF activity between type 1 (unabsorbed) and type 2 (absorbed) AGNs. We have made several statistical analyses taking the upper-limits of the 3.3 μm PAH line into account utilizing survival analysis methods. The results of our $\log(\mathrm{L_{14-195keV}})$ versus $\log(\mathrm{L_{3.3\ \mu m}})$ regression show a positive correlation and the slope for the type 1/unobscured AGNs is steeper than that of type 2/obscured AGNs at a 3σ level. Our analysis also shows that the circumnuclear star formation is more enhanced in type 2/absorbed AGNs than type 1/unabsorbed AGNs for low X-ray luminosity/low Eddington-ratio AGNs, while there is no significant dependence of SF activities on the AGN type in the high X-ray luminosities/ Eddington ratios.

5.1.1 The Regression Analysis and Statistical Tests

The analysis of the Akari/IRC early sample involves both detections and non-detections of the 3.3 μm PAH feature. In this case, usual statistical techniques are no longer applicable. To study data containing both detections and non-detections, we apply a series of survival analysis methods to the data using the ASURV package (Feigelson & Nelson (1985); Isobe et al. (1986); Lavalley et al. (1992)) to account for upper-limits (left censorship) of the 3.3 μm line luminosity. In Table 5.1 we explored the correlation between $\log(\mathrm{L}_{14-195\mathrm{keV}})$ and $\log(\mathrm{L}_{3.3\ \mu\mathrm{m}})$ as well as the correlation between the luminosities normalized by the black hole mass (M_{BH}). The M_{BH} presented in this work were collected from the literature where mass is derived from the 2MASS K-band stellar magnitudes (Mushotzky et al. (2008); Vasudevan et al. (2009); Winter et al. (2009)). These authors, in turn, followed Vovak et al. (2006) to obtain BH masses for each AGN in their samples using the relations: $\log(\mathrm{M}_{\mathrm{BH}}) = 8.19 + 0.524 \times (-\mathrm{M}_{\mathrm{K(stellar)}} - 23)$ or $\log(\mathrm{M}_{\mathrm{BH}}) \approx 1.23 \times \mathrm{L}_{\mathrm{K(stellar)}}$. The assumption made, in computing the mass, is that the K-band stellar light is dominated by the bulge (Winter et al., 2009). In addition, Mushotzky et al. (2008) show that the derived stellar luminosity is not correlated with the $\mathrm{L}_{14-195\mathrm{keV}}$ but that the nuclear luminosities are. However, Mushotzky et al. (2008) also mention that there are overestimates to the nuclear flux, since no provision is made for the contribution of the galaxy light in the central region (e.g. host dust emission from the torus itself).

Because of the presence of a scaling relation between the M_{BH} and the stellar mass of the bulge, the variable $\mathrm{L}_{3.3_{\mu\mathrm{m}}}/\mathrm{M}_{\mathrm{BH}}$ can be considered a proxy for specific star formation rate (sSFR). The variable $\mathrm{L}_{14-195\mathrm{keV}}/\mathrm{M}_{\mathrm{BH}}$ is a proxy to Eddington ratio ($\lambda_{\mathrm{Edd}} \equiv \mathrm{L}_{\mathrm{bol}}/\mathrm{L}_{\mathrm{Edd}}$), where $\mathrm{L}_{\mathrm{bol}}$ is the bolometric luminosity of the AGN and $\mathrm{L}_{\mathrm{Edd}} = 1.26 \times 10^{38}(\mathrm{M}_{\mathrm{BH}}/\mathrm{M}_{\odot})[\mathrm{erg\,s}^{-1}]$ is the Eddington luminosity or the limit where gravitational and radiation pressure are balanced.

To test the difference of star formation activities between different types of AGNs the following correlation analysis have been made. First, based on Tueller et al. (2008) optical classification, we divide our sample into two sub samples of optical type 1 AGNs and optical type 2 AGNs. Second, we repeated the analysis but in a column density classification scheme. We called X-ray type 1 AGNs the objects with $\mathrm{N}_{\mathrm{H}} \leq 10^{22}\ \mathrm{cm}^{-2}$ and X-ray type 2 those objects with $\mathrm{N}_{\mathrm{H}} > 10^{22}\ \mathrm{cm}^{-2}$.

In order to explore a posible correlation between the two variables the Cox regression method (where only the dependent variable have censored data) was employed. The parametric E-M (estimate and maximize) algorithm was used to determine the slope coefficients in a linear regression model. This method is a general approach to the problem of finding maximum likelihood estimates for censored data sets (Isobe et al., 1986) assuming a normal distribution of residuals. If censored data are not present this method yields the usual least-square results.

To test the hypothesis that $\mathrm{L}_{3.3\ \mu\mathrm{m}}/\mathrm{M}_{\mathrm{BH}}$ for Seyfert 1 and Seyfert 2 objects have the same distribution, the Gehan's extension of the Wilcoxon test, logrank test and Peto-Peto tests were used. We report the survival analysis probabilities, P, from the mentioned tests in Table 5.2. It shows that the probability that the distribution of 3.3 μm PAH luminosities of Seyfert 1 and Seyfert 2 objects from our sample is the same. A P value ≤ 0.05 means that the two-subsamples differ at a statistically significant level, otherwise they are consistent with belonging to the same parent population (LaMassa et al., 2012). Similar analysis was carried out for non-M_{BH} normalized data (see Table 5.2). The Kaplan-Meier (K-M) estimator was used to obtain mean values for each sub-sample with the TWOST application under ASURV. These tests are made for sub-samples divided by $\mathrm{L}_{14-195\mathrm{keV}}/\mathrm{M}_{\mathrm{BH}}$ and $\mathrm{L}_{14-195\mathrm{keV}}$ for the tests for $\mathrm{L}_{3.3\mu\mathrm{m}}/\mathrm{M}_{\mathrm{BH}}$ and $\mathrm{L}_{3.3\ \mu\mathrm{m}}$ respectively.

For the type 1 vs type 2 comparisons of $\mathrm{L}_{3.3\ \mu\mathrm{m}}$ of the low $\mathrm{L}_{14-195\mathrm{keV}}$ ($\mathrm{Low}-\mathrm{L}_{\mathrm{X}}$) and high $\mathrm{L}_{14-195\mathrm{keV}}$ ($\mathrm{High}-\mathrm{L}_{\mathrm{X}}$) samples, we further verify the statistical significance of the comparisons using the Bootstrap resampling method. We generate N_{boot} bootstrapped samples from each of the high and low $\mathrm{L}_{14-195\mathrm{keV}}$ samples. Each such bootstrapped sample contains the same number of objects (n_{obj}) as the original sample and each object in the bootstrapped sample is a random selection from the original sample, in which an object in the original may be selected in duplicate. The distribution of a statistical measure (e.g. mean value) from the N_{boot} redrawn samples is a good approximation of that from samples (each with a size of n_{obj}) randomly drawn from the underlying population. For each redrawn sample, we run the TWOST application, which gives the mean $\langle\log(\mathrm{L}_{3.3\ \mu\mathrm{m}})\rangle$ for each of the type 1 and type 2 AGNs. Since our interest is to see whether there is any systematic difference between type 1 and type 2 AGNs, we make a histogram of the difference $\langle\log(\mathrm{L}_{3.3\ \mu\mathrm{m}})\rangle_{\mathrm{Sy1}} - \langle\log(\mathrm{L}_{3.3\ \mu\mathrm{m}})\rangle_{\mathrm{Sy2}}$ from the $N_{\mathrm{boot}} = 600$ bootstrapped samples to

verify the significance of the difference.

Since one of the major advantages of our sample is to have X-ray based $\mathrm{N_H}$ measurements for all AGNs, we can further explore the correlation using the $\mathrm{N_H}$ values rather the type 1/type 2 dichotomy. Thus we also investigate the correlation of $\mathrm{L_{3.3\ \mu m}/M_{BH}}$ and $\mathrm{L_{3.3\ \mu m}}$ with $\mathrm{N_H}$. These tests should measure the "type" or "absorption" dependence of SFR/sSFR without making somewhat arbitrary decisions about type 1/type 2 borders.

Based on our data analysis we do not find large discrepancy between the X-ray and optical classifications. Almost half of the sources, 26/54 (48%), have optical classifications of Sy 1-1.5. The mean X-ray column density for these objects corresponds to a low column density object (un-absorbed) with a $\langle \log(\mathrm{N_H}) \rangle = 20.83$. The 1.6-2.0 optically classified sources (28/54; 52%) have as expected a higher column density, $\langle \log(\mathrm{N_H}) \rangle = 23.35$. When we use the X-ray criteria the proportion is similar: 24 X-ray type 1 sources (44%) and 30 X-ray type 2 sources (56%).

We applied the generalized Cox's proportional hazard model to compute the correlation probabilities along with the E-M algorithm which calculates the linear regression coefficients. The results of the regressions are summarized in Table 5.1.

The results of our series of linear regression analyses using the E-M method are expressed through the generic expression $\log(A_i) = a_i \ \{\log(B_i) - c_i\} \ + \ b_i$, where A_i is the independent variable, B_i is the dependent variable, a_i is the slope of the curve, b_i is the abscissa intersection point, and c_i is the average value of the corresponding independent variable of the given relationship. The origin point of the distribution has been shifted to the average value of the independent variable in order to minimize the artificial correlation of errors of the a_i and b_i parameters. This is needed because ASURV does not provide the covariance matrix of parameter errors. We have studied the dependencies between the luminosity of the PAH at $\lambda_{\mathrm{rest}} = 3.3$ μm ($\mathrm{L_{3.3\ \mu m}}$) emission line to the X-ray luminosity in the 14–195 keV band:

$$\log(\mathrm{L_{3.3\ \mu m}}) = a_0 \ \{\log(\mathrm{L_{14-195keV}}) - c_0\} \ + \ b_0 \tag{5.1}$$

Likewise, we express the relationship between the black-hole mass normalized luminosities:

$$\log(\mathrm{L}_{3.3\ \mu\mathrm{m}}/\mathrm{M}_{\mathrm{BH}}) = a_1\ \ \{\log(\mathrm{L}_{14-195\mathrm{keV}}/\mathrm{M}_{\mathrm{BH}}) - c_1\}\ +\ b_1. \tag{5.2}$$

A similar procedure was performed to explore a possible relationship between $\mathrm{N_H}$ and $\mathrm{L}_{3.3\ \mu\mathrm{m}}$ ($\mathrm{L}_{3.3\ \mu\mathrm{m}}/\mathrm{M}_{\mathrm{BH}}$):

$$\log(\mathrm{L}_{3.3\ \mu\mathrm{m}}) = a_2\ \ \{\log(\mathrm{N_H}) - c_2\}\ +\ b_2 \tag{5.3}$$

$$\log(\mathrm{L}_{3.3\ \mu\mathrm{m}}/\mathrm{M}_{\mathrm{BH}}) = a_3\ \ \{\log(\mathrm{N}_H) - c_3\}\ +\ b_3 \tag{5.4}$$

The regressions have been made for all AGNs in our sample as well as for $\mathrm{L}_{14-195\mathrm{keV}}$ and $\mathrm{L}_{14-195\mathrm{keV}}/\mathrm{M}_{\mathrm{BH}}$-divided sub-samples for Equation 5.3 and Equation 5.4 respectively. The best-fit values and 1σ errors for each equation coefficient are given by the ASURV package and summarized in Table 5.1 and the scatter diagram with the best-fit lines are shown in Figure 5.2.

The average values of the independent variables used under this study are $c_0 = \langle \log \mathrm{L}_{14-195\mathrm{keV}}[\mathrm{erg\,s^{-1}}]\rangle = 43.64$, $c_1 = \langle \log \mathrm{L}_{14-195\mathrm{keV}}/\mathrm{M}_{\mathrm{BH}}[\mathrm{erg\,s^{-1}M_\odot}^{-1}]\rangle = 35.42$ and $c_2 = c_3 = \langle \log(\mathrm{N_H})[\mathrm{cm^{-2}}]\rangle = 22.23$.

As shown in Table 5.1, the probabilities that a correlation is not present for the $\log(\mathrm{L}_{14-195\mathrm{keV}})$ versus $\log(\mathrm{L}_{3.3\ \mu m})$ relationship is 0.01 and for $\log(\mathrm{L}_{14-195\mathrm{keV}}/\mathrm{M}_{\mathrm{BH}})$ versus $\log(\mathrm{L}_{3.3\ \mu\mathrm{m}}/\mathrm{M}_{\mathrm{BH}})$ is 0.002, implying that a correlation is present through the whole sample. We divided the sample according to the optical classification of the sources. The probability that a correlation in not present for the optical Seyfert 1 objects is 0.02 for the $\log(\mathrm{L}_{14-195\mathrm{keV}})$-$\log(\mathrm{L}_{3.3\ \mu\mathrm{m}})$ relationship and 0.005 for the M_{BH} normalized case, indicating significant correlations. For the optical Seyfert 2's, the probability that there is no correlation between $\mathrm{L}_{14-195\mathrm{keV}}$ and $\mathrm{L}_{3.3\ \mu\mathrm{m}}$ is 0.65, while the same probability is 0.1 between $\log(\mathrm{L}_{14-195\mathrm{keV}}/\mathrm{M}_{\mathrm{BH}})$ and $\log(\mathrm{L}_{3.3\ \mu\mathrm{m}}/\mathrm{M}_{\mathrm{BH}})$. Thus no significant correlation has been found between the AGN power and star-formation rate in Seyfert 2 galaxies. The correlation is marginal in the normlized case for Seyfert 2's.

Table 5.1: Linear regression parameters obtained using the E-M method under ASURV.

$\log(L_{3.3\ \mu m}) = a_0\ \{\log(L_{14-195keV}) - c_0\} + b_0$						
Sample	No.	Up.[a]	a_0	b_0	$\langle\log(L_{3.3\ \mu m})\rangle$	P[b]
All AGNs	54	30	0.42±0.14	40.20±0.11	40.07±0.12	0.01
Optical type 1	26	20	1.05±0.27	39.92±0.24	39.68±0.22	0.02
Optical type 2	28	10	0.11±0.17	40.27±0.12	40.23±0.11	0.66
X-ray type 1	24	19	1.11±0.35	39.83±0.33	39.61±0.24	0.05
X-ray type 2	30	11	0.12±0.18	40.23±0.12	40.19±0.11	0.56
$\log(L_{3.3\ \mu m}/M_{BH}) = a_1\ \{\log(L_{14-195keV}/M_{BH}) - c_1\} + b_1$						
Sample	No.	Up.[a]	a_1	b_1	$\langle\log(L_{3.3\ \mu m}/M_{BH})\rangle$	P[b]
All AGNs	54	30	0.73±0.17	31.97±0.13	31.88±0.13	0.002
Optical type 1	26	20	1.56±0.37	31.55±0.26	31.62±0.21	0.005
Optical type 2	28	10	0.62±0.23	32.16±0.16	32.01±0.16	0.10
X-ray type 1	24	19	1.59±0.43	31.48±0.33	31.53±0.21	0.006
X-ray type 2	30	11	0.58±0.22	32.13±0.15	32.00±0.15	0.10
$\log(L_{3.3\ \mu m}) = a_2\ \{\log(N_H) - c_2\} + b_2$						
Sample	No.	Up.[a]	a_2	b_2	$\langle\log(L_{3.3\ \mu m})\rangle$	P[b]
All	54	30	0.14±0.09	40.02±0.14	40.07±0.12	0.003
$\log(L_{14-195keV}) \leq 43.64$	26	11	0.28±0.13	39.78±0.19	39.95±0.15	0.01
$\log(L_{14-195keV}) > 43.64$	28	19	-0.03±0.09	40.39±0.15	40.37±0.13	0.58
$\log(L_{3.3\ \mu m}/M_{BH}) = a_3\ \{\log(N_H) - c_3\} + b_3$						
Sample	No.	Up.[a]	a_3	b_3	$\langle\log(L_{3.3\ \mu m}/M_{BH})\rangle$	P[b]
All	54	30	0.22±0.12	31.71±0.19	31.88±0.13	0.075
$\log(L_{14-195keV}/M_{BH}) \leq 35.43$	25	13	0.15±0.10	31.44±0.15	31.52±0.12	0.12
$\log(L_{14-195keV}/M_{BH}) > 35.43$	29	17	0.20±0.14	32.23±0.23	32.42±0.14	0.17

[a] Number of upper-limits in the subsample.

[b] Correlation probability by Cox's proportional hazard model.

The sample has been also subdivided according to a X-ray column density classification scheme instead of the optical classification. We call the sources with $N_H \leq 10^{22}$ cm^{-2} "X-ray type 1 AGNs" and those with $N_H > 10^{22}$ cm^{-2} "X-ray type 2 AGNs". The results in Table 5.1 show that the difference between correlations in optical and X-ray AGN type division schemes are different by only about 4% from each

other. Figure 5.2 shows the scatter diagrams between $\log(L_{14-195keV})$ and $\log(L_{3.3\ \mu m})$ as well as between $\log(L_{14-195keV}/M_{BH})$ and $\log(L_{3.3\ \mu m}/M_{BH})$. The best-fit regressions for the all-AGN sample as well as type-divided samples are shown. The error range of the regression line corresponding to $\Delta\chi^2 < 2.3$ (68% confidence for the two interesting parameters) is also shown as a shaded area in each panel for the all-AGN sample. In both figures, the regression line of type 1 AGNs shows a steeper slope than that of type 2 AGNs. The tendency is common for optically-divided types and X-ray divided types. The differences of the slopes between type 1 and type 2 regression curves are at the 2-3σ levels.

Table 5.2: Two sample tests for optically and X-ray classified AGNs.

Class.	Criteria				$\langle\log(L_{3.3\ \mu m}/M_{BH})\rangle$		Gehan's	Logrank	Peto&Peto
		No.	n_1 [a]	n_2 [b]	Type 1	Type 2	Prob.	Prob.	Prob.
Optical	All AGNs	54	26	28	31.62±0.21	32.01±0.16	0.27	0.17	0.21
	$\log(L_X/M_{BH}) \leq 35.43$	25	10	15	31.17±0.15	31.66±0.13	0.14	0.09	0.12
	$\log(L_X/M_{BH}) > 35.43$	29	16	13	32.21±0.19	32.62±0.20	0.21	0.18	0.18
X-ray	All AGNs	54	24	30	31.53±0.21	32.00±0.15	0.34	0.14	0.20
Class.	Criteria				$\langle\log(L_{3.3\ \mu m})\rangle$		Gehan's	Logrank	Peto&Peto
		No.	n_1	n_2	Type 1	Type 2	Prob.	Prob.	Prob.
Optical	All AGNs	54	26	28	39.68±0.22	40.23±0.11	0.58	0.05	0.22
	$\log(L_X) \leq 43.64$	26	9	17	39.44±0.28	40.19±0.13	0.04	0.02	0.02
	$\log(L_X) > 43.64$	28	17	11	40.59±0.09	40.29±0.19	0.66	0.34	0.50
X-ray	All AGNs	54	24	30	39.61±0.24	40.19±0.11	0.80	0.08	0.37

[a] Number of type 1 objects contained in the sample.

[b] Number of type 2 objects contained in the sample.

To further verify this tendency, we have made further statistical tests. We divided the sample into high and low $L_{14-195keV}$ (or $L_{14-195keV}/M_{BH}$) and compared the mean $\log L_{3.3\ \mu m}$ (or $L_{3.3\ \mu m}/M_{BH}$) values of the type 1 and type 2 AGNs (see Table 5.2) using a number of two-sample tests available in ASURV. We used the Gehan's Generalized Wilcoxon test, logrank test and Peto & Peto Generalized Wilcoxon Test to determine the probability that the distributions of (s)SFR proxy among the type 1 and type 2 sub-samples are drawn from the same parent population separately for high and low $L_{14-195keV}$ (or $L_{14-195keV}/M_{BH}$)

regimes. The only statistically significant difference between the type 1 and type 2 samples in these two-sample tests are in the $\langle \log(L_{3.3\ \mu m}) \rangle$ values of low X-ray liminosity sample. The difference is marginal in the M_{BH} normalized case.

The basic results of the regressions involving N_H (see Equations 5.3 and 5.4) are as follows. We do not find significant correlations between $\log(N_H)$ and $\log(L_{3.3\ \mu m})$ for the all-AGN sample (see Figure 5.1(*a*)). However, if we divide the sample in two X-ray luminosity bins, a positive correlation has been observed in only low luminosity AGNs.

No significant correlation has been found between $\log(N_H)$ and $\log(L_{3.3\ \mu m}/M_{BH})$ relationship in any of the all, high $\log(L_{3.3\ \mu m}/M_{BH})$ and low $\log(L_{3.3\ \mu m}/M_{BH})$ samples (see Figure 5.1(*b*)).

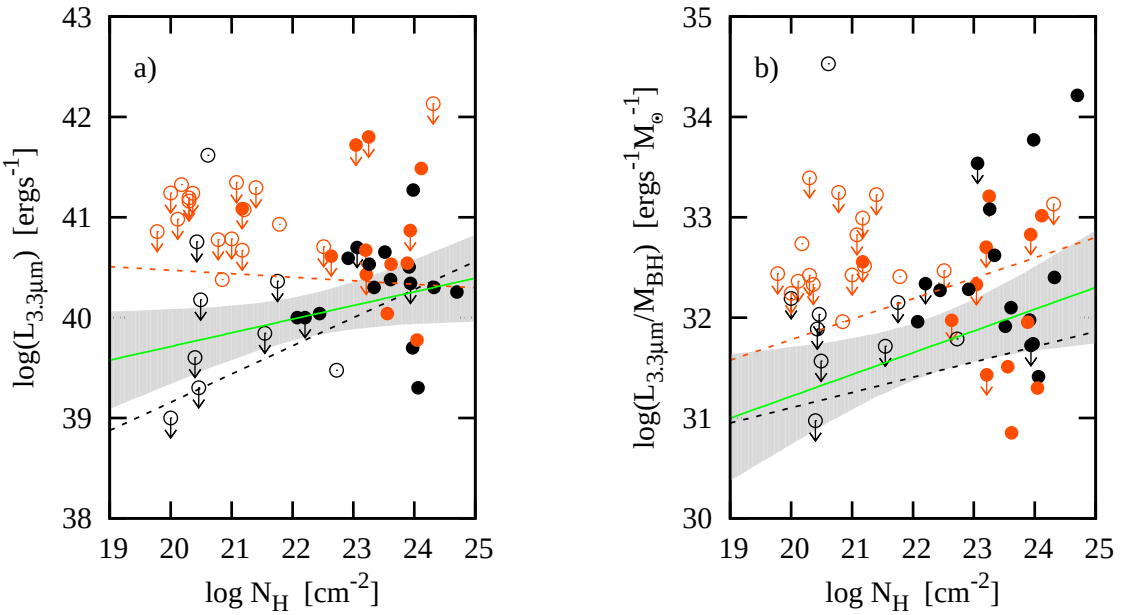

Figure 5.1: (*a*) $\log(L_{3.3\ \mu m})$ versus N_H relationship. Orange (paler) symbols have been used for AGNs with $\log(L_{14-195keV}) > 43.64$ and black for $\log(L_{14-195keV}) \leq 43.64$, orange and black dashed lines are the regression fits for the subsamples, respectively. (*b*) $\log(L_{3.3\ \mu m}/M_{BH})$ versus N_H relationship Orange symbols have been used for AGN with $\log(L_{3.3\ \mu m}/M_{BH}) > 35.43$ and black for $\log(L_{3.3\ \mu m}/M_{BH}) \leq 35.43$, orange and black dashed lines are the regression fits for the subsamples, respectively. Open circles are for X-ray type 1 objects and filled circles for X-ray type 2 objects. Arrows are for upper-limits. Solid green lines are the linear fits for the whole sample in each case. For numerical details see Table 5.1.

On the right vertical axis of Figure 5.2(*a*) the SFR, which is estimated by using the $L_{FIR} - L_{3.3\ \mu m}$ relation by Mouri et al. (1990) and the L_{FIR}−SFR relation by Kennicutt (1998) using:

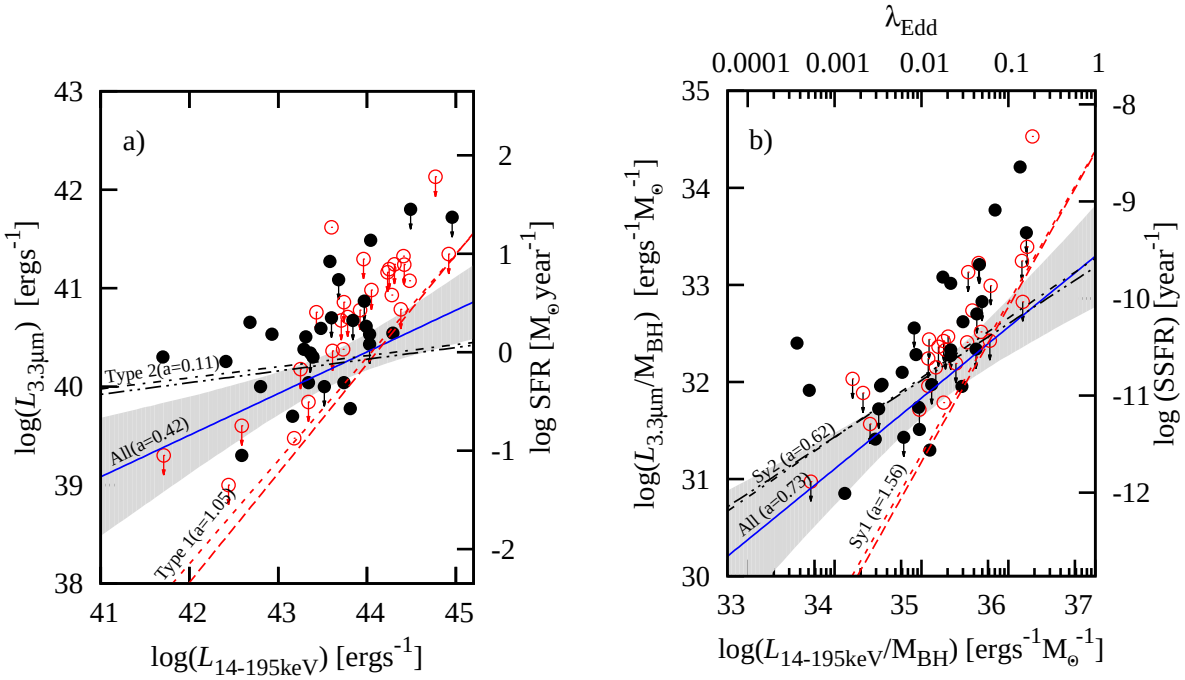

Figure 5.2: (*a*) $\log(\mathrm{L}_{14-195\mathrm{keV}})$ versus $\log(\mathrm{L}_{3.3\ \mu\mathrm{m}})$ and (*b*) $\log(\mathrm{L}_{14-195\mathrm{keV}}/\mathrm{M}_{\mathrm{BH}})$ versus $\log(\mathrm{L}_{3.3\ \mu\mathrm{m}}/\mathrm{M}_{\mathrm{BH}})$ relations. On the right vertical axis of panel (*a*), approximate star-formation rate corresponding to $\log(\mathrm{L}_{3.3\ \mu\mathrm{m}})$ are shown. Also on the upper horizontal and right vertical axes of panel (*b*), approximate Eddington ratios, λ_{Edd}, corresponding to the $\log(\mathrm{L}_{14-195\mathrm{keV}}/\mathrm{M}_{\mathrm{BH}})$ values and the specific star formation rate (sSFR) corresponding to $\log(\mathrm{L}_{3.3\ \mu\mathrm{m}}/\mathrm{M}_{\mathrm{BH}})$ are shown respectively. Arrows are for upper-limits. In each figure, the best-fit linear regression for all-AGN sample is shown in solid blue lines, while the error region is shown in gray shades. Open red circles are used for optical type 1 objects and filled black circles for optical type 2 objects. Red dashed and long-dashed lines corresponds to the regression lines for optical and X-ray type 1 objects, respectively. While the black dot-dashed and dot-dot-dashed lines corresponds to the regression lines for optical and X-ray type 2 AGNs, respectively.

$$\log(\mathrm{SFR})[\mathrm{M}_{\odot}\mathrm{year}^{-1}] = \log(\mathrm{L}_{3.3\ \mu\mathrm{m}}[\mathrm{erg\,s}^{-1}]) \ - \ 40.34 \tag{5.5}$$

On the upper horizontal axis of Figure 5.2(*b*), approximate Eddington ratios (see Equation 5.6), related to the $\mathrm{L}_{14-195\mathrm{keV}}/\mathrm{M}_{\mathrm{BH}}$ values are indicated. The conversion has been made as follows. First, we convert from the 14–195 keV to unabsorbed 2-10 keV luminosity using an effective photon index of $\Gamma = 1.85$, which implies $\mathrm{L}_{2-10\mathrm{keV}}/\mathrm{L}_{14-195\mathrm{keV}} = 0.41$. This is based on Ueda et al. (2011), where average effective photon index between these two bands range from $\Gamma \approx 1.7$ at the low luminosity end to $\Gamma \approx 2.0$ in the low luminosity end. For the bolometric correction from 2-10 keV, we use $\mathrm{L}_{\mathrm{bol}}/\mathrm{L}_{2-10keV} = 14$, from Lusso et

al. (2012) for $\log(\mathrm{L}_{2-10\mathrm{keV}}) \approx 43.2$ type 1 AGNs, which is the average 2-10 keV unabsorbed luminosity of AGNs in our sample implied from the mean $\langle(\log \mathrm{L}_{14-195\mathrm{keV}})\rangle$.

$$\lambda_{\mathrm{Edd}} = \mathrm{L}_{\mathrm{Bol}}/\mathrm{L}_{\mathrm{Edd}} \sim 5 \times 10^{-38}(\mathrm{L}_{14-195\mathrm{keV}}[\mathrm{erg\ s^{-1}}]/\mathrm{M}_{\mathrm{BH}}[\mathrm{M}_{\odot}]) \tag{5.6}$$

The rough sSFR scale on the right axis of Figure 5.2(*b*) is determined based on the combination of Equation 5.5, the $\mathrm{M}_{BH} - \mathrm{L}_{K(\mathrm{stellar})}$ relation from Mushotzky et al. (2008) and the stellar mass to K-band luminosity ratio, $\mathrm{M}_{\mathrm{stellar}}/\mathrm{L}_{\mathrm{K(stellar)}} \sim 0.8$ (in solar units) (Brinchmann & Ellis, 2000). The M_{BH} dependence of the ratio $\mathrm{M}_{\mathrm{BH}}/\mathrm{L}_{K(\mathrm{stellar})}$ is neglected and is evaluated at $\log(\mathrm{M}_{\mathrm{BH}}) = 8.27$, which is the mean value for our sample.

$$\log(\mathrm{sSFR})[\mathrm{year}^{-1}] = \log(\mathrm{L}_{3.3\ \mu\mathrm{m}}[\mathrm{erg\,s^{-1}}]) - \log(\mathrm{M}_{\mathrm{BH}}[\mathrm{M}_{\odot}]) \ - \ 42.87 \tag{5.7}$$

Since there is significant scatter and luminosity/mass dependence in the conversions involved, these relations are only accurate to an order of magnitude.

The most significant result of our tests is the excess of $\mathrm{L}_{3.3\ \mu\mathrm{m}}$ of type 2/absorbed AGNs with respect to that of type 1/unabsorbed AGNs at low $\mathrm{L}_{14-195\mathrm{keV}}(\mathrm{Low} - \mathrm{L_X})$. However, this excess is not observed at high $\mathrm{L}_{14-195\mathrm{keV}}$ $(\mathrm{High} - \mathrm{L_X})$. These results are worth scrutinizing and therefore we made bootstrap resampling to the each of the high and low $\mathrm{L}_{14-195\mathrm{keV}}$ samples as described in Section 5.1.1. The bootstrap histograms of $\Delta_{12} \equiv \langle\log \mathrm{L}_{3.3\ \mu\mathrm{m}}\rangle_{\mathrm{Sy1}} - \langle\log \mathrm{L}_{3.3\ \mu\mathrm{m}}\rangle_{\mathrm{Sy2}}$ for 600 redrawn samples for each of the high and low $\log \mathrm{L}_{14-195\mathrm{keV}}$ sub-samples are shown in Figure 5.3. In some redrawn samples where there are too many upper limits, the TWOST routine cannot determine the mean $\langle\log(\mathrm{L}_{3.3\ \mu\mathrm{m}})\rangle_{\mathrm{Sy1}}$ value and instead gives an NaN (not a number). There are 9/600 and 78/600 such for the high and low $\mathrm{L}_{14-195\mathrm{keV}}$ samples respectively. In these cases, we use the upper limit values to calculate the mean. The histograms of these cases are also overplotted in Figure 5.3 under thick lines and indicated by symbols '<<<<<<'.

The bootstrap histogram shows that only 29 out of 600 bootstraps (5%) show $\langle\log(\mathrm{L}_{3.3\ \mu\mathrm{m}})\rangle_{\mathrm{Sy1}} - \langle\log(\mathrm{L}_{3.3\ \mu\mathrm{m}})\rangle_{\mathrm{Sy2}} > 0$ for the low $\mathrm{L}_{14-195\mathrm{keV}}$ sample, verifying the conclusion of the TWOST tests. This

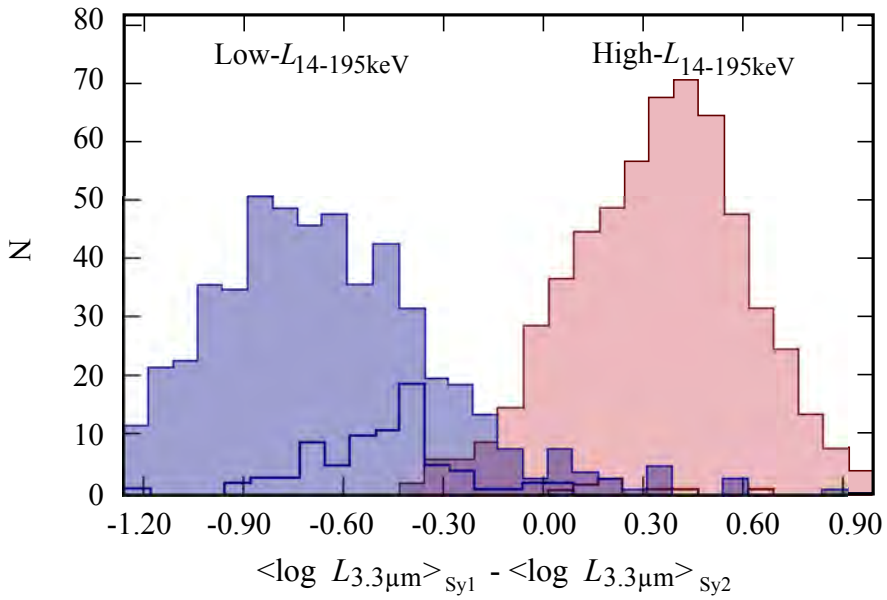

Figure 5.3: The bootstrap histograms of $\Delta_{12} = \langle \log \mathrm{L}_{3.3\ \mu\mathrm{m}} \rangle_{\mathrm{Sy1}} - \langle \log \mathrm{L}_{3.3\mu\mathrm{m}} \rangle_{\mathrm{Sy2}}$ are shown for the high $\mathrm{L}_{14-195\mathrm{keV}}$ (blue/darker histogram) and low $\mathrm{L}_{14-195\mathrm{keV}}$ (red/paler histogram) samples. The histograms below thick solid lines, which are labeled as a number of "<"'s show the cases where the TWOST routine fails to give $\langle \log \mathrm{L}_{3.3\ \mu\mathrm{m}} \rangle_{\mathrm{Sy1}}$ due to too many upper limits in the corresponding redrawn sample, in which the upper limits are used for the mean calculations.

percentage is an overestimate considering that ~ 4 of the 29 $\Delta_{12} > 0$ cases are upper limits. For the high $\mathrm{L}_{14-195\mathrm{keV}}$ sample, where the mean Δ_{12} is positive, 58 cases out of 600 bootstraps give $\Delta_{12} < 0$. Thus the SFR in more enhanced in type 1 than in type 2 sources in the high X-ray luminosity sample with only a marginal significance.

One important question is whether there is any systematic difference of Δ_{12} values between high and low $\mathrm{L}_{14-195\mathrm{keV}}$ samples. In order to test whether the Δ_{12} is significantly different between the high and low $\mathrm{L}_{14-195\mathrm{keV}}$ samples, we calculated the difference $(\Delta_{12,\mathrm{High}-\mathrm{L_X}} - \Delta_{12,\mathrm{Low}-\mathrm{L_X}})$ for 600 randomly selected high X-ray luminosity-low X-ray luminosity pairs from re-drawn samples (see Figure 5.4). The distribution of $(\Delta_{12,\mathrm{High}-\mathrm{L_X}} - \Delta_{12,\mathrm{Low}-\mathrm{L_X}})$ shows that the probability that it becomes less than zero by chance is only 0.75%.

In our early-sample near-IR study of the 3.3 μm PAH emission as a proxy of SFR of a sample of X-ray selected AGNs (Castro et al., 2014), we found strong correlation between the 14–195 keV X-ray luminosity

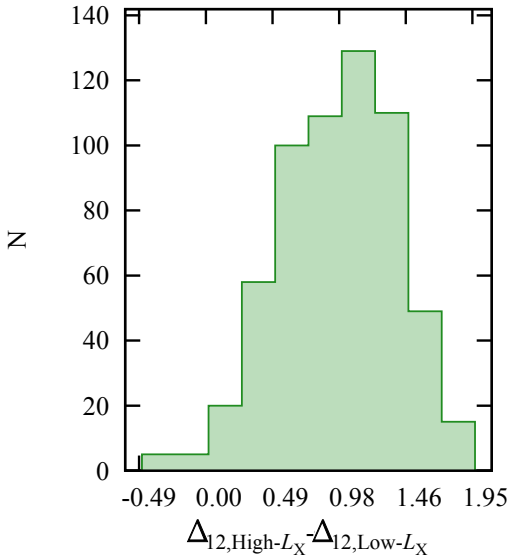

Figure 5.4: Histogram of the difference ($\Delta_{12,\mathrm{High-L_X}} - \Delta_{12,\mathrm{Low-L_X}}$) for 600 randomly selected high $L_{14-195\mathrm{keV}}$ and low $L_{14-195\mathrm{keV}}$ pairs from re-drawn samples, respectively. The distribution of ($\Delta_{12,\mathrm{High-L_X}} - \Delta_{12,\mathrm{Low-L_X}}$) shows that the probability that it becomes less than zero by chance is only 0.75%.

($L_{14-195\mathrm{keV}}$) and their SFR. No statistical difference was found in the mean circumnuclear SFR between type 1 and type 2 AGNs for the overall sample. However, limiting ourselves to low-luminosity AGNs, we have found stronger starburst activity in type 2 AGNs than type 1 AGNs, as well as a significant correlation between N_H and SFR. There is no significant difference in the star-forming activity between high luminosity type 1 and type 2 AGNs. Our previous results suggest that the difference between type 1 and type 2 in low luminosity AGNs may reflect an evolution sequence, where more obscuring material is available around low luminosity type 2 AGNs when the circumnuclear star formation is feeding the central engine. At high luminosities, the difference between the two types may be mainly from the orientation effect.

5.2 Preliminary results on Spitzer/IRS derived SFRs

The analysis procedures employed for the study of the early AGN sample were also used for the study of the circumnuclear SF properties but now using the measurements obtained by the study of the extended sample, which has data in the mid-IR Spitzer/IRS for 130 sources. The objective of the present research is

to determine the properties of circumnuclear star formation using the PAH emission line at 11.3 μm as the main indicator of such activity. We measured the lines using the MINUIT package. The results of these measurements involve the use of detections and upper-limits.

Using the 11.3 μm PAH feature luminosities (see Table 5.5) the SFR can be derived (as shown in Figure 5.5) by applying the Diamond-Stanic & Reike (2012) relation

$$\mathrm{SFR}\ [\mathrm{M}_{\odot}\ \mathrm{yr}^{-1}] = 9.6 \times 10^{-9}\ (\mathrm{L}_{11.3\ \mu\mathrm{m}}\ [\mathrm{L}_{\odot}]) \tag{5.8}$$

and because we know from the Swift/BAT survey the $\mathrm{L}_{14-195\mathrm{keV}}$ value for each source and also the intensity of the 11.3 μm PAH emission line, then a relation between $\mathrm{L}_{14-195\mathrm{keV}}$ and SFR can be established:

$$\mathrm{SFR}\ [\mathrm{M}_{\odot}\ \mathrm{yr}^{-1}] = a_0\ \ \{\log(\mathrm{L}_{14-195\mathrm{keV}}) + c_0\}\ +\ b_0 \tag{5.9}$$

As shown in Figure 5.6 strong correlation is found between 6.2 μm and 11.3 μm PAH feature. This, suggesting non-supression of the 6.2 μm PAH feature strength with respect to the presence of the 11.3 μm PAH feature in the sample here studied.

The IR luminosity of an individual source, scales with $\mathrm{L}_{14-195\mathrm{keV}}$. Studing the $\log(\mathrm{L}_{14-195\mathrm{keV}})$–SFR properties of the sample we have found no statistical difference in the mean circum-nuclear SFR, traced by the 11.3 μm PAH emission, for our overall extended sample (see Figure 5.5).

Table 5.3: Mid-IR linear regression parameters obtained using the E-M method.

$SFR = a_0 \ \{\log(L_{14-195\ keV}) - c_0\} \ + \ b_0$						
Sample	No.	Up.[a]	a_0	b_0	$\langle\log(SFR)\rangle$	P[b]
All AGNs	130	22	0.26±0.09	-0.69±0.06	-0.72±0.07	0.03
Seyfert 1s	65	12	0.30±0.13	-0.73±0.09	-0.68±0.10	0.17
Seyfert 2s	65	10	0.25±0.14	-0.68±0.10	-0.75±0.10	0.16

[a] Number of upper-limits in the subsample.

[b] Correlation probability by Cox's proportional hazard model.

When separated by optical type, the K-M estimator was used to obtain mean values for each sub-sample with the TWOST application under ASURV. As shown in Table 5.3, similar regression values are found for Seyfert 1 and Seyfert sources for the extended sample, but with better correlation probabilities (17 and 16%, respectively).

Table 5.4: Mid-IR two sample tests for optically classified AGNs.

Criteria				$\langle\log(SFR)\rangle$	$\langle\log(SFR)\rangle$	Gehan's	Logrank	Peto&Peto
	No.	n_1 [a]	n_2 [b]	Type 1	Type 2	Prob.	Prob.	Prob.
All AGNs	130	65	65	-0.68±0.10	-0.75±0.10	0.37	0.43	0.37
$\log(SFR) \vee L_X \leq 43.457$	60	20	40	-0.87±0.16	-0.78±0.12	0.60	0.82	0.60
$\log(SFR) \vee L_X > 43.457$	70	45	25	-0.52±0.10	-0.65±0.15	0.41	0.40	0.42

[a] Number of type 1 objects contained in the sample.

[b] Number of type 2 objects contained in the sample.

If we sub-divide by $L_{14-195keV}$ and optical type the K-M estimator can be used again (see Table 5.4). It seems that the low luminosity Seyfert 2s sub-sample presents stronger SFR compared to the low luminosity Seyfert 1s sub-sample. This, with Gehan's, log rank and Peto&Peto probabilities of 0.60, 0.82 and 0.60, respectively. However, since these probabilities implies the probability that the distribution of 11.3 μm PAH-derived SFRs of low-$L_{14-195keV}$ Seyfert 1s and low-$L_{14-195keV}$ Seyfert 2s from our sample to be the

same, it means that the two-subsamples do not differ at a statistically significant level.

If we repeat the same procedure, but this time for high-$L_{14-195keV}$ Seyfert 1s and high-$L_{14-195keV}$ Seyfert 2s (see Table 5.4) then we obtain Gehan's, log rank and Peto&Peto probabilities of 0.41, 0.40 and 0.42, respectively. Also implying that this sub-samples are not statistically differentiated at a significant level. Compared to our early sample, in this extended sample we find a number of type 1s with low-$L_{14-195keV}$ and high-SFR, which weakens the difference in SFR found for Seyfert 2 sources of low luminosity reported in Castro et al. (2014).

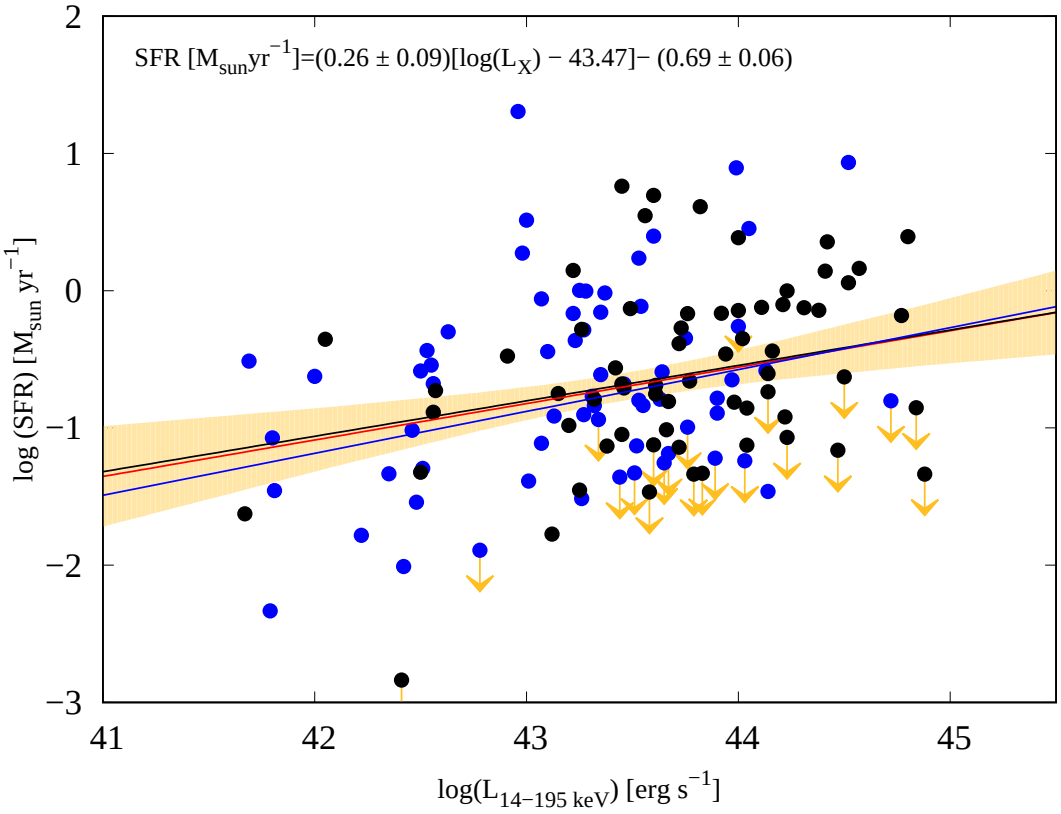

Figure 5.5: SFR properties of our X-ray selected mid-IR extended sample. Blue points are for optial type 2 while black points are used for type 1 sources. Arrows are for upper-limits. The best-fit linear regression for the all-AGN sample is shown in a solid red line, while the error region is shown shaded in light-red. The parametric E-M (estimate and maximize) algorithm was used to determine the slope coefficients (upper-left corner of the figure) in a linear regression model, where $\langle \log(L_{14-195\ keV}) \rangle = 43.457$.

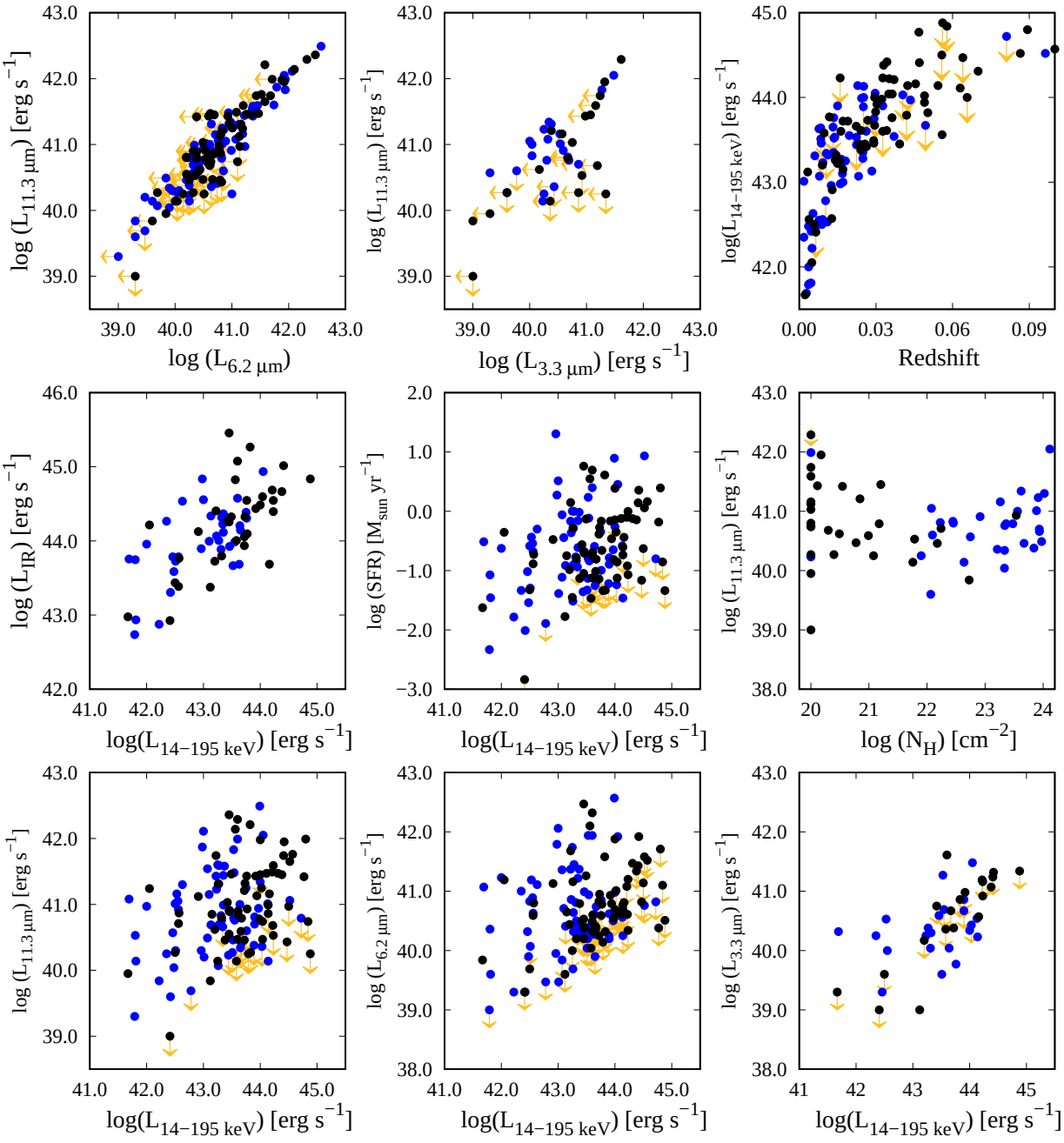

Figure 5.6: PAH properties and relations in the mid- and near- infrared 5–14 μm IR band. Blue points are for optical Syefert 2 sources, while black points are for Seyfert 1 sources. Downward golden arrows are related to the upper-limit of the y-variable. Leftward golden arrows are related to the upper-limits of the x-axis variable.

Table 5.5: Mid- and Near-Infrared

Name[a]	z	Type[b]	log(L_X)[c]	log(M_{BH})[d]	N_H [e]	J[f]	H[f]	K[f]	D_L	log($L_{3.3}$)	log($L_{6.2}$)	log($L_{11.3}$)	log(L_{IR})[g]	log(SFR)
			[erg s^{-1}]	[$M_\odot$]	[$\times 10^{22} cm^{-2}$]	[mag]	[mag]	[mag]	[Mpc]	[erg s^{-1}]	[erg s^{-1}]	[erg s^{-1}]	[erg s^{-1}]	[$M_\odot$ yr^{-1}]
Mrk 335	0.025	1.2	43.45	...	...	12.61	11.73	10.59	105.11	...	<40.53	40.91	10.74	-0.67
Mrk 1501	0.089	1.2	44.80	...	...	13.87	13.03	11.78	381.05	...	<41.71	41.99	...	0.39
Mrk 348	0.015	2.0	43.90	7.97	1.69	12.95	12.30	11.54	60.79	<40.67	40.20	40.81	...	-0.78
Mrk 1148	0.064	1.0	44.47	...	...	14.84	14.27	13.34	268.23	...	<40.82	<40.43	...	-1.16
NGC 526A	0.019	1.5	43.72	...	1.50	12.80	11.90	10.90	77.45	...	<40.25	40.46	10.42	-1.14
Fairall 9	0.047	1.2	44.41	8.91	0.01	13.05	12.10	11.11	194.67	<41.24	<41.43	41.74	11.50	0.14
NGC 612	0.029	2.0	44.05	8.47	129.70	13.17	12.23	11.72	121.72	41.48	41.92	42.05	11.42	0.45
ESO 297-018	0.025	2.0	44.00	9.68	41.71	13.42	12.66	12.06	102.68	40.34	40.98	41.34	...	-0.26
NGC 788	0.013	2.0	43.52	...	46.89	12.86	12.03	11.39	54.94	...	<40.20	40.46	10.15	-1.13
Mrk 1018	0.042	1.5	44.14	...	...	13.21	12.36	11.62	175.12	...	<40.69	<40.86	...	-0.73
Mrk 590	0.026	1.2	43.42	9.00	0.01	12.41	11.64	10.57	107.60	<40.75	<40.49	41.03	10.75	-0.56
IC 1816	0.016	1.8	43.10	...	...	12.72	11.95	11.44	68.61	...	40.71	41.15	10.48	-0.44
NGC 973	0.016	2.0	43.27	...	...	12.84	11.68	10.86	65.54	...	40.32	40.69	10.49	-0.90
ESO 198-024	0.045	1.0	44.16	8.36	0.01	13.39	12.46	11.48	188.18	40.57	40.81	41.16	10.17	-0.43
NGC 1052	0.005	2.0	42.22	...	...	11.00	10.40	9.81	20.21	...	39.30	39.84	9.36	-1.78
ESO 417-G006	0.016	2.0	43.26	...	...	12.83	12.06	11.70	65.93	...	39.69	40.07	...	-1.51
NGC 1365	0.005	1.8	42.63	8.88	104.8	11.34	10.24	9.22	21.90	...	41.11	41.30	11.02	-0.29
ESO 548-G081	0.014	1.0	43.32	...	0.01	11.98	11.31	10.53	58.52	...	40.20	40.80	10.28	-0.79
ESO 549-G049	0.026	2.0	43.60	...	0.01	12.83	11.93	11.23	107.21	...	41.94	41.99	11.06	0.39
ESO 157-23	0.043	2.0	43.97	...	...	13.81	12.77	11.96	179.77	...	40.50	40.94	...	-0.64
3C 120	0.033	1.0	44.38	8.56	0.16	12.66	11.71	10.57	135.28	41.07	<41.34	41.45	11.15	-0.14
MCG-02-12-050	0.036	1.2	43.76	...	...	13.73	13.02	12.30	149.34	...	<40.59	41.43	11.03	-0.16

Table 5.5(Continued.)

Name[a]	z	Type[b]	log(L_X)[c]	log(M_{BH})[d]	N_H [e]	J[f]	H[f]	K[f]	D_L	log($L_{3.3}$)	log($L_{6.2}$)	log($L_{11.3}$)	log(L_{IR})[g]	log(SFR)
			[erg s^{-1}]	[$M_\odot$]	[$\times 10^{22} cm^{-2}$]	[mag]	[mag]	[mag]	[Mpc]	[erg s^{-1}]	[erg s^{-1}]	[erg s^{-1}]	[erg s^{-1}]	[$M_\odot$ yr^{-1}]
MCG-01-13-025	0.015	1.2	43.25	...	...	12.82	11.99	11.22	64.31	...	<40.00	40.14	...	-1.45
CGCG 420-015	0.029	2.0	43.75	...	...	13.13	12.23	11.49	120.12	...	<40.83	41.25	10.87	-0.34
CGCG 468-002	0.018	2.0	43.25	...	...	...	...	...	73.74	...	41.74	41.60	...	0.00
Ark 120	0.032	1.0	44.23	8.74	0.01	12.04	11.20	10.22	134.04	<41.16	41.20	41.59	11.03	-0.00
Pictor A	0.035	1.0	44.04	...	0.06	13.69	12.96	12.58	143.89	...	<40.66	40.47	...	-1.12
IRAS 05218-1212	0.049	1.0	44.02	...	...	...	...	...	203.17	...	<41.01	41.25	...	-0.34
NGC 2110	0.007	2.0	43.63	8.28	2.84	11.93	11.06	10.14	31.32	...	40.27	40.80	10.17	-0.79
ESO 005-G004	0.006	2.0	42.46	7.89	5.58	12.61	11.41	10.56	25.64	39.30	40.32	40.57	10.27	-1.01
Mrk 3	0.013	2.0	43.76	8.48	1.24	11.97	11.00	10.64	54.56	39.77	40.85	<40.60	10.79	-0.99
ESO 426-G002	0.022	2.0	43.44	...	0.01	13.38	12.67	12.11	91.20	...	<40.25	<40.23	...	-1.35
ESO 121-G028	0.040	2.0	44.03	9.00	16.19	13.89	13.21	12.84	166.99	<40.43	<40.64	<40.36	...	-1.23
UGC 03478	0.012	1.2	42.57	...	...	12.94	11.99	11.23	51.54	...	40.80	40.87	10.25	-0.72
UGC 03601	0.017	1.5	43.15	...	...	13.34	12.57	11.93	69.34	...	40.65	40.85	...	-0.74
Mrk 78	0.037	2.0	43.54	...	...	12.69	12.08	11.73	152.71	...	40.94	41.48	...	-0.11
Mrk 10	0.029	1.2	43.46	...	...	13.33	12.84	12.20	119.56	...	<40.38	40.89	...	-0.70
IC 0486	0.026	1.0	43.73	...	...	12.88	12.23	11.68	109.64	...	40.95	41.32	10.81	-0.27
Mrk 1210	0.013	2.0	43.35	...	...	13.26	12.53	11.74	54.50	...	40.34	40.99	10.60	-0.61
Mrk 622	0.023	2.0	43.07	...	...	13.72	13.01	12.39	94.50	...	41.36	41.54	...	-0.05
PG 0804+761	0.100	1.0	44.57	...	...	12.97	12.08	10.91	429.61	...	<41.52	41.76	...	0.16
NGC 2655	0.004	2.0	41.81	...	...	10.37	9.54	9.39	18.73	...	39.60	40.14	9.42	-1.45
Mrk 18	0.011	2.0	42.53	7.45	18.25	13.89	13.21	12.84	44.70	40.53	41.19	41.16	...	-0.43
SBS 0915+556	0.049	2.0	43.67	...	...	14.65	13.88	13.22	204.89	...	<40.74	<40.41	...	-1.18
MCG-01-24-012	0.019	2.0	43.55	8.59	...	14.15	13.31	12.73	79.71	<40.69	<40.34	40.76	10.47	-0.83

Table 5.5(Continued.)

Name[a]	z	Type[b]	log(L_X)[c]	log(M_{BH})[d]	N_H [e]	J[f]	H[f]	K[f]	D_L	log($L_{3.3}$)	log($L_{6.2}$)	log($L_{11.3}$)	log(L_{IR})[g]	log(SFR)
			[erg s^{-1}]	[$M_\odot$]	[$\times 10^{22} cm^{-2}$]	[mag]	[mag]	[mag]	[Mpc]	[erg s^{-1}]	[erg s^{-1}]	[erg s^{-1}]	[erg s^{-1}]	[$M_\odot$ yr^{-1}]
MCG+04-22-042	0.032	1.2	43.98	...	...	13.01	12.32	11.66	132.51	...	<40.54	40.78	...	-0.81
Mrk 110	0.035	1.0	44.22	7.80	0.02	13.87	13.15	12.25	144.88	<41.19	<40.61	40.68	...	-0.92
Mrk 705	0.029	1.2	43.49	...	...	12.86	12.12	11.30	119.12	...	41.26	41.46	10.81	-0.13
MCG+10-14-025	0.039	1.5	43.45	...	...	13.49	12.26	14.89	162.09	...	42.47	42.36	11.94	0.76
NGC 2992	0.007	2.0	42.55	8.04	1.19	13.87	13.15	12.25	31.00	40.00	40.89	41.05	...	-0.54
MCG 05-23-016	0.008	2.0	43.51	7.66	...	12.08	11.24	10.34	34.14	39.60	<40.04	<40.27	...	-1.32
NGC 3081	0.007	2.0	43.07	7.96	94.2	12.56	11.97	11.43	32.08	...	<39.84	40.49	...	-1.11
NGC 3079	0.003	2.0	42.00	...	...	11.91	10.58	9.64	14.92	...	41.23	40.97	10.44	-0.62
ESO 374-G044	0.028	2.0	43.13	...	...	13.77	12.94	12.51	116.21	...	<40.41	40.69	10.82	-0.91
NGC 3227	0.003	1.5	42.56	7.83	1.74	11.26	10.52	9.92	15.47	...	40.59	40.71	9.87	-0.88
NGC 3281	0.010	2.0	43.34	8.62	86.3	13.14	12.14	11.28	43.02	...	<40.39	<40.66	10.71	-0.93
NGC 3393	0.012	2.0	42.96	...	...	12.44	11.70	11.40	50.48	...	39.95	40.30	10.38	1.30
Mrk 417	0.032	2.0	43.90	8.04	85.69	13.87	13.13	12.73	134.22	<40.86	<40.62	40.70	...	-0.89
NGC 3783	0.009	1.0	43.58	8.21	0.57	11.98	11.02	10.01	39.19	<40.36	<40.04	<40.14	10.49	-1.46
NGC 3786	0.008	1.8	42.50	...	...	12.47	11.53	10.85	35.95	...	40.83	41.01	...	-0.58
UGC 06728	0.006	1.2	42.41	6.81	0.01	13.10	12.44	11.87	26.19	<39.00	<39.30	<39.00	9.41	-2.83
PG 1149-110	0.049	1.0	43.94	...	...	13.71	13.06	12.23	203.17	...	40.79	41.13	...	-0.46
NGC 4051	0.002	1.5	41.67	7.27	0.01	11.64	10.81	10.01	9.35	<39.30	39.84	39.95	9.46	-1.62
Ark 347	0.022	2.0	43.53	8.12	30.0	13.05	12.12	11.40	91.26	...	<40.39	40.79	...	-0.79
UGC 07064	0.024	1.9	43.28	...	...	13.06	12.41	11.73	101.83	...	41.45	41.59	...	-0.00
NGC 4102	0.002	2.0	41.69	7.90	...	10.85	9.77	9.16	11.31	40.32	41.07	41.08	10.24	-0.51
NGC 4151	0.003	1.5	43.12	7.69	5.32	10.26	9.43	8.51	13.30	39.00	<39.60	39.84	9.86	-1.77
Mrk 766	0.012	1.5	42.91	7.85	0.01	12.74	11.74	10.75	52.19	...	41.13	41.12	10.61	-0.47

Table 5.5(Continued.)

Name[a]	z	Type[b]	log(L_X)[c]	log(M_{BH})[d]	N_H [e]	J[f]	H[f]	K[f]	D_L	log($L_{3.3}$)	log($L_{6.2}$)	log($L_{11.3}$)	log(L_{IR})[g]	log(SFR)
			[erg s^{-1}]	[$M_\odot$]	[$\times 10^{22} cm^{-2}$]	[mag]	[mag]	[mag]	[Mpc]	[erg s^{-1}]	[erg s^{-1}]	[erg s^{-1}]	[erg s^{-1}]	[$M_\odot$ yr^{-1}]
Mrk 50	0.023	1.2	43.45	...	...	14.10	13.60	12.93	95.35	...	<40.20	40.55	...	-1.04
NGC 4388	0.008	2.0	43.64	8.53	36.17	12.48	11.73	11.06	33.87	40.04	40.61	41.00	10.69	-0.59
Mrk 771	0.063	1.0	44.11	...	...	13.85	13.06	12.14	263.89	...	<40.62	41.47	...	-0.12
NGC 4507	0.011	1.0	43.77	...	34.28	12.11	11.30	10.38	47.60	...	40.78	40.93	10.58	-0.65
ESO 506-G027	0.025	2.0	44.13	8.59	76.82	13.09	12.15	11.33	102.71	40.54	<40.56	41.01	...	-0.58
NGC 4593	0.009	1.0	43.20	8.61	0.031	11.73	11.07	10.03	36.23	<40.17	40.44	40.62	10.21	-0.98
SBS 1301+540	0.029	1.0	43.83	7.54	0.01	14.46	13.63	13.03	122.26	<40.86	<40.32	<40.27	...	-1.33
NGC 4941	0.003	2.0	41.79	...	...	12.30	11.60	11.26	14.82	...	<39.00	39.30	9.22	-2.33
NGC 4939	0.010	2.0	42.78	...	...	12.91	12.21	11.68	41.79	...	<39.47	<39.69	...	-1.89
NGC 4945	0.001	2.0	42.35	8.52	0.793	12.38	11.28	9.37	7.52	40.25	41.00	40.25	10.75	-1.33
ESO 323-077	0.015	1.2	43.22	...	...	11.51	10.49	9.44	60.70	...	41.68	41.74	10.89	0.14
NGC 4992	0.025	2.0	43.89	...	69.05	13.24	12.53	12.17	102.41	...	<40.25	<40.38	...	-1.21
II SZ 010	0.034	1.0	43.61	...	...	14.02	13.35	12.54	140.56	...	<40.32	40.90	...	-0.68
MCG-03-34-064	0.016	1.8	43.27	8.28	...	12.34	11.56	10.87	66.96	40.38	40.64	41.31	...	-0.28
Cen A	0.001	2.0	43.01	...	...	11.33	10.34	8.84	7.30	...	39.47	40.20	...	-1.38
NGC 5252	0.022	1.9	44.14	8.64	4.34	13.06	12.37	11.80	93.46	40.23	<40.25	40.14	...	-1.46
IC 4329A	0.016	1.2	44.23	8.52	0.61	11.30	10.34	9.30	64.97	40.92	<40.34	<40.53	10.88	-1.06
UM 614	0.032	1.0	43.60	...	...	13.67	12.84	11.88	133.98	...	<40.49	<40.47	...	-1.12
Mrk 279	0.030	1.5	43.92	8.62	0.013	12.19	11.22	10.39	124.56	<40.98	40.93	41.43	10.92	-0.16
Mrk 463	0.050	1.0	43.82	...	...	13.70	12.10	10.48	209.00	...	41.58	42.21	11.75	0.61
NGC 5506	0.006	1.9	43.31	7.77	2.78	12.07	10.43	9.03	24.82	40.04	40.81	40.83	10.37	-0.76
NGC 5548	0.017	1.5	43.72	8.42	0.07	11.77	10.87	10.13	69.56	40.38	40.83	41.21	10.54	-0.38
ESO 511-G030	0.022	1.0	43.66	8.66	0.098	12.89	12.00	11.21	91.03	...	<40.41	40.59	...	-1.01

Table 5.5(Continued.)

Name[a]	z	Type[b]	log(L_X)[c]	log(M_{BH})[d]	N_H [e]	J[f]	H[f]	K[f]	D_L	log($L_{3.3}$)	log($L_{6.2}$)	log($L_{11.3}$)	log(L_{IR})[g]	log(SFR)
			[erg s^{-1}]	[$M_\odot$]	[$\times 10^{22} cm^{-2}$]	[mag]	[mag]	[mag]	[Mpc]	[erg s^{-1}]	[erg s^{-1}]	[erg s^{-1}]	[erg s^{-1}]	[$M_\odot$ yr^{-1}]
Mrk 1383	0.086	1.0	44.52	...	...	13.03	12.15	11.11	368.55	...	<41.58	41.65	...	0.05
NGC 5643	0.003	2.0	41.80	...	...	12.06	11.25	10.80	16.03	...	40.36	40.53	10.23	-1.07
NGC 5674	0.024	1.9	43.35	...	...	13.03	12.23	11.57	101.56	...	41.22	41.44	10.85	-0.15
NGC 5728	0.009	2.0	43.23	8.53	82.0	12.42	11.66	11.10	37.66	40.25	40.86	41.23	10.55	-0.36
IC 4518A	0.016	2.0	43.22	...	...	13.56	12.54	11.73	65.81	...	41.37	41.43	...	-0.16
Mrk 841	0.036	1.0	44.04	8.15	0.01	13.03	12.25	11.40	149.64	...	<40.63	40.74	11.08	-0.85
Mrk 1393	0.054	1.5	44.14	...	...	13.95	13.22	12.44	226.21	...	<40.77	40.99	...	-0.60
NGC 5899	0.008	2.0	42.51	...	...	12.47	11.45	10.95	34.38	...	<40.07	40.30	10.21	-1.29
Mrk 290	0.029	1.0	43.67	7.68	0.15	13.60	12.90	12.18	120.91	<40.67	<40.38	40.79	...	-0.80
ESO 138-G001	0.009	2.0	42.56	...	...	12.79	11.80	10.61	36.79	...	40.63	40.92	10.27	-0.67
NGC 6221	0.004	1.0	42.05	...	...	11.80	10.99	10.34	20.05	...	41.19	41.24	10.70	-0.35
NGC 6240	0.024	2.0	43.99	...	...	13.33	12.54	12.12	99.69	...	42.57	42.49	...	0.89
NGC 6300	0.003	2.0	42.48	...	21.5	11.42	10.57	10.10	14.82	...	39.90	40.04	10.07	-1.54
Arp 102B	0.024	1.0	43.38	...	...	12.86	11.93	11.50	98.39	...	<40.79	40.46	...	-1.13
Mrk 507	0.055	1.0	43.56	...	...	13.78	12.83	12.28	232.93	...	42.10	42.14	11.31	0.54
3C 382	0.057	1.0	44.84	...	0.01	12.44	11.55	10.67	241.48	...	<41.10	<40.74	...	-0.85
ESO 103-035	0.013	2.0	43.65	7.73	21.6	13.01	12.11	11.51	53.65	...	<39.90	<40.34	10.63	-1.25
3C 390.3	0.056	1.0	44.88	8.52	0.12	13.59	12.59	11.71	233.80	<41.34	<40.51	<40.25	11.32	-1.33
Fairall 51	0.014	1.0	43.26	...	...	12.33	11.27	10.28	57.29	...	41.16	41.31	...	-0.28
ESO 141-G055	0.037	1.2	44.21	...	...	12.66	11.77	10.71	152.54	...	<41.08	41.49	11.17	-0.10
MCG+04-48-002	0.013	2.0	43.53	7.68	...	12.93	11.49	11.09	56.16	41.27	41.94	41.83	...	0.23
Mrk 509	0.034	1.2	44.42	8.59	0.015	12.93	11.49	11.09	141.11	41.32	41.92	41.95	...	0.35
IC 5063	0.011	2.0	43.32	7.68	21.78	12.45	11.64	10.96	45.76	40.30	<40.50	40.76	10.80	-0.83

Table 5.5(Continued.)

Name[a]	z	Type[b]	log(L_X)[c]	log(M_{BH})[d]	N_H [e]	J[f]	H[f]	K[f]	D_L	log($L_{3.3}$)	log($L_{6.2}$)	log($L_{11.3}$)	log(L_{IR})[g]	log(SFR)
			[erg s^{-1}]	[$M_\odot$]	[$\times 10^{22} cm^{-2}$]	[mag]	[mag]	[mag]	[Mpc]	[erg s^{-1}]	[erg s^{-1}]	[erg s^{-1}]	[erg s^{-1}]	[$M_\odot$ yr^{-1}]
NGC 7130	0.016	2.0	42.98	...	...	12.73	12.05	11.34	65.36	...	41.79	41.87	11.32	0.27
NGC 7172	0.008	2.0	43.46	8.31	8.19	12.50	11.51	10.45	34.94	40.59	40.99	40.91	10.41	-0.68
NGC 7213	0.005	1.5	42.50	8.63	0.025	10.90	9.826	9.48	23.45	<39.60	39.69	40.27	9.92	-1.32
II Zw 171	0.070	1.0	44.31	...	...	13.99	13.29	12.55	294.61	...	41.47	41.47	...	-0.12
Mrk 304	0.065	1.0	44.00	...	...	13.27	12.35	11.34	275.95	...	<40.69	<41.45	...	-0.14
3C 445	0.055	1.0	44.50	...	...	13.34	12.26	11.02	232.84	...	<41.14	<40.97	...	-0.62
NGC 7314	0.004	1.9	42.42	7.84	1.16	13.84	12.91	11.84	19.10	...	39.30	39.60	9.79	-2.00
Mrk 915	0.024	1.0	43.61	...	...	13.36	12.50	11.64	98.15	...	<40.60	40.84	...	-0.75
MCG+01-57-016	0.024	1.8	43.37	...	...	12.97	12.23	11.54	101.74	...	41.37	41.58	10.81	-0.01
3C 452	0.081	2.0	44.72	...	22.98	14.67	13.88	13.45	343.96	...	<40.82	<40.79	...	-0.80
NGC 7469	0.016	1.2	43.60	8.31	0.01	11.39	10.68	9.76	66.04	41.61	42.32	42.29	11.56	0.69
Mrk 926	0.046	1.5	44.77	8.95	0.035	13.14	12.30	11.50	194.00	...	<40.38	41.42	...	-0.18
PG 2304+042	0.042	1.0	43.79	...	...	14.03	13.28	12.54	173.26	...	<40.14	<40.25	...	-1.33
NGC 7603	0.029	1.5	44.00	...	...	12.00	11.18	10.15	120.69	...	41.88	41.98	10.97	0.38
NGC 7679	0.017	2.0	43.00	...	...	12.58	12.06	11.33	69.41	...	42.06	42.11	11.04	0.51
PKS 2356-61	0.096	2.0	44.52	...	...	14.98	14.25	13.75	412.71	...	<40.76	41.06	...	0.93

[a] Counterpart names taken from Baumgartner et al. (2013).

[b] Type as listed in the Swift/BAT 70-month catalog webpage[1]

[c] Hard X-ray luminosity in the 14-195 keV band.

[d] log(M_{BH}) taken from Winter et al. (2009).

[e] N_H taken from Winter et al. (2009) and Ichikawa et al. (2012a).

[f] J, H and K magnitudes taken from the 2MASS All-Sky Point Source Catalog (PSC).

[g] Derived according to Sanders & Mirabel (1996) with data from the IRAS Point Source Catalog v2.0 (PSC).

CHAPTER 6

DISCUSSION AND FUTURE WORK

6.1 On the early and extended samples.

Using our early near-IR sample, we investigate the 2.5–5 μm spectra of 54 bright nearby non-blazar AGNs from the 9-month Swift/BAT catalog having Akari/IRC observations. We investigate the relation between AGN type/absorption and star formation activities. From our present work, we conclude the following:

☑ We have detected 3.3 μm PAH emission from 24 out of 54 flux limited sample of hard X-ray selected AGNs.

☑ Strong correlations have been found between $\log(\mathrm{L}_{14-195\mathrm{keV}})$ and $\log(\mathrm{L}_{3.3\ \mu\mathrm{m}})$ as well as between $\log(\mathrm{L}_{14-195\mathrm{keV}}/\mathrm{M}_{\mathrm{BH}})$ and $\log(\mathrm{L}_{3.3\ \mu\mathrm{m}}/\mathrm{M}_{\mathrm{BH}})$ for both optical and X-ray classified type 1 AGNs.

☑ We have found no statistical difference in the mean circum-nuclear SFR, traced by the PAH 3.3 μm emission, between type 1 and type 2 AGNs for our overall sample.

☑ If we limit ourselves to low luminosity AGNs, we have stronger nuclear starburst activity in type 2 AGNs than type 1 AGNs. There is no significant difference in the star-formation activity between high luminosity type 1 and type 2 AGNs. A similar trend has been found for the sSFR, between low and high Eddington ratio samples, although the statistical significance is lower.

☑ Significant correlation have been found between $\log(\mathrm{N}_{\mathrm{H}})$ and $\log(\mathrm{L}_{3.3\ \mu\mathrm{m}})$ for the low-$\mathrm{L}_{14-195\mathrm{keV}}$ sample, while no significant correlations have been found for the high-$\mathrm{L}_{14-195\mathrm{keV}}$ sample. The significance

of correlations between $\log(N_H)$ and $\log(L_{3.3\ \mu m}/M_{BH})$ in any sample are much weaker, if any.

☑ Our results suggest that the difference between type 1/type 2 in low luminosity AGNs may reflect an evolution sequence, where more obscuring material is available around low luminosity type 2 AGNs when the circum-nuclear star-formation is feeding the central engine. At high luminosities, the difference between the two types may be mainly from the orientation effect.

During the second stage of the present research, using our extended sample, we investigate the Spitzer/IRS 5–14 μm mid-IR spectra of 130 AGNs (including 65 Seyfert 1 and 65 Seyfert 2 sources). In this mid-IR band we use the 11.3 μm PAH feature as a proxy for SF activity as indicated in Diamond-Stanic & Reike (2012).

☑ We have detected 11.3 μm PAH emission from 108 out of 130 flux limited sample of hard X-ray selected AGNs (i.e. 83% detections). From those 22 upper-limits here included, 12 are in Seyfert 1s and 10 in Seyfert 1 sources.

☑ The extended sample has a $\langle \log(L_{14-195\ keV}) \rangle = 43.457$. Values above this threshold are considered has high-$L_{14-195keV}$ sources, and those with $\log(L_{14-195\ keV}) < \langle \log(L_{14-195\ keV}) \rangle$ are considered as low-$L_{14-195keV}$ sources along this work.

☑ Strong correlation is found between 6.2 μm and 11.3 μm PAH feature. This, suggesting non-dilution of the 6.2 μm PAH feature strength with respect to the presence of the 11.3 μm PAH feature in the sample here studied.

☑ The IR luminosity of an individual source, scales with $L_{14-195keV}$. Additionally, the 11.3 μm PAH feature presents some dependence with $L_{14-195keV}$.

☑ When studing the $\log(L_{14-195keV})$–SFR properties of the sample we have found no statistical difference in the mean circum-nuclear SFR, traced by the 11.3 μm PAH emission for our overall extended sample.

☑ If separated by optical type, very similar correlation values (within the error bar) are found for Seyfert 1 and Seyfert sources for the extended sample, but with better correlation probabilities (17 and

16%, respectively).

☑ If divided by $L_{14-195keV}$, the low luminosity Seyfert 2s sub-sample presents stronger SFR compared to the low luminosity Seyfert 1s sub-sample. This, with a log rank probability of 0.82, indicating that this sub-samples are well diferentiated populations.

☑ If divided by $L_{14-195keV}$, the high luminosity Seyfert 1s sub-sample presents stronger SFR compared to the high luminosity Seyfert 2s sub-sample. This, with a log rank probability of 0.40, indicating a weaker differentition in the SFR parameter for high-$L_{14-195keV}$ Seyfert 1 and Seyfert 2 sources, but still observable.

Our analysis depends on the validity of the survival analysis in the presence of upper-limits of the 3.3 and 11.3 μm luminosities.

6.2 Future Work

We compiled an extended sample of 130 Spitzer/IRS observed AGNs (see Table 3.2) and Section 2.2 for selection details), 69 of which have also available spectral information with the Akari/IRC instrument in the 5.2–14.3 μm IR band. The near- and mid-IR spectra from the combination of Akari/IRC and Spitzer/IRS instruments of selected objects in our sample are shown in Figure 3.10. Some basic SFR properties have been studied using the 11.3 μm PAH feature. However, given the richness of the sample and the amount of elements present in the spectral range studied here, it is still necessary to explore other variables and properties as:

☑ We will test for possible inter-correlations between the 3.3 μm, 6.2 μm, 7.7 μm, 8.6 μm, 11.3 μm (Alonso-Herrero et al., 2014), 12.7 μm PAH emission features, the continuum slope and CO optical depth, as well as CO_2, H_2O and amorphous silicates (Imanishi et al., 2010). Using the 3.3 μm, 6.2 μm and 11.3 μm PAH emission features as a proxy for the SFR we will estimate the AGN type and Eddington-ratio dependences of circumnuclear SF.

☑ A continuum determination including mid- and near-infrared spectra, as well as the study of the star-forming PAH-related features and 2MASS J, H, K-bands emission properties (Ichikawa et al., 2014) will

permit to clearly disentagle of the SB/AGN/stellar components residing within the integrated spectra of the AGNs in our sample.

☑ Total infrared luminosities (L_{IR}; 8-1000 μm) have been calculated for the whole sample based on the Sanders & Mirabel (1996) relation. SFR vs. L_{IR} bahaviour will be tested for the extended sample(Kennicutt, 1998; Ichikawa et al., 2012a).

☑ A direct comparison between the 3.3 and 11.3 μm derived SFRs will be possible once we complete the line fitting for the 13 newly observed Akari/IRC AGNs (those good quality IRZ4 Akari/IRC observed objects not publicly available during our study of the early sample; see Castro et al. (2014)).

☑ The Eddington ratio (λ_{Edd}) to the X-ray luminosity shows a significant correlation in Mushotzky et al. (2008). We will test this correlation for our samples. Since we are using the same parent population (the Swift/BAT survey) we expect to obtain a very similar result. Specific SFRs estimated using this method wil be compared against our previous etimation for the early sample in Castro et al. (2014).

☑ The near- and mid-IR continuum (presumably due to dust reprocessing) slope will be measured and compared with the AGN hard X-ray power.

☑ By studing the AGN/SB contribution to the IR continuum we will identify the sources with low and high SB contribution in our X-ray selected sample. According to Brandl et al. (2006) the spectral slopes can be used to discriminate between SB and AGN powered sources and also that the PAH equivalent width is independent of the L_{IR} as both continuum and PAH feaure scale proportionally. This behaviour should be observed using the extended sample.

☑ PAHFIT (Smith et al., 2007) is a widely used IDL tool for decomposing Spitzer/IRS spectra in the literature. PAHFIT is used with full 5–35 μm low-resolution IRS spectra. This mid-IR considers starlight, thermal dust continuum, PAHs, prominent emission lines and other features. We have tested several fittings and scripts running in the 5–14 μm band using this tool. But a comprehensive study of our sample using this tool is expected in order to obtain EW measurements for all the PAHs, dust absorption features and prominent AGN-power related forbidden lines.

☑ Some of the galaxies in this work have known X-ray derived column densities, a quantity which may be related to the SF properties of the AGNs. In order to perform a proper analysis of this parameter in our extended sample we need to explore recent literature looking for X-ray derived $\mathrm{N_H}$ column densities.

Bibliography

Ajello, M., Alexander, D. M., Greiner, J., et al. 2012, ApJ, 749, 21

Alexander, D.M., & Hickox, R.C. 2012, NewAR, 56, 93

Allamandola, L.J., Greenberg, J.M., & Norman, C.A. 1979, A&A, 77, 66

Allevato, V., Finoguenov, A., Cappelluti, N., Miyaji, T., Hasinger, G., Salvato, M., Brusa, M., Gilli, R., Zamorani, G., Shankar, F., James, J. B., McCracken, H. J., Bongiorno, A., Merloni, A., Peacock, J. A., Silverman, J., & Comastri, A. 2011, ApJ, 736, 99

Altamirano-Dévora, L., Miyaji, T., Aceves, H., Castro, A., et al. 2016, RMxAA, 52, 11

Alonso-Herrero, A., et al. 2006, ApJ, 640, 167

Alonso-Herrero, A., Quillen, A.C., Simpson, C., Efstathiou, A., & Ward, M.J. 2001, AJ, 121, 1369

Alonso-Herrero, A., Ramos Almeida, C., Esquej, P., Roche, P.F., Hernán-Caballero, A., Honig, S.F. González-Martín, O., Aretxaga, I., et al. 2014, MNRAS, 443, 2766

Alonso-Herrero, A., Ramos Almeida, C., Mason, R., et al. 2011, ApJ, 736, 82

Antonucci, R.R.J. 1993, ARA&A, 31,473

Antonucci, R.R.J., & Miller, J.S. 1985, ApJ, 297, 621

Awaki, K., Ueno, S., Taniguchi, Y., Weaker, K.A. 2000, ApJ, 542, 175

Ballantyne, D.R., Everett, J.E., & Murray, N. 2006, ApJ, 639, 740

Barthelmy, S.D., Cline, T.L., Butterworth, P., Kippen, R.M., Briggs, M.S., Connaughton, V., & Pendleton, G.N. 2000, AIP Conference Series, Vol. 526., 731

Barton E.J., Geller M.J., & Kenyon S.J. 2000, ApJ,530, 660

Bassani, L., Dadina, M., & Maiolino, R. 1999, ApJS, 121, 473

Baumgartner, W.H., Tueller, J., Markwardt, C.B., Skinner, G.K., Barthelmy, S., Mushotzky, R.F., Evans, P.A., & Gehrels, N. 2013, ApJs, 207, 19

Beckmann, V., & Shrader, C.R. 2013, arXiv:1302.1397v1

Bianchi, S., Maiolino, R., & Risaliti, G. 2012, AdAst, arXiv:1201.2119

Bianchi, S., Chiaberge, M., Piconcelli, E., Guainazzi,M.,& Matt. G. 2008, MNRAS, 386, 105

Brandl, B.R., Bernard-Salas, J., Spoon, H.W.W., Devost, D., Sloan, G.C., et al. 2006, ApJ, 653, 1129

Brinchmann, J.,& Ellis, R. S. 2000, ApJ, 536, L77

Bundy, K., Georgakakis, A., Nandra, K., Ellis, R., Conselice, C., Laird, E., Coil, A., et al. 2008, ApJ, 681, 931

Burlon, D., Ajello, M., Greiner, J., et al. 2011, ApJ, 728, 58

Candian, A., Kerr, T.H., Song, I.-O., McCOmbie, J., & Sarre, P.J., 2012, MNRAS, 426, 389

Cappelluti, N., Ajello, M., Burlon, D., Krumpe, M., Miyaji, T., Bonoli, S., & Greiner, J. 2010, ApJ, 716, 2843

Cardelli, J. A., Clayton, G. C., & Mathis, J. S. 1989, ApJ, 345, 245

Castro, A., Miyaji, T., Shirahata, M., Ichikawa, K., Oyabu, S., Clark, D.M., Imanishi, M., Nakagawa, T., & Ueda, Y. 2014, PASJ, 66, 110

Chiar, J.E., & Tielens, A.G.G.M., 2006, ApJ 637, 774

Chiar, J.E., Tielens, A.G.G.M., et al. 2000, ApJ, 537, 749

Cid Fernandes, R., Gu, Q., Melnick, J., Terlevich, E., Terlevich, R., Kunth, D., Rodrigues Lacerda, R., & Joguet. B. 2004, MNRAS, 355, 273

Cid Fernandes, R., Heckman, T., Schmitt H., González Delgado, R.M., & Storchi-Bergman, T. 2001, ApJ, 558, 81

Clavel, J., et al. 2000, A&A, 357, 839

Cisternas, M., Jahnke, K., Inskip, K. J., et al. 2011, ApJ, 726, 57

Cusumano, G., La Parola, V., Segreto, A., et al. 2010A, A&A, 510, A48

Cusumano, G., La Parola, V., Segreto, A., et al. 2010B, A&A, 524, A64

Dartois,E. 2007, Interstellar dust grains: the hydrogenated amorphous carbon constribution. In: Molecules in Space and Laboratory

Davies, R.I., Müller Sánchez, F., Genzel, R., Tacconi, L.J., Hicks, E.K.S., Friedrich, S., & Stemberg, A. 2007, ApJ, 671, 1388

Davies, R.I., Thomas, J., Genzel, R., Müller-SÃąnchez, F., Tacconi, L.J., Sternberg, A., Eisenhauer, F., Abuter, R., Saglia, R., & Bender, R. 2006, ApJ, 646, 754

De Grijp, M.H.K, Miley, G.K., Lub, J., & De Jong, T. 1985, Nature, 314, 210

Diamond-Stanic, A.M., & Reike, G.H. 2010, ApJ, 724, 140

Diamond-Stanic, A.M., & Reike, G.H 2012, ApJ, 746, 168

Donley, J.L., Koekemoer, A.M., Brusa, M., Capak, P., Cardamone, C.N., Civano, F., Ilbert, O., et al. 2012, ApJ, 748, 142

Dwek, E., Sellgren, K., Soifer, B.T., & Werner, M.W., 1980, ApJ, 238, 140

Eckart, M.E., McGreer, I.D., Stern, D., Harrison, F.A., & Helfand, D.J. 2010, ApJ, 708, 584

Ellison, S.L., Patton, D.R., Mendel, J.T., & Scudder, J.M. 2011, MNRAS, 418, 2043

Elitzur, M. 2012, ApJ, 747, 33

Elitzur, M., & Shlosman, I. 2006, ApJ, L101

Egusa, F., Lorente, R., Onaka, T., Ita, Yoshifusa, Ohyama, Y., Tanabe, T., Pearson, C., & Yamashita, T. (2016) "AKARI IRC Data User Manual Version 2.2" (Sagamihara:JAXA/ISAS)

Esposito, V., & Walter, R. 2016, A&A, 590, 49

Esquej, P., Alonso-Herrero, A., González-Martín, O., Hönig, S.F., Hernán-Caballero, et al. 2014, ApJ, 780, 86

Fazio, G.G., et al. 2004, ApJs, 154, 10

Fetzer, J. 2016, The Polycyclic Aromatic Compounds: Health effects ans Safety Issues, AstroPAH, vol. 26

Feigelson, E. D., & Nelson, P. I. 1985, ApJ, 293, 192

Freudling, W., Siebenmorgen, R., & Haas, M. 2003, ApJ, 599, L13

Fritz, J., Franceschini, A., & Hatziminaoglou, E. 2006, MNRAS, 366, 767

Gehrels, N., et al. 2004, ApJ, 611, 1005

Genzel, R., Lutz, D., Sturm E., Egami E., & Kunze D. 1998, ApJ, 498. 579

Giard, M., Serra, G., Caux, E., Pajot, F., & Lamarre, J.F. 1988, A&A, 201, L1

Gilli, R., Comastri, A., & Hasinger, G. 2007, A&A, 463, 79

González-Martín, O., et al. 2013, A&A, 553, A35

Güver, T., & Özel, F. 2009, arXiv:0903.2057v2

Hammonds, M., Mori, T., Usui, F., & Onaka, T. 2015, Planetary and Space Science, 73, 83

Hasinger, G. 2008, A&A, 490, 905

Hasinger, G., Burg, R., Giacconi, R., Schmidt, M., Trumper, J., & Zamorani, G. 1998, A&A, 329, 482

Haas, M., Siebenmorgen, R., Schulz, B., Krügel, E., & Chini, R. 2005, A&A, 442, 39

Hickox, R. C., Myers, A. D., Brodwin, M., Alexander, D. M., Forman, W. R., Jones, C., Murray, S. S., Brown, M. J. I., Cool, R. J., Kochanek, C. S., Dey, A, Jannuzi, B. T., Eisenstein, D., Assef, R. J., Eisenhardt, P. R., Gorjian, V., Stern, D., Le Floc'h, E., Caldwell, N., Goulding, A. D., & Mullaney, J. R. 2010, ApJ, 716, 2843

Hönig, S.F., Kishimoto, M. 2010, A&A, 523, A27

Houck, J.R., et al. 2004, ApJs, 154, 18

Ichikawa, K., Ueda, Y., Terashima, Y., Oyabu, S., Gandhi, P., Matsuta, K., & Nakagawa,T. 2012, ApJ, 754, 45

Ichikawa, K., Ueda, Y., Terashima, Y., Oyabu, S., Gandhi, P., Matsuta, K., & Nakagawa, T. 2012, "Torus Workshop Proceedings", p. 109 (Texas:University of Texas at San Antonio)

Ichikawa, K., Imanishi, M., Ueda, Y., Nakagawa, T., Shirahata, M., Kaneda, H., & Oyabu, S. 2014, ApJ, 794, 139

Imanishi, M. 2003, ApJ, 599, 918

Imanishi, M. & Dudley, C. C. 2000, ApJ, 545, 701

Imanishi, M., Nakagawa, T., Shirahata, M., Ohyama, Y., & Onaka,T. 2010, ApJ, 721, 1233

Imanishi, M. & Maloney, P. 2003, ApJ, 588, 1651

Imanishi, M. & Wada, K. 2004, ApJ, 617, 214

Isobe, T., Feigelson, E. D., & Nelson, P. I. 1986, ApJ, 306, 490

James, F., & Roos, M. 1975, ApJ, 10, 343

Joblin, C., & Tielens, A.G.G.M. (Eds) 2011, PAHs and the Universe: A Symposium to Celebrate the 25th Anniversary of the PAH Hypothesis. EAS Publications Series, vol. 46

Kawakatu, N., & Wada, K. 2008, ApJ, 681, 73

Khachikian, E.Y., & Weedman, D.W. 1974 , ApJ, 192, 581

Kennicutt, R. C., Jr. 1998, ARA&A, 36, 189

Kennicutt, R. C., Jr., et al. 2003, PASP, 115, 928

Kishimoto, M., Hönig, S. F., Antonucci, R., et al. 2011, A&A, 536, A78

Krivonos, R., Revnivtsev, M., Tsygankov, S. et al. 2010, A&A, 519, 107
2012, ApJ, 744, 148

Kocevski, D.D., Faber, S.M., Mozena, M., et al. 2011, A&A, 536, A78

La Franca, F., Fiore, F., Comastri, A., et al. 2005, ApJ, 635, 864

Lagos, Claudia del P., Cora, S., & Padilla, N. 2008, ApJ, 758, 1

LaMassa, S. M., Heckman, T. M., Ptak, A., Schiminovich, D., O'Dowd, M., & Bertincourt, B. 2012, ApJ, 758, 1

Lavalley, M. P., Isobe, T., & Feigelson, E. D., 1992, in Astronomical Data Analysis Software and Systems I, eds. D. M. Worrall, C. Biemesderfer, & J. Barnes (San Francisco: ASP), 245

Lawrence, A., & Elvis, M. 1982, ApJ, 256, 410

Lawrence, A., & Elvis, M. 2010, ApJ, 714, 561

Li, A. 2006, ASP Conf. Series, Vol. 373, 561

2001, ApJ, 550, L213

Lutz, D., Spoon, H. W. W., Rigopoulou, D., Moorwood, A. F. M., & Genzel, R. 1998, ApJ, 505, L103

Lusso, E., Comastri, A., Simmons, B. D., Mignoli, M., Zamorani, G., Vignali, C., et al. 2012, MNRAS, 425, 623

Maiolino, R., & Rieke, G.H. 1995, ApJ, 454, 95

Maiolino, R., & Rissaliti, G. 2007, ASPCS, 373, 447

Maiolino, R., Rissaliti, G., Salvati, M., et al. 2010, A&A, 517, A47

Marco, O., & Alloin, D. 2000, A&A, 465, 472

Markowitz, A.G., Krumpe. M., & Nikkuta, T. 2014, MNRAS, 439, 1403

Markwardt, C. B., Tueller, J., Skinner, G. K., Gehrels, N., Barthelmy, S. D., & Mushotzky, R. F. 2005, ApJ, 633, L77

Mateos, S., Alonso-Herrero, A., Carrera, F.J., Blain, A., Watson, M.G., et al. 2012, MNRAS, 426, 3271

Mennella, V., Munoz Caro, G.M., Ruiterkamp, R., Schutte, W.A., Greenberg, J.M., Brucato, J.R., & Colangeli, L. 2001, A&A, 367, 355

Mor, R., Netzer H., & Elitzur M. 2009, ApJ, 705, 298

Mouri, H., Kawara, K., Taniguchi, Y., & Nishida, M. 1990, ApJ, 356, L39

Moorwood, A. F. M. 1986, ApJ, 166, 4

Mulas, G., Zonca, A., Casu, S., & Cecchi-Pestellini, C. 2017, ApJS, 207, 7

Murakami, H., Baba, H., Barthel, P., Clements, D. L., Cohen, M., Doi, Y., Enya, K., Figueredo, E., Fujishiro, N., Fujiwara, H., & Fujiwara, M. 2007, PASJ, 59, 369

Mushotzky, R.F., Winter, L.M.,McIntosh, D.H., & Tueller, J. 2008, ApJ, 684, 65

Nenkova, M., Sirocky, M.M., Nikkutta, R., et al. 2008, ApJ, 685, 160

Nikutta, R. ,Elitzur M., & Lacy M. 2009, ApJ, 707, 1550

Nishiyama, S., Nagata, T., Kusakabe, N., Matsunaga, N., Naoi, T., Kato, D., Nagashima, C., Sugitani, K., Tamura, M., Tanabé, T., & Sato, S. 2006, ApJ, 638,839

Nishiyama, S., Tamura, M., Hatano, H., Kato, D., Tanabé, T., Sugitani, K., & Nagata, T. 2009, ApJ, 696,1407

Noguchi, M. 1988, A&A, 203, 259

Norman, C., & Scoville, N. 1988, ApJ, 332, 124

Novak, G.S., Faber, S.M., & Dekel, A. 2006, ApJ, 637, 96

Ohyama, Y., Onaka, T., Matsuhara, H., Wada, T., Kim, W., Fujishiro, N., Uemizu, K., et al. 2007, PASJ, 59, 411

Oi, N., Imanishi, M., & Imase, K. 2010, PASJ, 62, 1509

Onaka, T., Lorente, R., Ita Y. et al. (2009) "AKARI IRC Data User Manual for Post-Helium (Phase 3) Mission" (Sagamihara:JAXA/ISAS)

Onaka, T., Matsuhara, H., Wada, T., et al. 2007, PASJ, 59, 401

Osterbrock, D.E. 1977, ApJ, 215, 733

Peeters, E., Spoon, H.W.W., & Tielens, A.G.G.M. 2004, ApJ, 613, 986

Perry, J.J., & Dyson, J.E. 1985, MNRAS, 213, 665

Pilleri, P., Joblin, C., Boulanger, F., & Onaka, T. 2015, A&A, 577, A16

Quillen, A.C., Alonso-Herrero, A., Rieke, M.J., Rieke G.H., Ruiz, M., Kulkarni, V. 1999, ApJ, 527, 696

Ramos-Almeida, C., Levenson, N.A., Alonso-Herrero, A., et al. 2011, ApJ, 731, 92

Richards, G.T., et al. 2006, AJ, 131, 2766

Román-Zúñiga, C.G., Lada, C. J., Muench, A., & Alves, J. F. 2007, ApJ, 664,35

Rodriguez-Ardila, A., & Mazzalay, X. 2004, arXiV:0601313v1

Sanders, D.B., & Mirabel, I.F. 1996, ARA&A, 34, 749

Sanders, D. B., Soifer, B.T., Elias, J.H., Madore, B.F., Matthews, K., Neugebauer,G., & Scoville, N. Z. 1988, ApJ, 325, 74

Schartmann, M., Meisenheimer, K., Camenzind, M., et al. 2008, A&A, 482, 67

Schlegel, D., Finkbeiner D.P., & Davis, M. 1998, ApJ, 638, 839

Shinozaki, K., Miyaji, T., Ishisaki, Y., Ueda, Y., & Ogasaka, Y. 2006, ApJ, 131, 2843

Silverman, J.D., Kampczyk, P., Jahnke, K., et al. 2011, ApJ, 743, 2

Simpson, C. 2005, MNRAS, 360, 565

Smith, J.D., Draine, B.T., Dale, D.A., Moustakas, J., Kennicut, R., Jr., Helou, G., Armus, L., et al. 2007, ApJ, 656, 770

Smith, R.G., Sellgren, K., & Tokunaga, A.T. 1989, ApJ, 344, 413

Soltan, A. 1982 , MNRAS, 200, 115

Song, I.-O., Kerr, T.H., McCombie, J., & Sarre, P.J. 2003, MNRAS, 346, L1

Spinoglio, L., Malkan, M., Smith, H.A., González-Alfonso, E., & Fischer, J. 2005, ApJ, 623, 123

Stern, D. 2005, ApJ, 631, 163

Sturm, E., et al. 2005, ApJ, 629, L21

Tielens, A. G. G. M. 2008, ARA&A, 46,289

Tokunaga, A.T., Sellgran, R.G., Nagata, T., Sakata, A., & Nakada, Y. 1991, ApJ, 380, 452

Tristram, K.R.W., Meisenheimer, K., Jaffe, W., Schartmann, M., et al. 2007, A&A, 474, 837

Tueller, J., Baumgartner, W. H., Markwardt, C.B., et al. 2010, ApJs, 186, 378

Tueller, J., Mushotzky, R. F., Barthelmy, S., et al. 2008, ApJ, 681, 113

Ueda, Y., Akiyama, M., Hasinger, G., Miyaji, T., & Watson, M. 2014, ApJ, 786, 104

Ueda, Y., Akiyama, M., Ohta, K., & Miyaji, T. 2003, ApJ, 598, 886

Ueda, Y., Hiroi, K., Isobe, N., Hayashida, M., Eguchi, S., Sugizaki, M., Kawai, N., Tsunemi, H., Mihara, T., Matsuoka, M., Ishikawa, M., et al. 2011, PASJ, 63, 937

Urry, P., & Padovani, P. 1995, PASP, 107, 803

Vasudevan, R. V., Mushotzky, R. F., Winter, L., & Fabian, A.C. 2009, MNRAS, 399, 1553

Voit, G. M. 1992, ApJ, 399, 495

Voss, R., Ajello, M. 2010, ApJ, 721, 1843

Watabe, Y., Kawakatu, N., & Imanishi, M. 2008, ApJ, 677, 895

Weaver, K.A., Meléndez, M., Mushotzky, R.F., Kraemer, S., Engle, K., Malamuth, E., et al. 2010, ApJ, 716, 1151

Weedman, D.W., Feldman, F.R., Balzano, R., et al. 1981, ApJ, 248, 105

Weedman, D.W,, Sargsyan, L., LeBouteiller, V., Houck,J.R., & Barry, D., 2012, ApJ 761, 184

Wilson, A.S., & Tsvetanov, Z.I. 1994, AJ, 107, 1227

Winter, L. M., Lewis, K. T. Koss, M., Veilleux, S., Keeney, B., & Mushotzky, R. F. 2010, ApJ, 710, 503

Winter, L. M., Mushotzky, R. F., Reynolds, C. S. & Tueller, J. 2009, ApJ, 690, 1322

Wu, Y., Charmandaris, V., Huang, J., Spinoglio, L., & Tommasin, S. 2009, ApJ, 701, 658

Yamada, R., Oyabu, S., Kaneda, H., et al. 2013, PASJ, 65, 103

APPENDIX A

DEVELOPED SOFTWARE

In order to improve the data analysis required for the present work, a series of programs were developed to provide a tool capable of performing repetitive processes involving spectral data reduction, variable selection criterion, combination of multiple spectra from a single object, wavelength correction, galactic de-reddening correction, spectral plotting, spectral line fittings, statistical analyses and others. These programs were required in order to avoid unnecessary repetition of simple steps.

This semi-automatic scheme requires an input of two lists, one with the Akari/IRS selected sources and a second list with the Spitzer/IRS selected sources. These lists include information about the object name, x-ray luminosity, coordinates, redshift, optical type, luminosity distance, and others. The provided parameters are read by the programs and used for the respective purposes. If a certain source is no longer required then that source just need to be erased from the list and run the program scripts in order to obtaing new spectral plots, histograms and image mosaics.

A simple FORTRAN/tcsh program (`auto-spec.f95`; see Figure A.1) was developed in order to speed up the file management and the data reduction process. This script read a data-file containing a list of sources to be processed, then the raw spectral files were uncompressed, input and output directories required by the IDL Akari/IRC Spectroscopy Toolkit (see Section 3.2.2) were also created. The Akari/IRC reduction toolkit required to be individually executed for each sprectra using the specifically self-generated commands from the script. The toolkit is not automatic, it requires some level of supervision by the user. Once the execution ended for a particular object the observed spectrum was kept in an output directory, thus making it easier to

collect results. The script continued reading the list until all objects were processed.

AGN sources can have from one to five orbits of Akari/IRC observations. Another FORTRAN/tcsh/Awk program (`akari-av70.f95`; see Figure A.1 and A.2(*left*)) was developed in order to obtain an averaged spectrum of each source in our selection list. As a result, this program generated an output directory and a log file containing the information of the averaged spectra. In the end, a visual review of the products was necessary to determine which spectra were to be excluded from the sample because of their poor quality and/or incompleteness. In order to average multiple available Spitzer/IRS spectra from sigle sources a FORTRAN/tcsh/Awk program (`spitzer-av70.f95`) was developed in order to obtain an averaged spectrum of each source in our selection list. This program process spectra in the same way than its done for the Akari/IRC spectra but with slight diferences in data format. As a result, this program generated an output directory and a log file containing the information of the averaged spectra. Taking the spitzer observation log as a primary reference we defined a final list-of-spectra.

Mosaics shown both Spitzer/IRS and Akari/IRC spectra (shown in Figure 3.10) of our X-ray selected sample are automatically composed using the program `s70-multiplot-irs.f95` as shown in Figure A.3(*left*). This program calculates the number of sources, the minumun and maximum wavelength of the available spectra as wells as the maximum flux in order to define a scale for both spectra. This program employs a composition of *gfortran*, *gawk*, *gnuplot* and *unix* commands. A red-filter mosaic of images obtained from the Digital Sky Survey (DSS) is shown in Figure 2.7. The flow-diagram ot the program. `s70-multiplot-dss.f95` responsible for generating these mosaics is shown in A.3(*right*). Fits files were previously downloaded using the ESO dss2 batch tool. This program employs a composition of *gfortran* and *gnuplot* commands. All the programs and scripts described in Figure A.1 can work as pieces of a general block diagram. Each block works independently if required. Some parts of the process, such as the download of the spectra, spectral qualkity check, specification of the selection criteria and spectral line fitting remain to be manual.

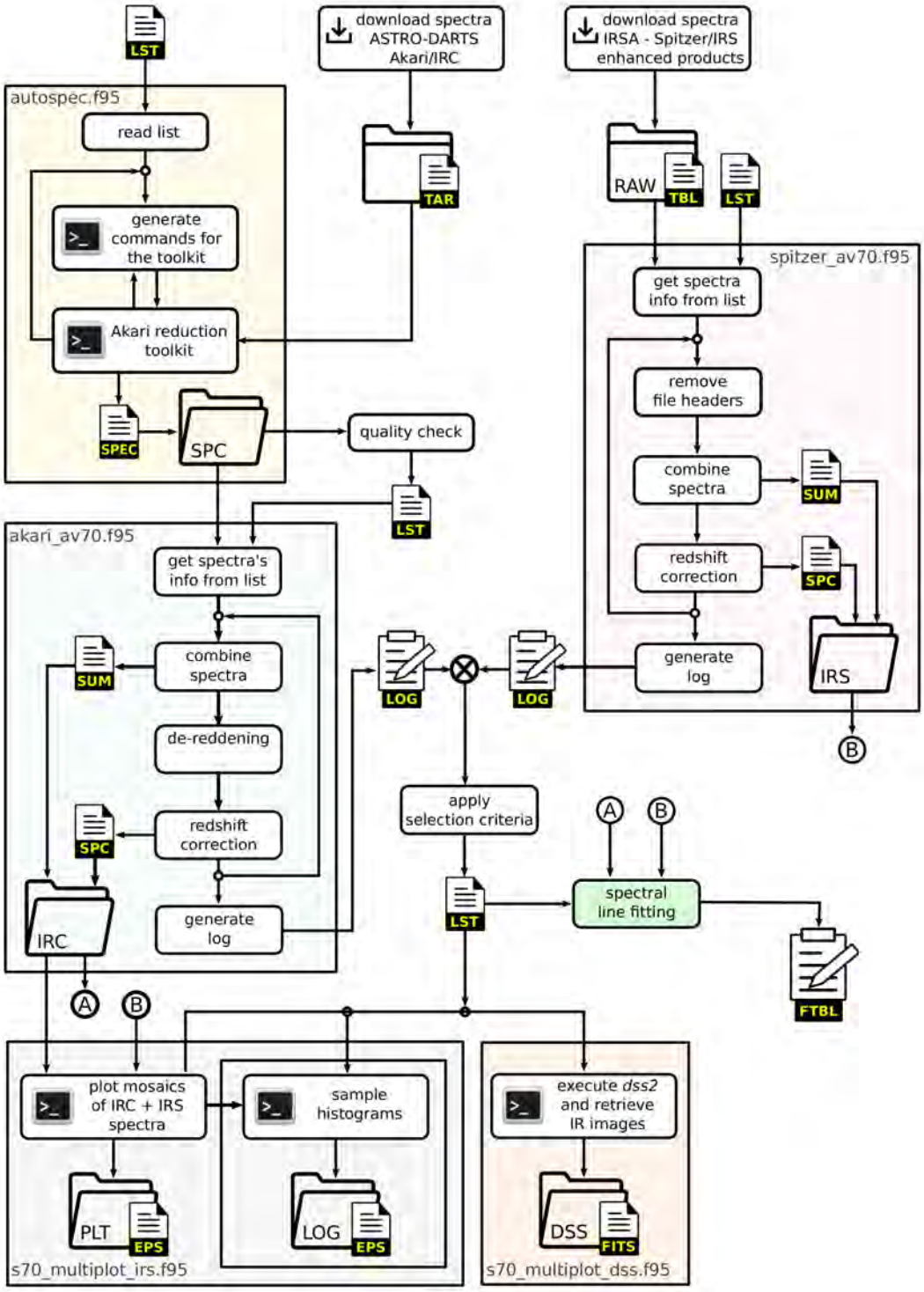

Figure A.1: Block-diagram of the data analysis process involved in the present work. In order to prevent changes on the selected criteria and/or the analysis proccess a set of programs and scripts were developed, thus, we are able to proccess and plot spectra in a semi-automatic way.

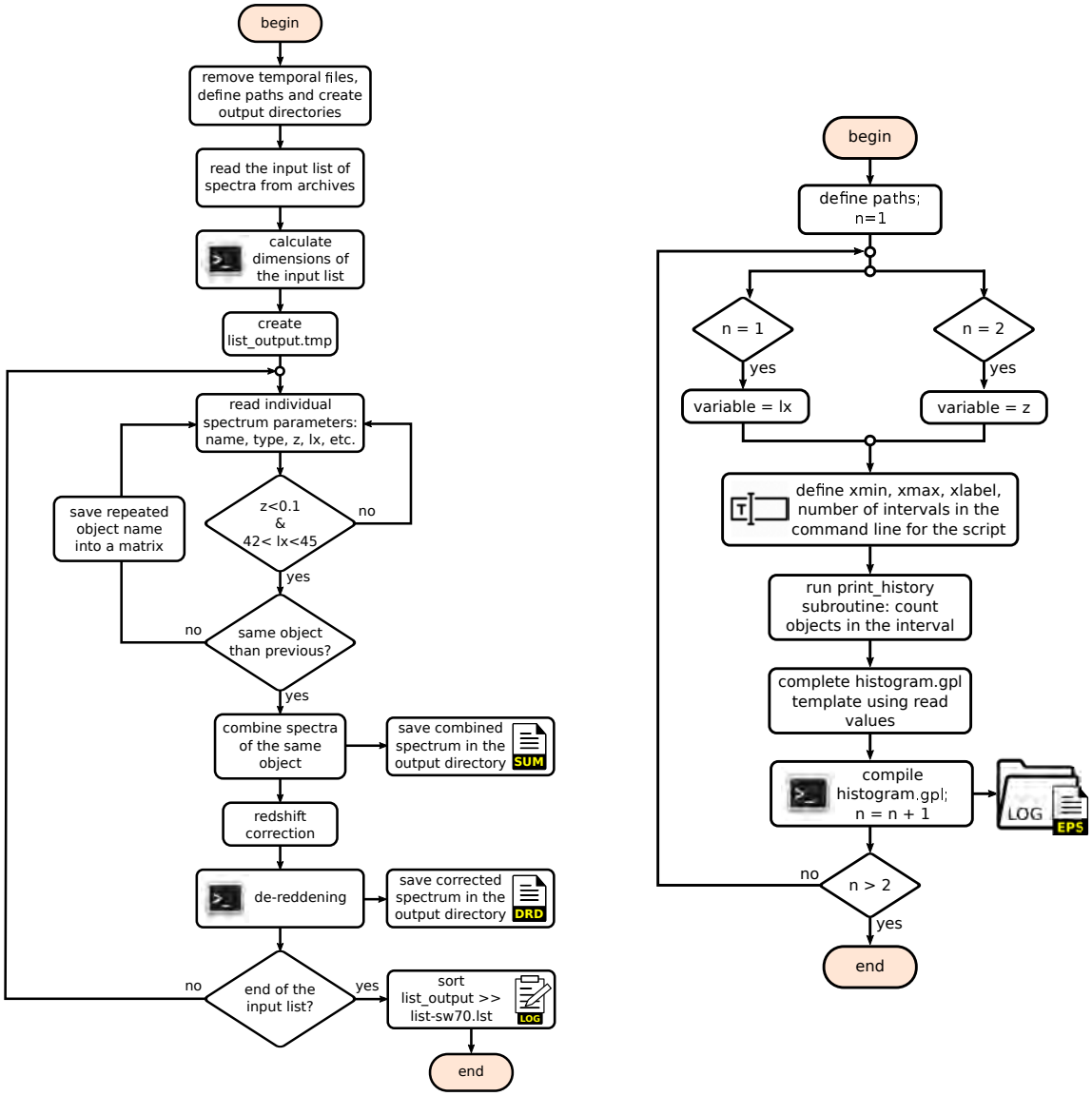

Figure A.2: (*Left*) Flow-diagram of the developed program to average all good quality spectra from the same object downloaded from the archives. Two different programs were writen for Akari/IRC and Spitzer/IRS but work in the same way. The program `av-swift70.f95` employs a composition of *gfortran*, *gawk* and *unix* commands. (*Right*) Flow-diagram of the program `histogram-s70.f95` used to create histograms for several parameters taken from the main input list (the sample selection).

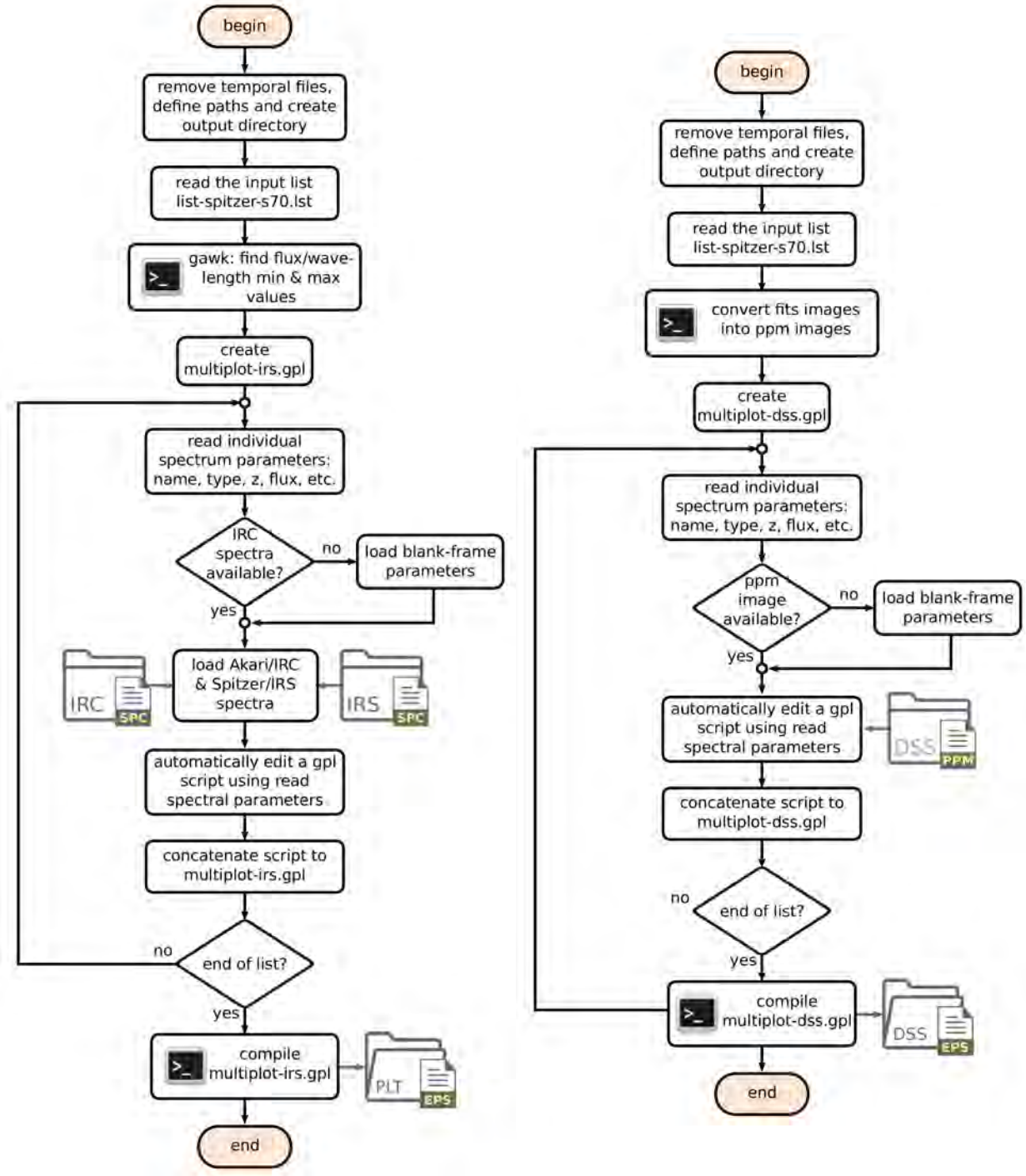

Figure A.3: (*Left*) Flow diagram of the program `irs-multiplot-s70.f95` used to plot a series of mosaics of the Akari/IRC and Swift/IRS spectra. (*Right*) Flow diagram of the program `dss-multiplot-s70.f95` used to plot a series of mosaics of the DSS infrared images of the galactic sources in our sample.